The Dissertation Committee for Swadhin Pradhan
certifies that this is the approved version of the following dissertation:

Battery-free Wireless Sensing and Beyond

Committee:

_____

Lili Qiu, Supervisor

_____

Aloysius Mok

_____

Mohamed G. Gouda

_____

Karthikeyan Sundaresan

Battery-free Wireless Sensing and Beyond

by

Swadhin Pradhan

DISSERTATION

Presented to the Faculty of the Graduate School of

The University of Texas at Austin

in Partial Fulfillment

of the Requirements

for the Degree of

DOCTOR OF PHILOSOPHY

THE UNIVERSITY OF TEXAS AT AUSTIN

August 2020

To *Ma* and *Baba*, who have always been there.

Acknowledgments

I relished every bit of my time at UT Austin as a Ph.D. student. It was as much a journey inside through introspection as it was a pursuit of knowledge through hypotheses and experiments. It made me realize that the purpose of education is not merely filling the mind with facts, but also perfecting its ability to question and find new frontiers. It made me understand being a lifelong learner by embarking on a never-ending journey across the valleys of curiosity. *Walt Disney* aptly said: *"When you're curious, you find lots of interesting things to do"*.

I owe my deepest gratitude to Prof. Lili Qiu, my advisor. I have always enjoyed discussing research with her and sharing her passion for work and commitment to perfection. I am forever indebted to her for all her sleepless nights, and the effort she expended every day for the last six years to make me what I am today. Thank you, Lili, for being a great advisor, an excellent researcher, and a kind person.

I am also grateful to my Ph.D. committee members and mentors - Dr. Karthikeyan (Karthik) Sundaresan, Prof. Aloysius Mok, and Prof. Mohamed G. Gouda. Working with Karthik on the *Rio* project was a great learning experience because of his excellence in research and humility in life. I have learned the critical skill of remaining calm during the inevitable difficulties of

closest cousin-brothers: Tappa, Roni, Akash, and Shivam were the moments to cherish and the much-needed getaways from my daily struggle of Ph.D. I also want to express my heartfelt gratitude to my dearest *Dadu* (affectionate term for maternal grand-father in Bengali), who unfortunately passed away during my Ph.D. He was always proud of the smallest of achievements of his grandson. I miss you, *Dadu*.

Finally, my deepest gratitude and love goes to my mother (*Ma* in Bengali), Swagata, and my father (*Baba* in Bengali), Subhas. Whenever I try to write this part of the note, a host of memories and emotions rush to my mind, and words fall short. I remember their faces during my first stage performance, when I learned to ride a bike, and my college graduation ceremony. Thousands of such tiny moments of their inspiration, support, sacrifices, and love have become the foundation of my life. I have always been amazed by my father's practical skills, which I believe played a critical role in my decision to become an engineer first, and a researcher later. The intoxicating smile and simplicity of my mother kept the child inside me always alive. I missed her selfless love and care the most during my Ph.D.

Moreover, they have shown their unwavering support for any of my adventures. They did not make me realize for a moment about their unrelenting grief of living without their only child. Thank you, *Ma*, and thank you, *Baba*, for all that you are and for everything that you have done for me. I dedicate the dissertation to you.

Battery-free Wireless Sensing and Beyond

Swadhin Pradhan

The University of Texas at Austin, 2020

Supervisor: Lili Qiu

The future of Internet-of-Things (IoT) demands seamless interaction between users and devices. The vision is also of one, where sensing and actuation interfaces blend into everyday objects. If all these interactions and sensing interfaces are realized without the need of an integrated power source and built upon hardware so cheap and simple that it can be installed or discarded easily; then, any physical space can become truly context-aware.

Firstly, to achieve this vision of IoT-enabled smart space, we first design and develop RIO, a novel battery-free touch-sensing user interface (UI) primitive. With RIO, any surface can be turned into a touch-aware surface by directly attaching RFID tags to them. RIO is built using the technique of impedance tracking: when a human finger touches the surface of an RFID tag, the impedance of the antenna changes. This change manifests as a variation in the phase of the RFID backscattered signal and is used by RIO to track fine-grained touch movement over both off-the-shelf and custom-built tags.

Secondly, we build a system that analyzes ball motion using a single RFID reader antenna and RFID tags. Despite significant work on wireless sensing, most existing works focus on sensing translation movement or absolute localization. However, rotational motion is also essential, especially in sports analytics (*e.g.*, tracking ball movement), yet has been under-explored. Motivated by the need, we use RFID tags to sense a ball's speed, direction, spin, and rotation axis. In particular, we exploit the polarization in RFID to enable motion sensing. We develop a model to capture the impact of polarization on the received signal and an optimization framework to incorporate the model to estimate the ball movement. We implement our system, Tag-based Inertial Measurement Unit (*TIMU*), and demonstrate its effectiveness through an extensive evaluation. To the best of our knowledge, this is the first RFID system that can sense general motion using a single RFID antenna.

Finally, we further develop a system called RTSense, which enables RFID tags to sense room temperature. Our key insight is that the impedance of the RFID tag changes with the temperature, and such a change can be reflected in the tag reading. Thus, we can piggy-back communication channels with sensing information. However, it is challenging to achieve high accuracy and robustness against environmental changes. To address these challenges, we first develop a detailed analytical model that captures the impact of temperature change on the tag impedance. We then build a system that leverages a pair of tags that respond differently to the temperature change to cancel out the environmental changes.

Table of Contents

List of Tables

List of Figures

xx

Chapter 1

Introduction

The future of interactive smart-spaces counts on *seamless ubiquitous sensing* [72] powered by the Internet of Things (IoT). Because, accurate sensing of the surrounding fuels the context-awareness, which is critical for the *intelligence* of these spaces. This vision of the future also demands seamless integration of intuitive interaction between users and smart devices. This vision can only be realized if sensing and actuation interfaces are embedded into common everyday objects, without a huge infrastructure burden. Imagine if all these input and sensing modalities operate without the need for any *built-in* battery or power source, and built upon hardware so cheap and simple that it can be installed or discarded easily. In this proposal, we build on this vision of ubiquitous wireless sensing using battery-free cheap stickers by re-purposing or customizing the Radio-Frequency IDentification (RFID) tags. More specifically, we aim to enable three aspects of ubiquitous wireless sensing: *user interaction sensing, environment sensing*, and *object movement sensing*. Furthermore, we want to make these systems seamless and easy-to-incorporate.

However, passive RFID tags have already been used to develop sensing, activity recognition and localization solutions [78, 209, 108, 107, 184, 198].

Among these notable works, machine learning techniques using the PHY-layer features of both off-the-shelf [108] and custom-built tags [107] have been successful in classifying several well-defined gestures such as hand waving, touching and swiping. Other approaches such as [159], have also designed custom backscatter capacitive measurement circuits to detect touch events on the tag antenna. Apart from these works, there are some recent works [115, 113, 94] which use higher bandwidth through universal software radio platforms to enable cm-level fine-grained tracking or food-quality detection. Furthermore, there are few recent techniques which leverage RFID-tags to sense a few information of interest of the immediate surroundings, like temperature, light, humidity, etc. [178] experiments with connecting commercial sensors onto the passive antennas of RFID tags to sense different properties of the surrounding, whereas [54] uses customized RFID tag to measure the temperature. However, all these approaches, trade-off among various practical factors, like, communication range, cost, and sensing resolution. In the following, we focus on the main challenges to realize this vision of battery-free wireless sensing with commercial off-the-shelf components.

1.1 Challenges

While intuitive and attractive, making passive RFID based wireless sensing based systems work well in practice for different types of applications involves several challenges. Main challenges are the following:

- **Enabling Seamless and Ubiquitous Interactivity**: To realize the

vision of large IoT-enabled smart spaces, we need to break the barrier between the user and the intended application. If we can enable seamless interaction between the users and the objects in the environment through battery-free RFID tags, it would be an important first step toward the goal. How can we enable touch interaction in everyday objects through RFID tags in a scalable and robust manner? In a multi-tag setting, how to avoid or better even, exploit the mutual coupling phenomenon in RFID tags to measure the single point touch detection and tracking reliably?

- **Enabling Complex Motion Sensing**: To track the motion states of a moving object in a dynamic environment, one needs to infer the translation and rotation information simultaneously. How can we achieve this with a minimal hardware setup such as a single RFID reader antenna? Furthermore, can we achieve this accuracy with minimal change in the environment or the moving object without any customized hardware setup? This seamless track-able complex motion information can be used to make the spaces more context-aware.

- **Going beyond the Mobility Sensing**: To sense beyond the mobility or interactivity also plays a critical role in realizing the vision of genuinely context-aware smart spaces. For example, can we sense the environmental temperature with these passive RFID tags in a robust manner? In the presence of the intrinsic environmental variations, how

can we design a system or metric to be reliable? How to make a perfect trade-off among the communication range, cost, latency, and robustness for these types of passive sensing systems? Can we provide some insights regarding this? These challenges are generally side-stepped in the previous tag sensing works [64, 65, 68].

1.2   Our Approach

To realize the grand vision of fully context-aware connected smart-spaces, where ubiquitous wireless sensing is a reality, we propose to build three end-to-end systems that tackle different aspects of the goal. The goals of these three novel passive RFID systems are designed to mainly address the challenges mentioned above. Firstly, we develop a battery-free touch primitive, called Rio, which can be embedded in everyday objects and addresses the issue of *ubiquitous interactivity.* Secondly, we use these passive RFID tags to track the motion information (both translation and rotation) of a moving ball using a single RFID reader antenna, which addresses the problem of *complex motion sensing.* Thirdly, we build a wireless battery-free temperature sensor, called RIO, which can easily be blended into the wall surfaces to measure the indoor temperature. This helps to address the challenge of *environmental sensing.*

These three components touch upon three leading players of this vision of context-aware smart space: user, environment, and object. In Rio, we enable seamless user interaction with the environment, which opens up the possibility of making any object interactive. This also unfolds the grand vi-

4

sion of ubiquitous interactivity. Moreover, passive RFID system based motion tracking also provides information about the moving object in the environment. In RIO, we go beyond traditional translational motion estimation and incorporate rotational motion-sensing too. Whereas, RTSENSE provides an attractive solution to sense and communicate the environmental temperature. This helps in making a space genuinely context-aware. In the following, we provide a brief description of each of the three modules of this proposal.

1.2.1 RIO: Battery-Free Touch UI

In the first work, we explore the design of a battery-free fine-grained touch gesture input interface using Radio Frequency IDentification (RFID) technology. We have focused on the following things to implement RIO.

Firstly, to validate the reliability of RIO's primitive, we present a detailed a measurement study of RFID backscatter signals in response to physical touch across the RFID antenna. We use both over-the-air and Vector Network Analyzer (VNA) measurements, to show how (a) the impedance of the RFID antenna will vary in response to the physical touch; (b) the amount of variation depends on the location of the physical contact with the antenna; and (c) the variations in antenna impedance form the dominant factor (compared to other artifacts like multi-path) contributing to a corresponding change in the magnitude and phase of the backscattered signal. Equipped with this understanding, RIO uses this touch-dependent phase change behavior of RFID tags as a primitive to detect touches on an RFID tag, as well as to track the

location of the finger during a swipe over the tag surface.

Secondly, Previous works have identified that *mutual coupling* between tags [174, 56, 133, 188] has a significant impact on the backscattered signal phase. Hence, when multiple RFID tags are deployed close together on the same surface, the backscattered phase is affected by both the physical contact with the RFID antenna, as well as mutual coupling effects, thereby substantially affecting the tracking accuracy. While previous works have made similar observations [174, 56, 133, 188], the impact of such coupling has been overcome largely by building tolerance into the solution. In contrast, we take a more active approach to model and understand the impact of inter-tag coupling on our primitive. With the help of our measurement campaign and supporting model, we show that while coupling can affect the phase change behavior on the desired tag and hence its tracking accuracy, it contributes to a stable, predictable phase-change pattern in the neighboring tags. Thus, by leveraging the collective phase-change behavior across multiple tags, RIO translates the challenge of coupling into an opportunity to enhance the tracking accuracy even in multi-tag scenarios.

Thirdly, we design algorithms that leverage the touch-based phase-change primitive in RIO as well as the inter-tag coupling behavior to track touches to a median error of only 3 and 7 *mm* in single and multi-tag settings respectively. RIO's algorithms provide the flexibility to operate at various points in the accuracy-latency trade-off curve, allowing for a reasonable loss in accuracy for a more responsive real-time tracking.

Finally, the ability to go beyond COTS tags expands the scope of applications possible with RIO. Custom-designed RFID tags mimicking different shapes, characters, etc. allow battery-free interfaces to be customized for specific smart spaces use cases in RIO. We describe how these tags can be constructed, and extend the touch/gesture tracking algorithms in RIO to support tracking applications with these custom-designed tags.

1.2.2 TIMU: Battery-Free Motion Sensor

We seek to develop a passive RFID-based tracking system that can achieve (i) high tracking accuracy for both rotation and translation movement, (ii) low cost, and (iii) battery-free. For this purpose, we attach RFID tags to a ball and use a commercial-off-the-shelf (COTS) reader with a single antenna to sense motion information. The system is easy to use and user friendly since RFID tags are cheap, light-weight, and easy to attach to a ball, and a COTS reader with one antenna is widely available.

To achieve high tracking accuracy, we exploit the polarization between an RFID tag and a linearly polarized reader antenna to enable sensing using a *single* reader antenna. Due to RFID polarization, the magnitude and phase of the received signal are significantly affected by the relative orientation and position between the RFID antenna and tag. Therefore, we can use the reflected signal arriving at the RFID antenna during rotation as the signature to estimate the orientation. In order to realize this vision, we decompose the general tracking problem into three more tractable sub-problems: (i) track-

ing rotation given a fixed ball position, (ii) tracking translation movement, and (iii) integrate the rotation tracking and translation tracking for general movement tracking. For (i), we analytically derive the reflected signal arriving at the RFID antenna given the relative position and orientation between the reader and tag by considering the polarization and non-uniform gains of the RFID reader antenna and tags.

We apply our model to derive the received signals during rotation for a given rotation axis. We then search the rotation axis whose estimated signals during a rotation best matches with the measurement. We cast this tracking problem to a non-linear optimization problem and design a deep neural network (DNN) to efficiently find the right initial solution. We further leverage the temporal locality to improve the quality of the solution.

For (ii), we use the phase change to track the relative distance change and use frequency hopping to get the absolute distance. Tracking the angle of arrival (AoA) using a single antenna is more challenging. Existing works require multiple antennas to estimate AoA. We realize one-antenna based AoA estimation by using the same non-linear optimization framework, which leverages the polarization and non-uniform gains in the RFID reader antenna and tags.

Finally, we integrate our rotation tracking with translation tracking to handle general movement involving both rotation and translation. We build a system, called TIMU (Tag Inertial Measurement Unit), which turns COTS RFID Tags into battery-free IMUs. It measures motion parameters, including

rotation axis, rotation speed, 3D position in a battery-free manner, while eliminating the need for an additional communication channel to report the tracked information. By accomplishing this, we enable a single RFID antenna based solution for complex motion state sensing. Using a set of passive RFID tags, TIMU deciphers both translation and rotation motion, even at a relatively higher speed.

1.2.3   RTSense: Battery-Free Temperature Sensor

Inspired by the tag-antenna based sensing and due to the growing popularity of low-cost passive RFID tags, we explore the possibility of using passive RFID tags as temperature sensors. There have been several existing works that use RFID tags to sense motion, such as, tracking [184, 165], activity monitoring [78, 168] or touch sensing [145] using RFID tags. However, temperature sensing is significantly different since it is beyond measuring the length of the propagation path but measuring the physical property of the antenna. We observe, like [65], that temperature change can result in a change in the impedance of the RFID tag, and such a change can be captured using the phase of the received signal reflected by the RFID tag (like [68] with customized tags). Based on this relation, one can potentially map the phase change back to the temperature change.

To achieve reliably more accuracy in temperature sensing, we develop an analytical model that captures the impact of temperature change on the phase of the reflected signal. The model helps us gain insight that larger an-

tenna surface area results in more impedance change, which can be exploited in differential sensing. This opens up the possibility of achieving better resolution by exploiting the antenna surface. To make the system more robust against environmental changes, we use a pair of tags that respond differently to the temperature and measure the phase difference between the two tags. The use of two tags allows us to cancel out the impact of environmental changes since both tags experience the same environmental change. Using these observations, we build the tag-pair by attaching RFID chip transponders to the dipole antennas. This area-based tag-pair design helps us to develop an environment independent way of sensing room temperature, which in turn circumvents the problem of sensing range reduction.

Before arriving into the final design, we experiment with a variety of RFID setups for temperature sensing. We converge to a simple commercial RFID tag coupled with a custom-designed copper dipole antenna-based temperature sensor through experiments. We build a system called RTSense (RFID-based Temperature Sensing) using this tag-pair, which can be easily deployed in the walls of current buildings or future smart-spaces. We also use a specific phase-difference based metric to increase the robustness of the system.

1.3   Contributions

The major contributions of this proposal are summarized as follows:

- We develop a prototype of Rio, and demonstrate its touch and gesture tracking accuracy using both COTS and custom-designed RFID tags. We demonstrate the robustness of Rio through exhaustive real-world evaluations and show that accurate tracking is maintained even at different tag angles and distances to the RFID reader. We also develop two sample applications using custom-designed RFID tags to highlight the flexibility and practicality of Rio. Our evaluations demonstrate that Rio (a) detects a human touch event with 100% accuracy and (b) tracks the location of a human finger during a swipe gesture across the surface of a COTS RFID tag to within $3mm$.

- In TIMU, we develop a passive wireless sensing framework to track different motion state information. We develop a novel algorithm that uses the polarization and non-uniform gain values between the RFID tags and reader antenna to estimate the rotation axis and speed using a *single* RFID reader antenna. To the best of our knowledge, this is the *first* system that senses general motion, including both rotation and translation using a single RFID reader antenna.

- In RTSense, we develop a simple yet accurate model that captures the relationship between the temperature and phase of the reflected signal from an RFID tag. RTSense uses a pair of RFID tags as temperature sensors that are robust against environmental changes. After extensive evaluation, we demonstrate that cheap passive RFID tags can serve as

temperature sensors (can provide up to 2.9 degree centigrade of median error) independent of the distance of deployment and orientation and have a normal read range.

1.4 Proposal Outline

We present a primer on the passive RFID system in Chapter 2 and discuss related work in Chapter 3. We explain *RIO* in Chapter 4. We present *TIMU*, our motion-sensing system in detail in Chapter 5. Next, we discuss the work *RTSense*, the passive RFID-based temperature sensing work, and conclude in Chapter 6 and 7, respectively.

Chapter 2

Background on Passive RFID

Passive RFID system communicates using a backscatter radio link, as shown in Fig. 2.1. The reader supplies a Continuous Wave (CW) periodic signal that persists indefinitely. The passive tags purely harvest energy from this CW signal. The tag then modulates its data on the backscatter signals using ON-OFF keying through changing the impedance on its antenna (Fig. 2.2).
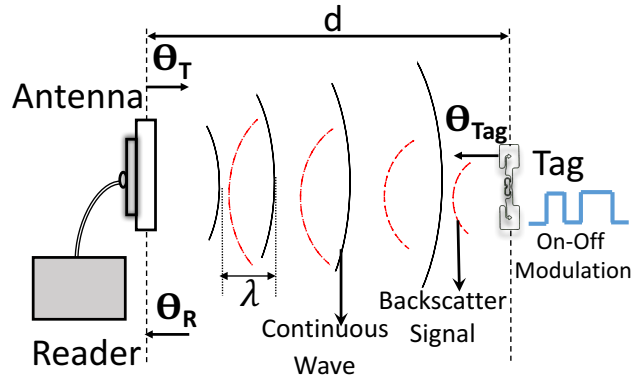
Figure 2.1: Operation of a RFID reader antenna and a tag.

2.1 Protocol

Fig. 2.2 shows a successful read process between the reader and tag. According to the specification [34], an inventory round begins with a *Query*

13

command from the reader that includes a slot-count value Q and other modulation parameters, *e.g.*, link frequency. Each tag receiving *Query* will pick a random value in the range of $[0, 2^Q - 1]$ and load the value as its slot counter to be used as a timer. When the slot counter reaches 0, the tag replies an *RN16* packet, containing a 16 bit pseudo-random number. The reader sends an *ACK* command containing the same *RN16*, and the tag replies its ID back to the reader. If there is a collision, the tag resets its slot-counter again.
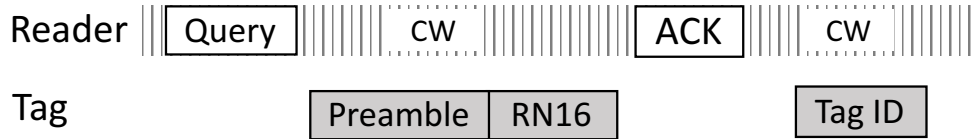
Figure 2.2: Communication process between reader and one tag.

2.2 Passive RFID tag

A typical passive RFID tag, as shown in Fig. 4.2b, consists of an antenna and an integrated circuit (chip). According to [152], passive RFID tag absorbs the most energy when the chip impedance and the antenna impedance are conjugately matched, *i.e.*, $Z_c = Z_a^*$ [134]. So, all off-the-shelf ultra-high frequency(UHF, 860-960 MHz) passive tags come with proper matching [134].

2.3 COTS RFID reader

COTS RFID reader [25] uses linear or circular polarized antennas for both transmitting and receiving. They generally provide facilities to access

14
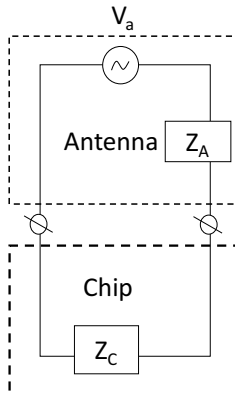
Figure 2.3: Passive RFID tag equivalent circuit.

lower-level information [24] like RSS and phase values etc. through SDK [30]. A COTS reader employs an open-loop estimation (*e.g.*, preamble correlation) or a closed-loop estimation technique for acquiring phase and RSS [35].

2.4 Received Signal Phase

Let r denote the distance between the reader antenna and tag. Therefore, the signal traverses a total distance of $2r$ due to back-scattering. The received phase is not only determined by the distance, but also by the additional phase offsets introduced by the transmitter, tag, and receiver circuits, denoted as θ_T, θ_{TAG} and θ_R, respectively. The total phase change [35] observed by the reader can be expressed as:

$$\theta = (\frac{2\pi}{\lambda} \times 2r + \theta_T + \theta_{TAG} + \theta_R) \bmod 2\pi \qquad (2.4.1)$$

where λ is the wavelength. $\theta_T + \theta_R$ can be expressed as polarization mismatch $2\phi(\hat{r})$ or 2γ. θ_{TAG} can be expressed as $arg(\frac{1}{Z_A+Z_C(OFF)} - \frac{1}{Z_A+Z_C(ON)})$. If we assume $Z_C(OFF) \to \infty$ (*i.e.*, practically very large) [68, 118], then the above equation can be expressed as:

$$\theta = (\frac{2\pi}{\lambda} \times 2r + 2\gamma + arg(-\frac{1}{Z_A + Z_C(ON)})) \bmod 2\pi \qquad (2.4.2)$$

If we measure frequently enough without phase wrap-around, $\theta = \frac{2\pi}{\lambda} \times 2r + 2\gamma + C$, where $C = arg(-\frac{1}{Z_A+Z_C(ON)})$ is a constant. γ is the polarization mismatch angle between the reader and tag antennas. For a linearly polarized RFID reader antenna and tag directly facing each other (*e.g.*, azimuth angle $= 0$), γ is equal to the relative orientation (*e.g.*, $\gamma = 0$ when they are in parallel and $\gamma = \pi/2$ when they are orthogonal). When the azimuth is non-zero, γ is the sum of the relative orientation and azimuth [154, 165].

2.5   Tag Chip Threshold Power

The amount of this harvested power that is transferred to the RFID chip (IC) is P_{chip} [62, 93, 64] can be given by:

$$P_{chip} = (1 - |\Gamma_{tag}|^2)G_{tag}G_tP_t\rho^2(\frac{\lambda}{4\pi r})^2 \qquad (2.5.1)$$

Here, the tag to reader distance is r, the reader antenna's transmission signal power is P_t, G_t is the directional gain of the reader antenna, G_{tag} is the gain

16

of the tag antenna, λ is the wavelength of the signal, ρ is the polarization loss factor (which is the function of mis-match between the reader and the tag antennas), and $\Gamma_{tag} = \frac{Z_C - Z_A^*}{Z_C + Z_A}$. Therefore, with the the change in the physical parameter of interest (Λ), the minimum power required to power the chip can be given by:

$$P_{threshold} \propto (1 - |\Gamma_{tag}(\Lambda)|^2) G_{tag}(\Lambda) P_t \qquad (2.5.2)$$

2.6 Tag Back-scattered Signal's Power Strength

Consider the RFID reader antenna transmits signal at a power of P_t. The transmission power density D_t [62, 93] at the tag at a distance r is as follow:

$$D_t(\theta_t, \phi_t) = \frac{P_t G_t(\theta_t, \phi_t)}{4\pi r^2} \qquad (2.6.1)$$

where $G_t(\theta_t, \phi_t)$ is the directional gain of the reader antenna, and θ_t and ϕ_t are polar measures in the reader antenna's coordinate system.

The tag antenna's intercepted power from this dissipation is given by the expression:

$$P_{tag} = D_t(\theta_t, \phi_t) A_e \qquad (2.6.2)$$

where A_e is the effective area of the tag antenna and expressed by $\frac{G_{tag}(\hat{\theta}_t, \hat{\phi}_t)\rho\lambda^2}{4\pi}$, $G_{tag}(\hat{\theta}_t, \hat{\phi}_t)$ is the directional gain of the tag antenna, λ is the wavelength of the reader's signal, and ρ is the polarization loss factor, which is a function of polarization mismatch between the reader and tag antennas.

17

$\hat{\theta}_t$ and $\hat{\phi}_t$ are polar measures in the tag's coordinate system and ρ can be expressed as $\frac{1+\rho_1^2\rho_2^2+2\rho_1\rho_2cos(\vartheta_1-\vartheta_2)}{(1+\rho_1^2)(1+\rho_2^2)}$ [150], where $\rho_1 e^{j\vartheta_1}$ and $\rho_2 e^{j\vartheta_2}$ are the complex polarization ratios of the reader antenna and the tag antenna, respectively. [1] However, when both the reader antenna and the tag antenna are linearly polarized, the polarization loss factor (ρ) can be expressed as $\rho = cos^2(\gamma)$, where γ is the polarization mismatch between the two antennas. Therefore, for a linearly polarized reader antenna and linearly polarized passive tag antenna pair, Equation (2.6.2) becomes as follow:

$$P_{tag} = (\frac{P_t G_t(\theta_t, \phi_t)}{4\pi r^2})(\frac{G_{tag}(\hat{\theta}_t, \hat{\phi}_t)cos^2(\gamma)\lambda^2}{4\pi}) \qquad (2.6.3)$$

Let P_{tag} denote the power impinged upon tag and P_{chip} denote the amount of harvested power that is transferred to the RFID chip (IC). It can be expressed as follow [62, 93]:

$$P_{chip} = KP_{tag} \qquad (2.6.4)$$

where K is the modulation loss of the tag antenna (the value is less than 1) and depends on the impedance matching between the chip and tag antenna.

Using the free-space Friis' equation model in the reverse side, we get the received power (P_{rec}) as follows (similar to Eq. (5.1.2)):

$$P_{rec} = (\frac{P_{chip} G_{tag}(\hat{\theta}_t, \hat{\phi}_t)}{4\pi r^2})(\frac{G_t(\theta_t, \phi_t)cos^2(\gamma)\lambda^2}{4\pi}) \qquad (2.6.5)$$

---

[1]The absolute value polarization ratio ρ of any antenna depends on the axial ratio A (calculated in dB), which can be expressed by $20log|\frac{\rho+1}{\rho-1}|$.

which becomes Eq. (2.6.6) by substituting P_{chip} in Eq. (2.6.5) by using Eq. (2.6.3) and Eq. (2.6.4) :

$$P_{rec} = P_t G_t(\theta_t, \phi_t)^2 G_{tag}(\hat{\theta}_t, \hat{\phi}_t)^2 K cos^4(\gamma)(\frac{\lambda}{4\pi r})^4 \qquad (2.6.6)$$

This indicates that

$$P_{rec} \propto P_t G_t^2 G_{tag}^2 r^{-4} K cos^4(\gamma)\frac{1}{r^4} \qquad (2.6.7)$$

Therefore, the back-scattered power received at the reader antenna is related to the gain of both tag and reader (G_{tag} and G_t), the reader's transmission power (P_t), the polarization loss factor ($cos^2(\gamma)$), the wavelength of the transmitted wave (λ), the distance (r) and modulation loss factor (K). When the tag is moving in a specific geometric configuration, all factors, except P_t and λ, change. To accurately model the geometric configuration change caused by movement, one must first model all these factors and then deduce the probable received signal strength at the receiver side (P_{rec}).

Chapter 3

Related Work

In this section, we present related works on wireless tracking, localization, sensing, and other adjacent applications. However, here, we mainly focus on RFID based tracking and sensing techniques. In each of the sub-topics, we explain the novelty of our systems.

3.1 RFID based Tracking and Sensing

The core idea of using RFID tags as an input mechanism or sensor is not new. Researchers have used either tag with micro-controllers [157] or passive tags in a COTS or custom setup. In the following, we explore the main research trends using RFID technology.

RFID tags are used to recognize gestures or activities based on distinct phase and Received Signal Strength (RSS) signatures. Researchers [209, 55] have implemented a matrix of RFID tags with multiple antennas to detect gestures. Recently, a few systems [78, 53] have used machine learning to mine the phase data for predicting fine-grained exercising activities. For example, Amandola *et al.* [53] detects multiple body segment movements using passive RFID tags. Kriara *et al.* [104] uses RFID based gesture recognition to

pair related objects which can help in exciting gaming applications. Furthermore, researchers [95, 168] have also exploited the doppler frequency shift of tag movement to detect individual customer behaviors like gazing or picking activities. RIO is orthogonal to such works as it targets fine-grained swipe tracking over a smaller area. RIO can be deployed in conjunction with such activity recognition techniques for a comprehensive IoT environment.

Initial attempts have used RSS to calculate the distance between the reader and the tag [130, 166, 156, 201]. However, due to its unreliability [90], researchers have exploited phase information for better tag positioning [111, 182, 198]. Angle of Arrival (AoA) based approaches [97, 132] are impacted by Non-Line of Sight (NLOS). Whereas, NLOS resilient Synthetic Aperture Radar (SAR) inspired approaches create a RF map by multipath profile [182, 180, 164] or hologram [127, 198] or phase profile [167] to achieve median error upto 1 cm [198]. For example, *BackPos* [111] has proposed a hyperbolic-based positioning system using phase information with multiple RFID reader (≥ 3) antennas with 13 cm median error. The technique of *PinIt* is further applied in robot object manipulation [180] using a set of pre-deployed reference tags. Moreover, Miesen *et al.* [127] employs the moving antenna to construct SAR and find out the tag's location with naive hologram. Unlike RIO, these methods employ multiple antennas or moving the reader to locate the tag(s).

Wang *et al.* [184] track tag movement with 8cm median error by using customized 8 antennas. Moreover, *PolarDraw* [165] uses two linearly polarized COTS antennas and exploits polarization property to track a RFID tag. How-

ever, *Tagball* [110] employs extended kalman filtering (EKF) [160] technique on collected phase information to create a 3D mouse with 12 tagged object. Fishkin *et al.* [82] has been able to use passive UHF RFID tags as a sensor for detecting rotational motion using multiple readers. Another approach of RFID tag tracking is based on proximity [91, 197, 112]. When the target tag enters in the radio range of an antenna, its location is assumed to be the same as this receiver. Furthermore, *Tagyro* [188] exploits phase information of multiple tags to get the orientation of the object with a median error of 4 degrees. Another recent work [85] uses a chip-less tag with a Wi-Fi based customized setup to detect human-object interaction. Rio is an evolution of such systems into one that enables robust fine-grained tracking on 2D surfaces using only a single antenna.

Early works [57, 121] use active tags as power-free buttons. Li *et al.*[108] use a single antenna to enable motion detection in their object interaction detection system called IDSense. It uses a Support Vector Machine (SVM) with a Radial Basis Function (RBF) kernel to detect five classes of tag interactions using PHY-layer features (RF Phase, RSSI, read rate, etc.). The SVM is trained using 600 interaction instances and achieves up to 97% accuracy. PaperID [107] is a similar work that uses supervised machine learning to detect 5 types of on-tag and free-air interactions with custom-designed RFID tags. It achieves a 94% accuracy (testing done by 5 users) by using the trained model from 150 instances at different locations. Rio improves upon these works by achieving high accuracy (4% error rate) using off-the-shelf hardware and an

extremely low training overhead (only 4 swipe instances required).

In the following Table 3.1, we highlight a set of prominent tracking and sensing systems presented in the literature.

System	Goal	Key Innovation	Limitation
RFind [115]	Fine-grained tag tracking	Large bandwidth use	Custom USRP setup with off-line tracking
Tagoram [198]	Precise tag positioning	Exploiting the phase profile	Specific use case with antenna array
RFCompass [180]	Robot object manipulation	SAR technique to build multi-path profile	Coarse-grained tracking possible
PolarDraw [165]	Tag movement tracking	Exploits polarization of passive tag	Recognizes only fixed alphabet
PaperID [107]	Object Interaction	Custom tag design	Huge amount of training needed
LiveTag [85]	Touch Detection	Chip-less tag compatible with WiFi	Limited range with extensive calibration
IDSense [108]	Object Interaction	First COTS single antenna solution	Detects only limited set of user actions
Tagyro [188]	3D orientation detection	Use of phase information of multiple tags	Needs extensive initial calibration
Femo [78]	Exercise activity tracking	Exploiting phase and RSS information	Limited number of activities after extensive training

Table 3.1: Summary of a few passive RFID based tracking systems.

3.1.1   Passive RFID-based environment sensing

Marocco et al. [125, 123] observes that the change in tag signal RSS and phase due to change in tag antenna performance is related to the change in the environment. This observation underpins passive RFID tag-based analog sensing, which embeds the sensed variable through their RF response. For

example, RFID tag designs used to measure temperature [54, 128], relative humidity [63, 117, 119], and gas presence [137]. Smith *et al.*[143] proposes building switches by connecting ICs with different IDs to the tag antennas. These mechanisms can either be based on chipped or chip-less tags, within a COTS or customized setup [202]. In a COTS setting, authors build a multiple-tag based system [71] to detect the water level in a container is detected by exploiting the ON-OFF switching. However, unlike RTSENSE, these works do not robustly enable fine-grained environmental sensing. Similar to ours, [178] proposes a COTS tag-pair approach with an implanted sensor but suffers from a limited sensing range, resolution, and robustness.

Moreover, [196] creates custom-designed RFID tags that embed a small amount of distilled water, making their wireless response temperature sensitive. [170] uses a bimetallic strip with a tag's antenna to detect displacement. Authors also build customized tags exploiting the impedance change property, to sense on-body temperature [54, 128], relative humidity [63, 117, 119], and even, gas presence [137]. Smith et al. [143] build novel switches by connecting ICs to different tag antennas. The authors in [158] design a custom back-scatter circuit to use the tag antenna for sensing purposes. This work [58] proposes the use of a specific patch-antenna design for temperature sensing, which is unlike RTSENSE not compatible with a COTS setup. All these approaches require custom tag designs in a wired setup, making them relatively expensive and less practical. These works though propose [70, 124] a few setup-independent metrics like AID but are limited to the chemical presence

and relative humidity [68] sensing.

3.1.2 Battery-assisted RFID based environment sensing

Authors in these works [57, 121] use active RFID tags as input buttons. Researchers have also used active tags with microcontrollers [158] for the sensing purpose. In this active tag-based setup, the sensed parameter is stored on the tag chip memory, which will be forwarded to a specific reader. Examples include the RFM3200, a wireless flexible temperature sensor from RFMicron Inc. [15], WISPs [202] and Ekhonet [205]. The need for writing into the tag memory makes tag costly and there is a need of customized readers. For example, temperature-sensing tags from RFMicron cost about 30 USD. In contrast, RTSENSE used inexpensive passive RFID tags that cost only about 0.03 - 0.05 USD each. Unlike these works, we propose a simple COTS tag-pair design exploiting the antenna surface area for *analog sensing* of temperature. Moreover, we also propose phase-based metric to improve the resolution, range, and robustness.

3.2 Other Sensing and Tracking Techniques

Apart from battery-free passive RFID tag driven techniques to sense or track, there are different other modalities available in the literature.

3.2.1 IMU, Wearables, and Camera based Motion Tracking

In mobile and wearable devices, the state-of-the-art orientation sensing is probably achieved by A3 [208] and MUSE [169]. Compared to the orientation, tracking moving distance with inertial sensors is a relatively more challenging endeavor. Prior works only track coarse-grained inertial distance for short-time motion, by counting steps and estimating step lengths [176, 200]. However, low-cost inertial sensors are hardly able to track precise distance [98].

Recently, researchers in [80, 83, 84, 126, 89] embed IMUs in a cricket ball to extract relevant features such as angular velocity, time of flight, ranging etc. Moreover, [100] measures spin-analytics in the context of a bowling ball. Different startups like Zepp, Mi Coach, and Ball are extracting the players' motion patterns using wearables. Hawk-Eye [9] uses camera-based tracking technology for fine-grained ball tracking, which has been officially included in Cricket, Tennis, etc. Furthermore, Hot Spot [11] is another popular IR technology used to determine contact points between ball and players.

3.2.2 Other Wireless Techniques for Tracking and Sensing

Numerous efforts have been devoted to wireless tracking and sensing during the past decades. Many existing works employ different channel parameters for tracking, such as Angle of Arrival (AoA) [101, 105, 194], Time of Flight (ToF) [87, 161], or their fusion [192, 146]. The latest of them [103] pushes the accuracy to sub-centimeter level. These approaches, however, usually require

a large phased array or a large frequency bandwidth, typically together with clear Line-Of-Sight (LOS) condition, to achieve good performance. Efforts have been made to expand bandwidth by frequency hopping [191, 175] and extend antenna array [193], which however incur extra spectrum or hardware overhead. In addition, the existing works require cooperation across multiple APs (four or five) [194, 101, 106] A few prior proposals attempt to track using a single AP, which again, still need precise AP location and orientation [29,35], or achieves decimeter accuracy [161, 175]. Moreover, many of the existing works degrade or fail in NLOS conditions.

Other related leverage fingerprinting of dense APs [59, 149, 163]. [141] employs Channel Impulse Response (CIR) for movement detection but does not address motion tracking. Centimeter granularity fingerprinting is studied using CIR [190], which is further enhanced by multiple antennas [74] and by frequency hopping [73]. These proposals require exhaustive calibration before deployment and deteriorate due to temporal dynamics. Moreover, the emerging 802.11mc [21] and Bluetooth 5.1 [5] standards provide round trip time and AoA measurement respectively. Both of these strategies, however, offer limited accuracy, especially in indoor environments.

Chapter 4

RIO: RFID based Touch Interface

In this chapter[1], we explore the design of a battery-free fine-grained touch gesture input interface leveraging passive Radio Frequency IDentification (RFID) technology. Specifically, we improve upon existing works by asking and answering an important question: *Can we use commercial off-the-shelf (COTS) RFIDs as a battery-free, low-cost, fine-grained touch-based user input primitive?* (Fig. 4.1a),

4.1 Overview

In this chapter, we design and build such an input primitive using COTS RFID readers and tags. We call this primitive Rio, for **R**FID-based **I**nput / **O**utput. Rio turns COTS RFID tags into touch interfaces: a user interacts with Rio by touching the tag, and Rio accurately tracks the touch

---

[1]This chapter is based on the following published work: *Swadhin Pradhan, Eugene Chai, Karthikeyan Sundaresan, Lili Qiu, Mohammad A. Khojastepour, and Sampath Rangarajan. 2017. RIO: A Pervasive RFID-based Touch Gesture Interface. In Proceedings of the 23rd Annual International Conference on Mobile Computing and Networking (MobiCom 17). Association for Computing Machinery, New York, NY, USA, 261274. DOI:https://doi.org/10.1145/3117811.3117818.* I am the principal author of this publication who is primarily responsible for formulating the problem, coming up with the solution, performing the extensive evaluation, and writing up the paper.

(a) Rio-enabled home setup. (b) Custom Rio tag for volume control.
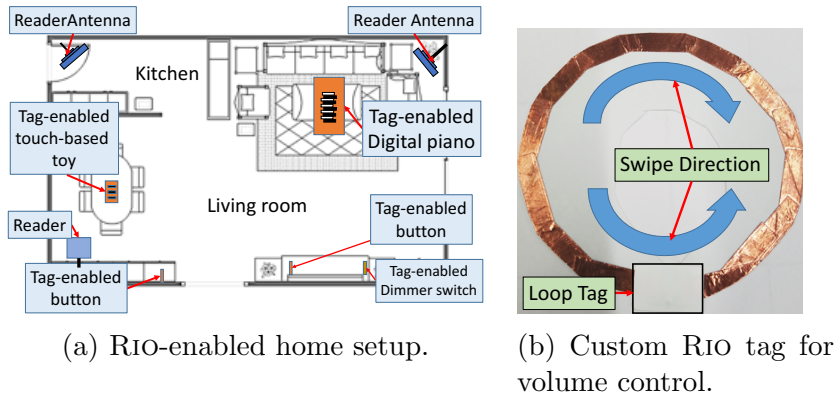
Figure 4.1: Example applications of Rio.

as it moves over the surface of a tag. Rio uses a novel technique of *impedance tracking* in back-scatter communications. The human body is conductive, with a capacitance on the order of hundreds of picofarads (pF) and a resistance of hundreds to thousands of Ohms [52, 99]. When a user touches an RFID tag, his/her body conductivity changes the effective *impedance* of the tag antenna. This impedance change manifests as a change in the phase of the back-scattered signal. Rio tracks this phase change to determine the location of the finger within a tag. By accurately modeling the relationship between impedance and RF phase, this fine-grained tracking can be achieved with minimal training overhead. Our evaluations show a tracking error of under 4% with only 4 training events (vs. 600 training events for IDSense [108]).

Rio offers three key features that make it ideal for IoT setting:

(i) Fine-Grained Accuracy. Rio detects finger taps on RFID tags with 100% accuracy, and tracks finger swipe positions to within $3mm$ of its correct position (validated using a camera and OpenCV for finger tracking). This

is achieved using off-the-shelf RFID tags, thus enabling a new battery-free, fine-grained and accurate UI primitive for smart-spaces.

(ii) Low-cost Hardware. RIO makes use of COTS RFID tags. We have tested RIO with a variety of tags, an example of which is the Monza 4D Dogbone tag [33]. These tags are extremely low-cost and can be purchased for as low as 14-cents each. The low-cost nature of RFID tags lowers the barrier to smart spaces as large numbers of tags can be installed within an area easily.

(iii) Customizable User Interface. RIO also supports custom-designed RFID tags. We build tags with custom-shaped antennas by laying out the antennas with copper metal tape and inductively couple them to small near-field RFID tags. RIO tracks touch gestures over these custom antennas, and thus enables custom, application-specific interfaces to be built.

In the following, we describe the details of RIO.

4.2   Human Touch Primitive

Human touch on the RFID tag changes the effective impedance of the antenna, and will, in turn, influence the phase of the back-scattered signal. In this section, we show how this phase-change behavior is used as a reliable and robust primitive for touch/gesture tracking in both single tag and multi-tag settings, and in the presence of artifacts such as multi-path and inter-tag coupling. We accomplish this with the help of both controlled and over-the-air measurements, and an analytical model that highlights the fundamental
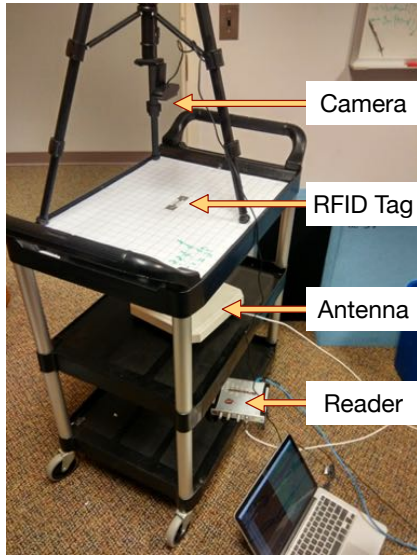
(a) Equipment setup.

(b) Monza R6 Dogbone RFID tag.

Figure 4.2: Equipment and tags used in the swipe experiment.

relationship between impedance change and the RF phase.

4.2.1 How Does Human Touch Change the Backscatter Phase of a Single RFID Tag?

Fig. 4.2a illustrates the measurement setup that is used to study the touch-induced performance of the RFID tag. We attach a single RFID tag that is $1.5 \times 10cm$ in size (shown in Fig. 4.2b) on a flat surface, and place a $9dBi$ circularly polarized RFID antenna $50cm$ directly below it. An Impinj R420 RFID reader powers the antenna. The camera in Fig. 4.2a only used in later sections for accuracy measurements. For clarity, we divide the tag into 9 equal subsections, as shown in Fig. 4.2b. Position 5 corresponds to the middle, while 1 and 9 are at the two ends of the tag.

(a) Simple touch.   (b) Swipe on surface.   (c) Swipe along edge.
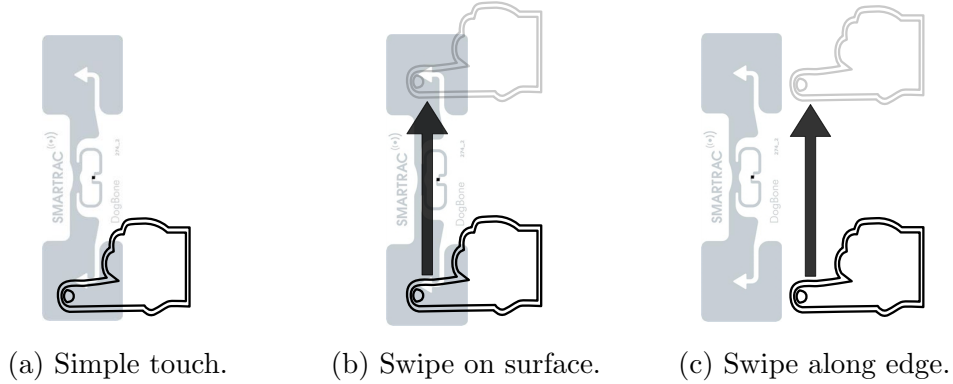
Figure 4.3: Touch gestures.

We perform three gestures, as illustrated in Fig. 4.3: a simple touch gesture where we touch one end of the tag (Fig. 4.3a), a swipe gesture where we start with a finger on one end of the RFID tag and move across the length of the tag at constant speed (Fig. 4.3b), and a swipe gesture that is performed along the edge of the tag but without touching the tag itself (Fig. 4.3c). The RFID reader continuously queries the RFID tag during the entire swipe gesture at a rate of ~200 reads/second. We use the Octane SDK [30] together with the Impinj R420 reader to obtain the phase and magnitude of the back-scattered responses from the RFID tag. We make four observations from our experiments:

(1) Human touch induces significant phase changes in the back-scattered response. Fig 4.4a shows the back-scattered phase of the RFID tag when a simple touch is applied from 1 to 3 seconds after the start of the experiment. Observe that during this time interval, the back-scattered phase jumps from 3.5 to 4.8 radians. The signal phase returns to 3.5 radi-

(a) Simple touch at 1 to 3 sec.　　(b) Swipe gesture.
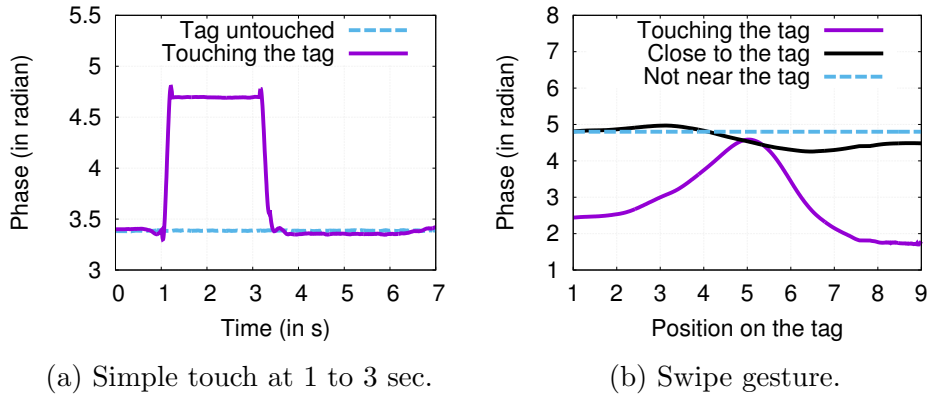
Figure 4.4: Phase of backscattered RFID signals.

ans once the touch is removed. This phenomenon demonstrates that a simple touch will induce a significant phase change (1.3 radians in this experiment). It is a simple method to detect a touch gesture on an RFID tag. This amount of phase change varies between tags and can either increase or decrease in response to human touch.

(2) A swipe gesture induces different phase changes as the finger moves over the tag. Fig. 4.4b shows the absolute backscattered phase under the two different swipe gestures. Observe that with the swipe gesture over the RFID tag, the amount that the phase changes compared to an untouched tag varies depending on the position of the finger. This phase trend follows a symmetrical bell-shape, with about 3 radians between the highest and lowest phases, and starting from one end of the tag, the largest phase-change is seen when the swipe crosses its middle.

(3) Human touch is the dominant cause of phase changes.

(a) Tag behind a wall.   (b) Tag behind door.
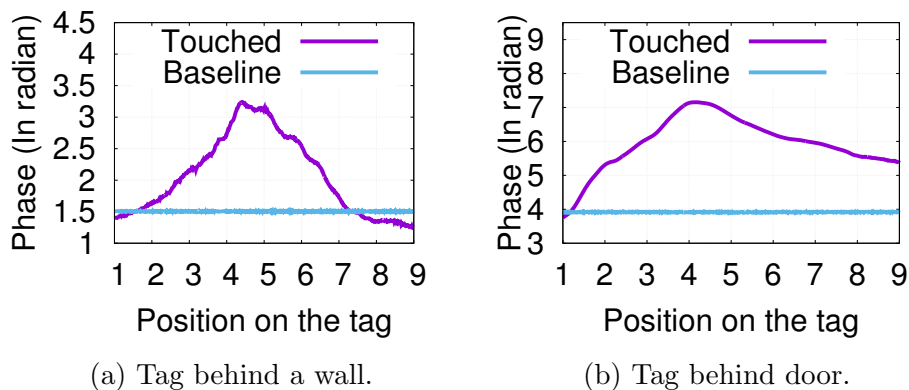
Figure 4.5: Phase-change pattern of backscatter signals with tag in NLOS locations.

Fig. 4.4b also shows the phase of the back-scattered signal when the swipe gesture is performed without touching the antenna on the tag. Observe that *while some phase changes are present, they are much less significant than when the touch gesture is performed directly on the tag.* This observation, together with the measurement under NLOS conditions, shows that the dominant effect due to human touch can be measured under varying channel conditions.

(4) Phase behavior is resilient to multi-path. In order to study the effect of non-line-of-sight (NLOS), we repeat the swiping gesture but with the tag and reader in different positions by separating them with (a) a wall, and (b) a door. The reader and tag are $2m$ apart. Under such conditions, the indirect signal paths and associated multi-path distortion have a more significant impact on the back-scattered signal. Note that the maximum range at which an RFID tag can be read depends on both the RFID reader and the tag. Our Monza R6 tags have a theoretical maximum read range of over $6m$,

but practically, this limit is close to the $2m$ used in our NLOS experiment.

Fig. 4.5 shows the phase of the back-scattered signal under these two conditions (labeled *Touched*). The *baseline* plot shows the RF the phase of the RFID tag without any human contact. Observe that *even in NLOS situations, the bell-shaped phase change behavior seen earlier is maintained.* Hence, even though multi-path and NLOS effects can influence the RF phase readings, the impact of human touch on the phase of the back-scattered the signal is dominant.

4.2.2   Why Does the Backscatter Phase Change with Human Touch?

The human body can be modeled as an electrical circuit with an equivalent resistance and capacitance [75]. In particular, the human skin has a capacitance equivalent to hundreds of picofarads (pF) [99]. When a human touch is established with the RFID antenna, *capacitive coupling* [61] is established between the human and the RFID antenna at the point of contact. We explain the impact of this coupling and verify its influence on the back-scatter phase through real-world VNA circuit measurements.

4.2.2.1   Capacitive Coupling

The radiation of RF signals from the RFID tag antenna is the result of time-varying current induced within the antenna. A change in the phase of this current will induce a corresponding phase change in the associated RF radiation [155, 67]. Hence, to understand how the phase of the back-scattered

signal changes, it is helpful to know how the phase of this induced current is affected by touch. The RFID tag in our experiments uses a *dipole antenna* [172] for backscatter communications. Using a simplified model of dipole antennas, the current induced in the RFID antenna can be mathematically expressed as [67]

$$I_m = -\frac{E_{\text{inc}}}{(Z_C + Z_A)\gamma \cos^2(\gamma L/4)} \qquad (4.2.1)$$

where Z_C and Z_A are the impedances of the RFID chip and antenna, respectively, E_{inc} is the incident electric field on the RFID antenna, L is the length of the antenna, and γ is the free-space phase constant. If the effective impedance of the antenna Z_A is changed, (4.2.1) shows that the induced current, and by extension, the back-scattered electric field and signal, will undergo a corresponding change in phase and magnitude [172]. However, *how does human touch change the antenna impedance?*

Through capacitive coupling, the human body becomes an extension of the RFID antenna. The effective impedance of the RFID antenna, Z_A, as presented to the RFID chip, is now a sum of the impedance of the antenna without human touch and the impedance introduced by the human finger. A change in phase in this effective impedance will cause a corresponding phase change in the current distribution within the antenna. As a result, the phase of the back-scattered signal changes in response to human touch.
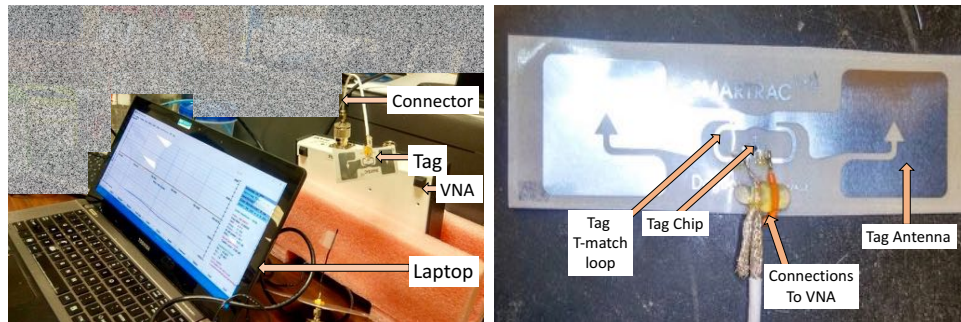
(a) VNA experimental setup.

(b) Customized Dogbone RFID tag for VNA experiment.

Figure 4.6: Vector Network Analyzer (VNA) measurement.

4.2.2.2 VNA Measurements

We directly measure this the impedance change due to human touch using an Array Solutions Vector Network Analyzer (VNA) [23]. We use the same RFID tag from Fig. 4.2b, but disconnect the RFID chip from the antenna, and solder the feed points of the RFID antenna directly to the electrical leads of the VNA. Fig. 4.6b shows the modified tag used for our VNA measurements. Using this setup, we can induce electrical currents within the RFID antenna, and directly measure the impedance in the antenna.

We again divide the tag into 9 equal subsections and measure the antenna's impedance when a human touch is applied to each of the 9 points. Fig. 4.7 shows the magnitude and phase of this measured impedance. Observe that the impedance change also follows a symmetric bell-shaped pattern, with the largest magnitude and phase changes occurring when the human touches the middle of the tag.
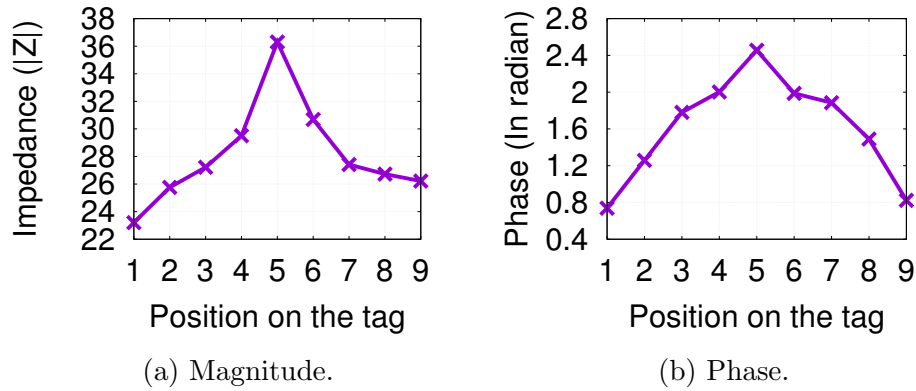
Figure 4.7: Tag impedance change due to human touch.

4.2.3 Human Touch on a Multi-Tag Array

Mutual coupling between one or more RFID tags nearby can distort the phase and magnitude of the back-scattered signal during a swipe gesture [174, 29]. For example, Fig. 4.8a shows the phase trends of four swipe events over a single RFID tag when (a) there are no other tags nearby, and (b) three examples when there is one other tag, placed $5mm$ away from it.

Observe that due to mutual coupling, the phase can even be almost invariant at several tag locations when one other tag is adjacent (e.g., positions 6 to 9 in Fig.4.8a for "w/ adj tag 3"). In the other two swipes with adjacent tags, the dynamic ranges of phase changes reduce to around 0.9 radian. This phenomenon is equivalent to a reduction in the signal-to-noise ratio (SNR) of the phase data obtained by the RFID reader. Furthermore, Fig. 4.8b illustrates that dynamic range of phase change in both halves of the curve for mutual coupling scenarios is on an average 1 radian less than the case when no tag is

38
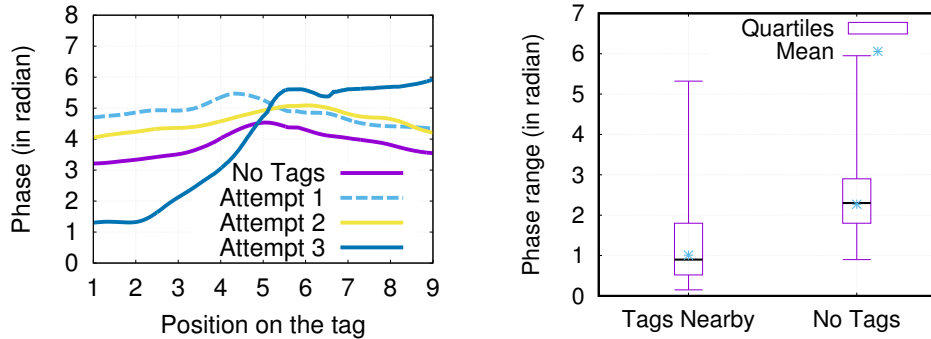
(a) Mutual coupling distorts swipe phase behavior. (b) Mutual coupling reduces dynamic range of phase change.

Figure 4.8: Phase behavior with or without nearby tags.

nearby. This reduction poses a challenge for RIO as a low SNR phase data is correlated with worse finger tracking accuracy.

To overcome this challenge, we now try to understand how mutual coupling between tags affects our primitive.

4.2.3.1   Inverted Phase Behavior

Our experiments show that due to mutual coupling when a human touch is applied to a tag, the *trend* of its phase change is the *opposite* of those seen in adjacent tags.

Fig. 4.9 shows the tag layout used in this experiment, with each pair of adjacent tags separated by $5mm$. To highlight the effect of mutual coupling, we consider only three tags in this array, labeled $i - 1$, i and $i + 1$. We swipe across tag i and record the phase of tags $i - 1$, i and $i + 1$.

Fig. 4.11 shows the phase of the back-scatter signal measured from
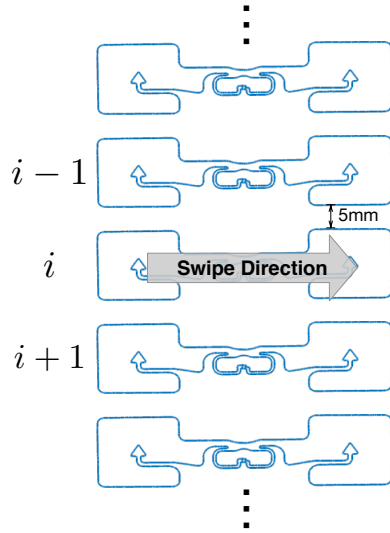
Figure 4.9: Tag array for coupling measurement.
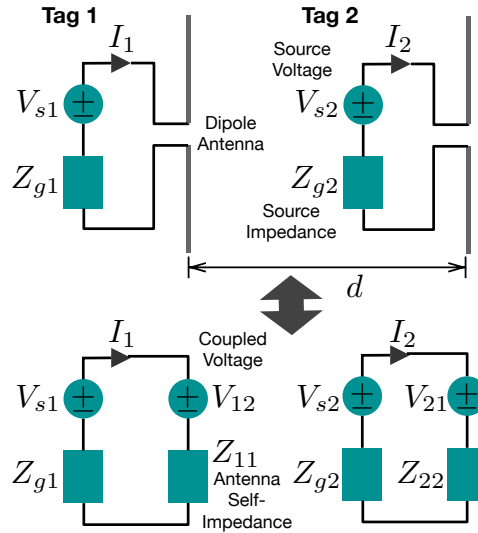
Figure 4.10: Equivalent circuit of tags 1 and 2.
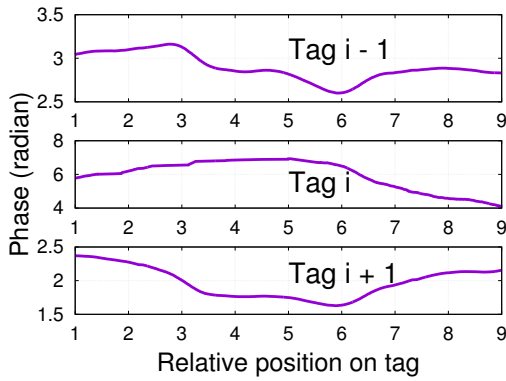
Figure 4.11: Phase change trends in tags $i - 1$ and $i + 1$ are the inverse of tag i.
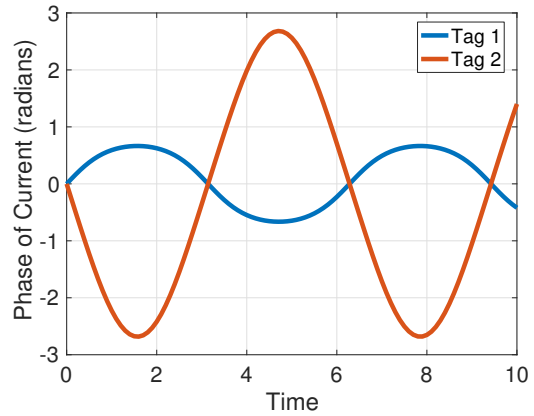
Figure 4.12: Phase of induced current in tags 1 and 2.

these three tags. Observe that due to mutual coupling, tag i experiences a smaller range (around 2 radian lesser) of phase variations during the swipe gesture. However, the trend of the phase changes show an interesting pattern: observe that as the swipe gesture moves across tag i, an increase in its phase coincides with a decrease in the phase of tags $i-1$ and $i+1$. We refer to this phenomenon as the *inverted phase behavior of adjacent tags*. The impact of such mutual coupling diminishes as we consider tags that are farther away than the adjacent tags.

4.2.3.2 Why is the trend of phase changes in adjacent tags inverted?

Model: To understand the impact of mutual coupling on tag interaction, we model the basic scenario of coupling between two tags. The equivalent circuit of the two tags can be represented as shown in Fig. 4.10. Here, V_{s1} and V_{s2} are the equivalent source voltages induced by the reader's signal on the tag antenna, with Z_{s1} and Z_{s2} being the corresponding chip impedances, and Z_{11} and Z_{22} being their respective antenna self-impedances.

The current in tag 1, I_1 induces a magnetic field, which couples tag 1 and tag 2, thereby inducing a coupled voltage in tag 2, V_{21}, where $V_{21} = I_1 Z_{21}$, and Z_{21} is the mutual impedance in tag 2 due to tag 1. Similarly, we have the coupled voltage in tag 1 as $V_{12} = I_2 Z_{12}$. Now, taking mutual coupling into account, the resulting voltages, for tag 1 and tag 2 respectively, can be written

as,

$$I_1(Z_{11} + Z_{s1}) = V_{s1} + I_2 Z_{12}$$

$$I_2(Z_{22} + Z_{s2}) = V_{s2} + I_1 Z_{21} \tag{4.2.2}$$

When a tag is interrogated, the back-scattered field (signal) from a tag is a function of the current in the tag. Hence, it suffices for the analysis to focus on the currents in the two tags to understand how interacting with one tag changes the current in the mutually coupled tag. Solving for the two currents in Equation 4.2.2, we get,

$$I_1 = \frac{V_{s1}\tilde{Z}_{22} + V_{s2}Z_{12}}{\tilde{Z}_{11}\tilde{Z}_{22} - Z_{12}Z_{21}}; \ I_2 = \frac{V_{s2}\tilde{Z}_{11} + V_{s1}Z_{21}}{\tilde{Z}_{11}\tilde{Z}_{22} - Z_{12}Z_{21}} \tag{4.2.3}$$

where $\tilde{Z}_{11} = Z_{s1} + Z_{11}$ and $\tilde{Z}_{22} = Z_{s2} + Z_{22}$.

Phase Change during Tag Interaction: Note that we are interested in modeling the *change in phase* of the signal received by the reader when a user is interacting with the tag being interrogated or a nearby tag. When a tag is interrogated, the signal received by the reader is a combination of the back-scattered signal from the desired tag as well as the scattered signal from the other tags (which serve as simple scatterers). We will assume that the contribution of the scattered signals is negligible relative to that of mutual coupling from nearby tags. In this case, the phase of the received signal can be estimated from the phase of the current of the back-scattered signal, while accounting for mutual coupling with nearby tags. The phase of the currents in the two tags, I_1 and I_2, can be written as,

$$\angle I_1 = \phi_1 - \phi_m, \text{ and } \angle I_2 = \phi_2 - \phi_m \tag{4.2.4}$$

where ϕ_1, ϕ_2 and ϕ_m are the phases of $(V_{s1}\tilde{Z}_{22} + V_{s2}Z_{12})$, $(V_{s2}\tilde{Z}_{11} + V_{s1}Z_{21})$, and $(\tilde{Z}_{11}\tilde{Z}_{22} - Z_{12}Z_{21})$ respectively.

Now, let us consider the case when the user interacts (touching or swiping) with tag 2. This will change the self impedance of Z_{22} as well as its coupled impedance Z_{12} on tag 1, while the chip impedances Z_{s1}, Z_{s2} and tag 1's self (Z_{11}) and induced (Z_{21}) impedances will not change. Hence, while phases ϕ_1 and ϕ_m will change, ϕ_2 will remain constant. The phase-change behavior can now be captured as,

$$
\begin{aligned}
\angle I_1(t) &= \phi_1(t) - \phi_m(t) \\
\angle I_2(t) &= \phi_2 - \phi_m(t) \\
\text{where, } \phi_1(t) &= \angle(V_{s1}Z_{s2} + V_{s1}Z_{22}(t) + V_{s2}Z_{12}(t)) \\
\phi_m(t) &= \angle\left(\tilde{Z}_{11}Z_{s2} + \tilde{Z}_{11}Z_{22}(t) - Z_{21}Z_{12}(t)\right)
\end{aligned}
$$

From the above equation, it can be observed that $\phi_1(t)$ and $\phi_m(t)$ are essentially functions of the same impedance changes, namely $Z_{22}(t)$ and $Z_{12}(t)$. However, the change in $Z_{12}(t)$ has an opposite effect in $\phi_1(t)$ compared to that in $\phi_m(t)$. This situation contributes to a counter-acting effect on the phase change of $I_1(t)$ compared to $I_2(t)$ (i.e., tag being touched), and results in the inverted phase-change behavior between the tags. To highlight this impact, we plot the phase evolution of $I_1(t)$ and $I_2(t)$ in Fig. 4.12. Here, $Z_{22}(t)$ is assumed to vary as a sine function during human interaction (for illustration). In contrast, $Z_{12}(t)$ is assumed to vary proportionally to $Z_{22}(t)$ (in both magnitude

and phase), and the rest of the non-varying complex quantities are assumed to be real with unit magnitude.

Thus, while leveraging the primitive for tracking could reduce accuracy in the presence of mutual coupling, the above measurements, and analysis highlight the predictable impact of mutual coupling on our primitive. Hence, by leveraging the phase-change behavior across neighboring tags jointly, our primitive can be made robust to mutual coupling in multi-tag settings.

4.3   RIO Design

Leveraging the above characteristics of the primitive, we now design the algorithms needed to track the human finger's path during a swipe gesture across a single isolated tag and across any individual tag within a tag array. Note that for the sake of simplicity, RIO only tracks a continuous, one-direction swipe across a tag starting from location 1 and ending at 9, as shown in Fig. 4.3b. This is not a fundamental limitation of RIO, and the algorithms can be extended to support arbitrary touch movement within a tag.

4.3.1   Finger Tracking on a Single RFID Tag

Single-tag swipe tracking is done in two stages. RIO first detects a touch event on the tag. Once a touch is detected, RIO uses an online tracking algorithm, RIO-SINGLE, to track a human finger's position across the single tag. A simple, low-overhead calibration is first performed on a tag attached to a surface to determine the precise characteristics of the bell-shaped phase

trend. This calibration overhead is small and needs to be performed only once after the tag is first installed. RIO then uses a tracking algorithm based on *segmental dynamic time warping (SDTW)* [139, 206, 140] that allows for good tracking accuracy with only limited calibration overhead.

4.3.1.1 Low-Overhead Tag Calibration

Tag calibration has to be conducted once after the tag is installed on a surface. During tag calibration, the user swipes his/her finger across the surface of the RFID tag at constant speed (as constant as possible), while the Impinj R420 RFID reader continuously reads the tag at a rate of 200 reads/second, and records the phases of all backscatter responses. RIO *normalizes* the phase responses w.r.t. the lowest value:

$$p(x) = r(x) - \min_x r(x), \quad 0 \le x \le L \qquad (4.3.1)$$

where $r(x)$ is the unnormalized (i.e. raw) phase values at location x from the calibration swipe across a tag of length L. RIO then uses polynomial curve-fitting to find the fourth-order polynomial that best describes the normalized calibration data.

Overhead. This calibration is repeated four (4) times. RIO uses the average of the four polynomial curves in the next touch detection/tracking step. This low-overhead calibration step is (a) *not* user-specific, and (b) only specific to the installed location of the tag. Hence, each installed tag only needs to be calibrated once before touch tracking is enabled for all users after
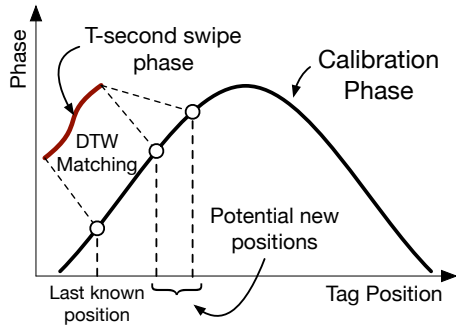
Figure 4.13: DTW search is applied to each window of samples during a swipe.
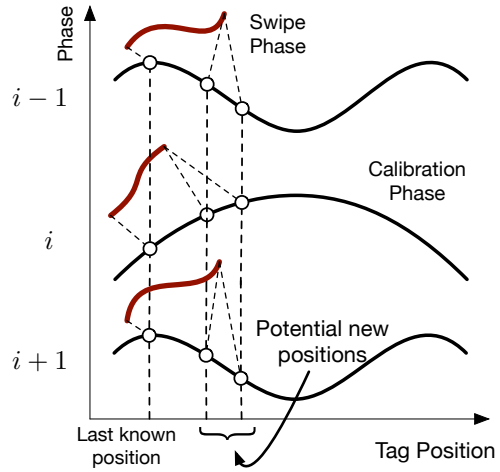
Figure 4.14: DTW search across adjacent tags.

that. Due to human limits, it is not possible to replicate a swipe with a human finger precisely. We have empirically determined that the average of four swipes is sufficient to capture the key behavior of an actual human swipe. We have validated this by having one person calibrate the tag, and evaluating the tracking accuracy of RIO with fifteen (15) other human individuals. Our tracking error remains under 4% for all the sixteen (16) individuals. Note that we do not need to re-calibrate RIO if only the antenna's reading angle or the tag changes. However, if there is some considerable change in the environment (e.g., the introduction of more blockage due to new types of furniture or more dynamic paths due to increased movements of people), we need to re-calibrate to create the primary phase trend to achieve accurate tracking.

46

4.3.1.2 Rio-Single Algorithm

RIO uses a two-stage approach to finger tracking. RIO continuously reads the RFID tag until it detects a touch event. Once a touch has been detected, RIO switches to a tracking stage where it tracks the position of the finger as it is swiped across the RFID tag.

Touch Detection. A touch event results in a significant change in the phase of the response signal from the tag. RIO queries the tag continuously and finds the average signal phase over every time interval of T seconds. If a significant change is seen from a one-time interval to the next (a change larger than a threshold C), then a touch event has occurred, and RIO switches to a tracking mode. RIO uses a threshold of $C = 0.9$ radians, which is empirically determined to provide 100% detection accuracy in real-world conditions.

Touch Tracking. RIO updates the finger's location during a swipe gesture using a segmental dynamic time warping (SDTW) search algorithm. A good overview of SDTW can be found in [140]. Broadly speaking, SDTW compares two sequence segments by stretching and squeezing (*i.e.*, warping) one of the sequences until an optimal match between them is found. The SDTW algorithm returns the measure of similarity between these two sequences at this optimal match.

Fig. 4.13 illustrates how RIO updates the estimated location of the finger in real-time. RIO first collects a sequence of phases of all back-scatter responses over a time window of T seconds. Starting from the previously es-

timated position of the finger, RIO begins a DTW matching by warping the collected sequence and comparing it against multiple *segments* of the calibration phase data. These segments start from the last known position of the finger and have varying lengths that span the range of potential new positions, as shown in Fig. 4.13. The segment with the best match is chosen, and its corresponding end position is taken as the new position of the finger.

This search-and-update step is continuously repeated as RIO tracks the finger over the surface of the tag. The details of the touch detection and tracking algorithms are described in Algorithm 1.

RIO estimates the finger location after every time interval of T seconds. The choice of T determines the latency and processing overhead of each location estimate. In our implementation of RIO, we use $T = 0.5s$ as we have empirically determined it to be suitable for a typical swiping speed. We have evaluated the performance of RIO for other values of T and found the performance to be similar.

In Algorithm 1, RIO performs a DTW search over a range of segment sizes, as specified by $x_{\min}$ and $x_{\max}$ in Algorithm 1. $x_{\min}$ and $x_{\max}$ determine the lower and upper ranges of swipe gesture speeds that will be accurately tracked by RIO. The greater the value of $x_{\max}$ the higher the upper bound of this speed limit. Similarly, the smaller the value of $x_{\min}$, the slower the lower bound on the speed limit. We select $x_{\min}$ and $x_{\max}$ to correspond to $0.5T$ and $1.5T$ seconds of calibration data respectively, which is equivalent to a swiping speed of 10 to $15mm/s$.

Algorithm 1 RIO-SINGLE

1: $x_0 \leftarrow$ current finger location; $x_{\max} \leftarrow$ max finger location w.r.t. x_0;
2: $x_{\min} \leftarrow$ min finger location w.r.t. x_0; $p(x) \leftarrow$ calibration data;
3: **procedure** DTW($\mathbf{a}, \mathbf{b}$)
4:     **return** DTW distance between sequences $\mathbf{a}$ and $\mathbf{b}$;
5: **end procedure**
6: **procedure** MINDTW($x_0, x_1, \mathbf{w}, p(x)$)
7:     $\mathbf{p} \leftarrow \{p(x)|x_0 \leq x \leq x_1\}$;   ▷ Segment of calibration phase data between x_0 and x_1
8:     **return** DTW($\mathbf{w}, \mathbf{p} - p(x_0)$);
9: **end procedure**
10: **procedure** GETPHASEDATA
11:     $t_0 \leftarrow$ CURRENTSYSTEMTIME;
12:     $t \leftarrow t_0$; $\mathbf{w} \leftarrow$ EMPTYVECTOR;
13:     **while** $t \leq t_0 + T$ **do**
14:         $t \leftarrow$ CURRENTSYSTEMTIME;
15:         $\mathbf{w} \leftarrow$ APPEND($\mathbf{w}$, CURRENTPHASEREADING);
16:     **end while**
17:     **return** $\mathbf{w} - \min(\mathbf{w})$;
18: **end procedure**
19: **procedure** UPDATELOCATION($x_0, \mathbf{w}$)
20:     $x_{\text{new}} \leftarrow \arg\min_{x_{\min} < x < x_{\max}}$ MINDTW($x_0, x, \mathbf{w}$);
21:     **return** x_{new};
22: **end procedure**
23: **procedure** TOUCHDETECTION
24:     **while** True **do**
25:         $\mathbf{w} \leftarrow$ GETPHASEDATA;
26:         **if** mean($\mathbf{w}$) $> C$ **then return** True;
27:         **end if**
28:     **end while**
29: **end procedure**
30: **procedure** TOUCHTRACKING
31:     **while** True **do**
32:         $\mathbf{w} \leftarrow$ GETPHASEDATA;
33:         $x_0 \leftarrow$ UPDATELOCATION($x_0, \mathbf{w}$);
34:     **end while**
35: **end procedure**
36: TOUCHDETECTION(); TOUCHTRACKING();

4.3.1.3 Computation Overhead

The computational overhead of finger tracking is dominated by the DTW algorithm, which has a complexity of $O(N^2)$. In practice, Rio samples M equally spaced sample sizes from the range of $x_{\min}$ and $x_{\max}$, and performs a location update (procedure UPDATELOCATION in Algorithm 1) over these M samples. The larger the number of samples M, the finer the tracking resolution. However, the overhead of the corresponding search will also be significantly greater. By default, Rio uses $M = 200$ to achieve high accuracy. However, our empirical evaluations, as shown in Fig. 4.23, show that we can reduce M to 50 with only a slight reduction in accuracy, but gain a $4\times$ reduction in computation delay. With $M = 50$, each full tracking update step can be accomplished in under a second, thus enabling real-time tracking of the finger position. Hence, an interface that is built with Rio can tune M to match the desired accuracy-overhead trade-off.

4.3.2 Finger Tracking on a Multi Tag Array

We consider the tag array layout, as illustrated in Fig. 4.9. Rio tracks a finger on a multi-RFID tag array with two steps. Rio first identifies the tag that the finger is touching, while accounting for mutual coupling. Once Rio determines the tag that is touched, it uses a multi-tag tracking algorithm (using neighboring tags) to continuously localize the finger during the swipe gesture.

4.3.2.1 Tag Calibration

As in the single tag case of §4.3.1.1, calibration has to be performed on the tag array only once after installation. RIO collects and normalizes the phases as the user swipes his/her finger across each tag in the array, as shown in Fig. 4.9. We use $p_1(x), \ldots, p_N(x)$ to refer to the normalized phases from the N tags in the array.

4.3.2.2 Rio-Multi Algorithm

Algorithm 2 RIO-MULTI: Touch Detection

1: **procedure** PHASEDIFF($\mathbf{w}$)
2:     $\mathbf{s} \leftarrow$ LINEARREGRESSION($\mathbf{w}$)
3:     **return** $\max\{\mathbf{s}\} - \min\{\mathbf{s}\}$
4: **end procedure**
5: **procedure** TOUCHDETECT($\mathbf{w}_1, \ldots, \mathbf{w}_N, L$)
6:     **for** $i = 1, \ldots, N$ **do**
7:         $d_i \leftarrow$ PHASEDIFF($\mathbf{w}_i$)
8:     **end for**
9:     **for** $i = 1, \ldots, N$ **do**
10:         **if** $i = 1$ **then**
11:             $m_i \leftarrow \alpha d_i - \beta d_{i+1}$
12:         **else if** $i = N$ **then**
13:             $m_i \leftarrow \alpha d_i - \beta d_{i-1}$
14:         **else**
15:             $m_i \leftarrow \alpha d_i - \beta(d_{i-1} + d_{i+1})$
16:         **end if**
17:     **end for**
18:     $i^{(1)} \leftarrow \underset{i \in \{1, \ldots, N\}}{\arg\max}\ m_i$
19:     **return** $i^{(1)}$
20: **end procedure**

Touch Detection. Touch detection operates on the back-scatter phase from

all N tags over a time window T. We use $\mathbf{w}_1, \ldots, \mathbf{w}_N$ to refer to these N vectors of phase data. Informally, RIO determines the total change in phase encountered by each tag over this time window. It then searches for the tag triple (or tag pair, in the case of the tags at either end of the array) that best demonstrates the *inverted phase behavior* as described in §4.2.3: for a given tag i, the change in phase of its neighboring tags $i-1$ and $i+1$ are the inverse of its own.

Algorithm 2 shows the pseudo-code for touch detection. The PHASED-IFF procedure determines the phase changes over the window of phase data. RIO smooths out the noise in the phase data by fitting the best line through the phase data using linear regression. The phase change of each tag, d_i, is the difference between the two extreme points on the line. RIO computes a weighted sum of the phase change of each tag i and its neighboring tags as $m_i = \alpha d_i - \beta(d_{i-1} + d_{i+1})$. By selecting weights α and β with opposite polarity, RIO can capture the effect of the inverse phase behavior of tag triples (or tag pairs). Empirically, we have found that the touch and tracking accuracy of RIO is best when $\alpha = 0.8$ and $\beta = 0.2$.

Touch Tracking. Once RIO has determined the specific tag that is being touched, it immediately begins reading phase data from that tag i, along with tags that are directly adjacent to it, tags $i-1$ and $i+1$ (if any). Fig. 4.14 illustrates how the segmental DTW search is extended to support two adjacent RFID tags. RIO conducts concurrent DTW searches on these three tags (or two tags, if i is an edge tag), using the same segment sizes for each step in the

52

Algorithm 3 RIO-MULTI: Touch Tracking

1: $x_0 \leftarrow 0$ ▷ Current finger location
2: $\mathbf{w}_1, \ldots, \mathbf{w}_N \leftarrow$ GETALLPHASEDATA
3: $i_{\max} \leftarrow$ TOUCHDETECT$(\mathbf{w}_1, \ldots, \mathbf{w}_N, L)$
4: **procedure** MINMULTIDTW$(x_0, x, \mathbf{w}_{i-1}, \mathbf{w}_i, \mathbf{w}_{i+1})$
5:     $g_i \leftarrow$ MINDTW$(x_0, x, \mathbf{w}_i, p_i)$
6:     $g_{i-1} \leftarrow$ MINDTW$(x_0, x, \mathbf{w}_{i-1}, p_{i-1})$
7:     $g_{i+1} \leftarrow$ MINDTW$(x_0, x, \mathbf{w}_{i+1}, p_{i+1})$
8:     $h \leftarrow \alpha g_i + \beta(g_{i-1} + g_{i+1})$
9:     **return** h
10: **end procedure**
11: **procedure** UPDATELOCATION$(x_0, \mathbf{w}_{i-1}, \mathbf{w}_i, \mathbf{w}_{i+1})$
12:     $x_{\text{new}} \leftarrow \underset{x_{\min} \leq x \leq x_{\max}}{\arg\min}$ MINMULTIDTW$(x_0, x, \mathbf{w}_{i-1}, \mathbf{w}_i, \mathbf{w}_{i+1})$
13:     **return** x_{new}
14: **end procedure**
15: **while** TRUE **do**
16:     $x_0 \leftarrow$ UPDATELOCATION$(x_0, \mathbf{w}_{i_{\max}-1}, \mathbf{w}_{i_{\max}}, \mathbf{w}_{i_{\max}+1})$
17:     $\mathbf{w}_{i_{\max}} \leftarrow$ GETPHASEDATA
18:     $\mathbf{w}_{i_{\max}-1} \leftarrow$ GETPHASEDATA
19:     $\mathbf{w}_{i_{\max}+1} \leftarrow$ GETPHASEDATA
20: **end while**

DTW search. The segment size that best matches the phase data from the three tags will indicate the new finger location.

Algorithm 3 shows the multi-tag tracking algorithm. The MAXMUL-TIDTW procedure performs the multi-tag DTW search jointly on sets of three adjacent tags and combines the results using the weighted metric $h = \alpha g_i + \beta(g_{i-1} + g_{i+1})$ where g_i, g_{i+1} and g_{i-1} is the DTW distance of tag i, $i-1$ and $i+1$ respectively. This metric identifies segments that match the phase pattern in the desired tag and the inverted phase pattern in the adjacent tags to boost the tracking accuracy. The segment identified in the UPDATELOCA-TION procedure is used to update the new location of the finger during the swipe. As before, RIO runs this search-and-update procedure continuously to track the location of the finger.

4.3.2.3   Scaling to Larger Multi-Tag Arrays

RFID readers achieve a constant number of reads/second (200 in case of our Impinj reader), regardless of the number of tags within the read range. Hence, when the array size is enormous, the read rate per tag decreases, which reduces the fidelity of the phase data, and consequently, the accuracy of both touch and gesture tracking. RIO addresses this by utilizing the PHY-layer filtering feature [34] of the RFID Class 1 Generation 2 (C1G2) protocol to read-only subsections of the array at a time. After RIO-MULTI detects the tag that is being touched, RIO applies the RFID filter to read up to eight tags around the tag that is touched (four on either side). The RIO-MULTI touch

54
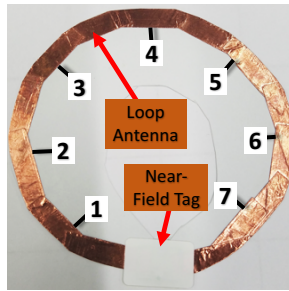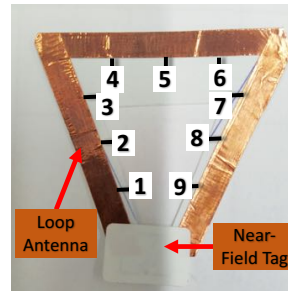
(a) Circle custom tag. (b) Triangle custom tag.
Figure 4.15: Custom-designed RFID tags.

tracking then tracks the swipe gesture on the touched tag.

4.4 Extending RIO with Custom Designed RFID Tags

COTS RFID tags are designed primarily for communications. Hence, the antennas are typically dipole antennas and have sizes and shapes that are carefully tuned to match the RFID chip's electrical impedance [134]. The limited variety in antenna designs restricts the range of user interfaces that can be built using COTS tags. In this section, we discuss RIO's potential by exploring how it can operate with custom-built RFID tags of varying shapes and sizes. This exposition will allow the user interfaces built using our touch primitive to be better customized to the specific demands of smart spaces.

Constructing Custom RFID Tags. We extend RIO to support custom-designed RFID tags, two of which are shown in Fig. 4.15. The antenna of the tags is constructed using a copper metal tape, arranged in shapes that can better mimic familiar control interfaces. For example, Fig. 4.15a shows a circle RFID antenna that resembles a round control knob. A user can swipe in

either clockwise or counter-clockwise directions to adjust the music volume, or light brightness, etc. Owners of the iPod Classic with the click wheel [26] will find this interface familiar. A small near-field RFID tag [22] with an adhesive side is attached to the custom-built antenna, as shown. The antenna forms an inductively coupled connection with the near-field RFID tag, and touching the antenna will result in a familiar phase change in the back-scattered signal.

Antenna Design Space. The antennas shown in Fig. 4.15 are examples of *loop antennas* [151]. We use loop antennas because they have the advantage of being easy to construct in various shapes and sizes. Our demonstration only uses basic shapes (a circle and a triangle), but many other antenna structures such as folded dipoles [114], coil [32] and cloverleafs [77] can be used as building blocks for more complex interfaces.

In order for the antenna to operate at maximum efficiency, the antenna layout must be tuned such that its impedance matches the impedance of the RFID chip. Our custom RFID antennas are designed primarily to mimic real-world control interfaces, and are not impedance-matched to the RFID chip. However, even with this sub-optimality, our experiments show that our custom tags can be read at ranges of up to $1.5m$, which is comparable to the performance of COTS RFID tags $2.4m$.

Tracking on Custom Tags. Fig. 4.16 shows the phase trends when clock-wise and counter-clockwise swipes are performed on the tags (Fig. 4.15). Observe that the phase trends show distinctive patterns and large phase variations (similar to those seen in COTS RFID tags) that can accurately locate

56
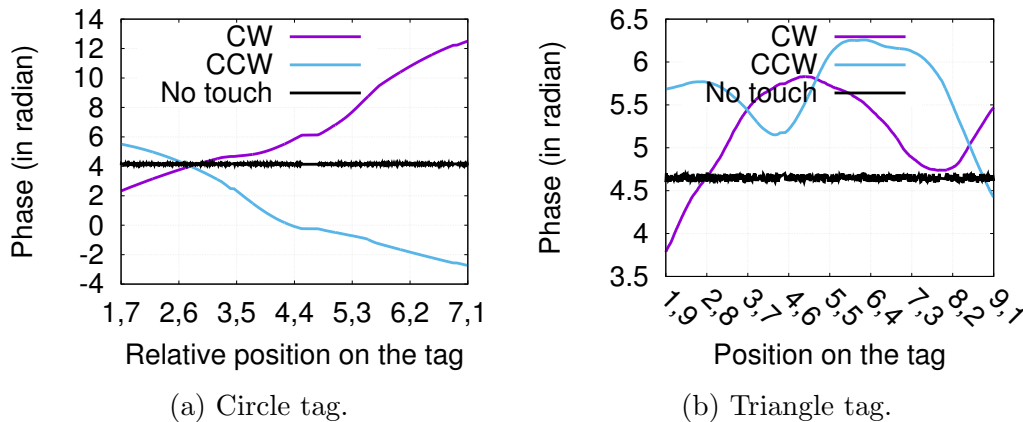
(a) Circle tag.   (b) Triangle tag.

Figure 4.16: Phase trends when a clockwise (CW) and counter-clockwise (CCW) swipe gestures are performed on the custom circle and triangle-shaped RFID tags.

a finger even in the presence of noise. Thus, the single tag tracking algorithm (Algorithm 1) in RIO can also be used to track touch/gesture with these custom tags.

4.5 RIO Evaluation

In this section, we evaluate RIO using the setup shown in Fig. 4.2a. We show the performance of RIO with COTS tags, as well as custom-designed tags, highlighting its robustness as a battery-free UI primitive. We also propose and evaluate two proof-of-concept applications to demonstrate the utility of RIO.

The RFID setup operates as before, where the Impinj R420 reader continuously queries the tags in range (at ∼200 reads/second), and records the RF phase of all RFID responses. We thus have a time series of phase readings for each tag. The camera is time synchronized with the reader control

software so that the video recording is time synchronized with the RF phase measurements. This video footage is used to determine the tracking accuracy.

COTS Tag Layout. We demonstrate the swipe tracking accuracy of RIO using the COTS tags. We use two different tag layouts: a single isolated tag, and a multi-tag array, as shown in Fig. 4.9. This tag layout has two parameters: Tag angle, and distance. *Tag angle:* Fig. 4.2a shows a setup where the tags are placed flat on a surface, which is parallel to the plane of the RFID reader antenna. We tilt the reader antenna by elevating one edge of the antenna to vary the angle of the tag(s) w.r.t. the reader antenna. *Tag distance:* We also elevate the entire tag(s) shown in Fig. 4.2a to vary the distance of the tags to the reader antenna. Experiment results with different tag angles and distances serve to demonstrate the performance of RIO under real-world conditions when the tag is not perfectly aligned with the antenna.

Custom Tags. We also evaluate RIO on custom tags, as described in §4.4. These custom tags are arranged $50cm$ away from and parallel to the reader antenna's surface.

Accuracy Measure. We use OpenCV [31] on the time-synchronized video footage to visually track the finger during the swipe and touch gestures. At any point in time, we compare the finger's location as indicated by the RIO to its actual finger position, as shown by the camera. The tracking accuracy of RIO is reflected in the offset distance (in mm) between these two measurements (RIO and camera).

4.5.1 RIO with COTS Tags

4.5.1.1 Touch Detection

COTS Single Tag. For single-tag detection, we use the phase change threshold $C = 0.9$ as described in §4.3.1.2. With this threshold, RIO achieves perfect touch detection, even under varying tag angles (from 0 to 60°, w.r.t. the reader antenna surface) and tag distances (up to $2.4m$ from the reader).

COTS Multi-Tag Array. Fig. 4.19 shows the detection accuracy when we touch each tag in an array of eight tags. Observe that RIO correctly detects the tag being touched more than 92% of the time. Touch events on tags closer to either end of the array are even correctly detected 100% of the time. Hence, RIO *provides close to perfect tag detection under real-world conditions, with RFID tags deployed in positions within an envisioned smart space.* We expect this accuracy to increase if multiple receive antennas, together with spatial diversity processing (*i.e.,* a multi-static setup) is used.

4.5.1.2 Touch Tracking

COTS Single Tag. Fig. 4.17 shows the tracking accuracy distribution of a swipe gesture when the tags are parallel to and at a distance of $50cm$ from the reader antenna. The swipe is performed at three different speed ranges: slow (less than $10mm/s$), medium (10 to $15mm/s$) and fast (quicker than $15mm/s$). A swipe at each speed range is repeated 100 times on each tag to obtain this distribution. Recall that the DTW window of $0.5T$ to T is chosen for swiping speeds of up to $15mm/s$. Observe that the median location error

(a) Rio-Single.

(b) Rio-Multi.
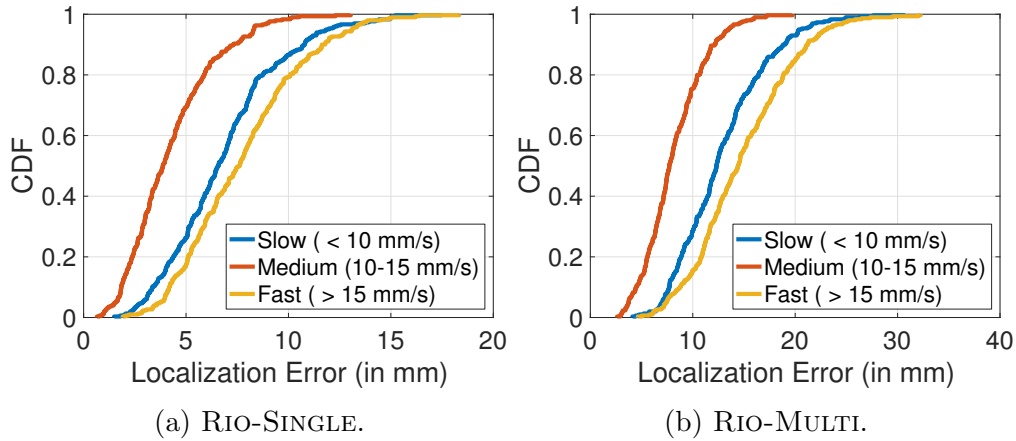
Figure 4.17: Rio tracking accuracy with swipes of different speeds.

(a) Smartrac Monza R5 RFID tag (Tag1).

(b) Smartrac Monza R6 G2IL RFID tag (Tag2).

(c) Alien-9640, Higgs-3 short-dipole paper tag (Tag3).

(d) Alien-9730, Higgs-4 short-dipole paper tag (Tag4).
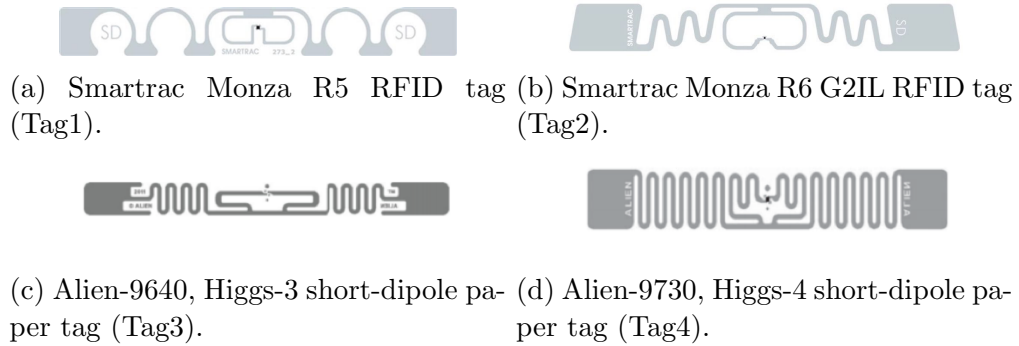
Figure 4.18: Rio is tested on four other tag types.

at medium speed over a single tag, as shown in Fig. 4.17a, is $3mm$. Given that the tag is $80mm$ in length, this median error is a mere 3.8% of the tag length. The median error with slow and fast swipes is greater, at 7 and $8mm$, respectively, but is still within 10% of the tag length.

This good single tag performance is not limited to our specific RFID tag. To demonstrate this fact, and we perform the medium-speed swipe gesture over four other types of tags with different antenna designs and RFID chips,

60
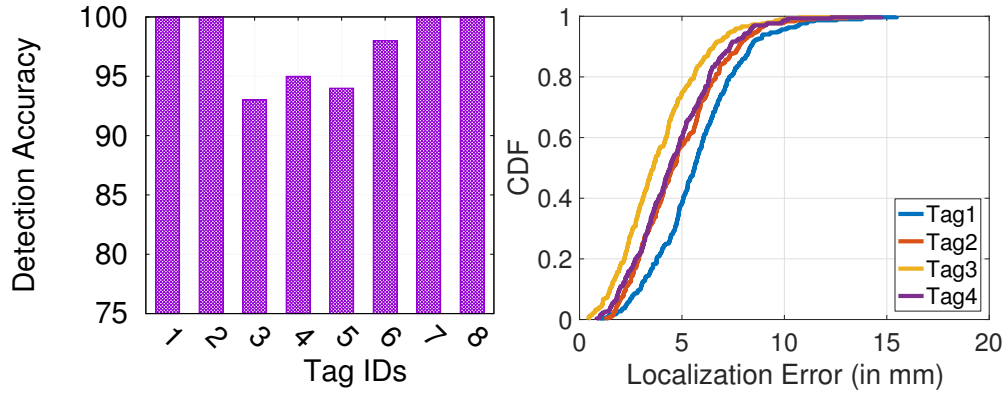
Figure 4.19: Touch detection on multi-tag array.

Figure 4.20: Swipe error distribution for 4 other tags(Tag1, Tag2, Tag3, Tag4).

as shown in Fig. 4.18. Fig. 4.20 shows that the median tracking error lies between 3 and $6mm$, less than 10% of the tag length.

COTS Multi-Tag Array. Fig. 4.17b shows the tracking error distribution in an array of eight (8) tags. These results assume perfect touch detection accuracy. Observe that the results show similar behavior to the single-tag case, where the medium speed swipe has this lowest median error of $7mm$, while the slow and fast speeds have median errors of 12 and $14mm$. Hence, even in the presence of mutual coupling effects, Rio can localize the finger to within 10% of the overall tag length. The experiments on both the single and multi-tag arrays demonstrate that Rio *can accurately track a finger's location during a swipe gesture.*

61
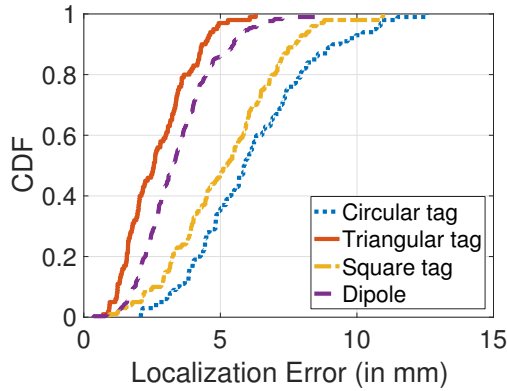
Figure 4.21: Tracking error distribution of custom tags.
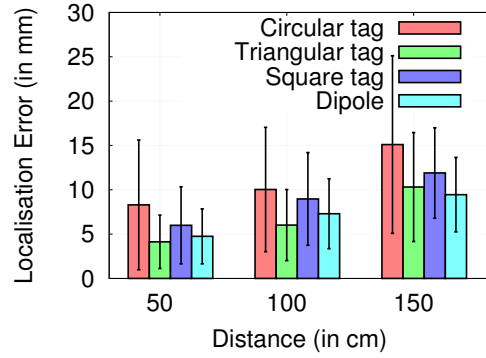
Figure 4.22: Tracking accuracy of custom tags at different distances from reader.
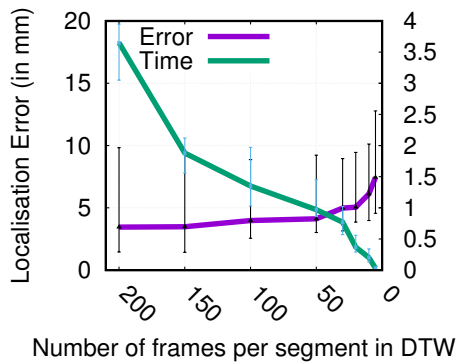
Figure 4.23: Tracking resolution vs computational overhead.
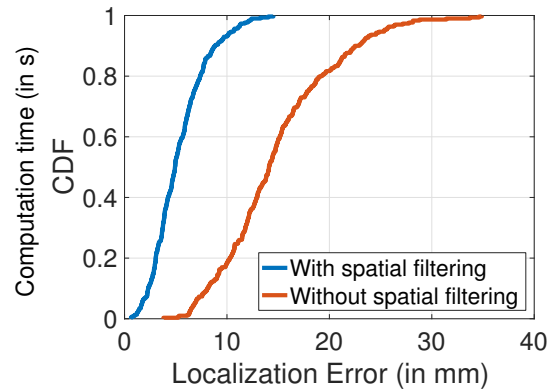
Figure 4.24: Swipe tracking accuracy over an array of 30 RFID tags.

4.5.2   RIO with Custom-Designed Tags

We evaluate RIO with four different types of custom tags: the circle and triangle, as shown earlier in Fig. 4.15, along with a square and dipole that are constructed with the same techniques. We place the smart tags $50cm$ away from the reader antenna and perform a medium-speed swipe gesture. Fig. 4.21 shows the tracking accuracy distribution when a swipe performed on each of these four custom tags. Observe that the median tracking error of all four tags is less than $8mm$, which is comparable to that obtained using COTS RFID tags. Fig. 4.22 shows the localization error distribution when the custom tags are placed at distances up to $1.5m$ away from the reader. Observe that even at this distance, the median tracking error is no more than $15mm$, or less than 19% of the tag length. Hence, RIO *readily supports custom-designed RFID tags that are purpose-built for specific smart spaces.*

4.5.3   RIO is a Robust Touch-Sensing Primitive
4.5.3.1   Tracking Resolution vs Computation Overhead

RIO trades off finger tracking resolution and computational overhead through the number of segments, M, used for each location update (procedure UPDATELOCATION in Algorithm 1) and Algorithm 3. For RIO, we run the data processing and pattern recognition module at an Intel desktop with a 2.93GHz Core i7 CPU and 16GB of memory, running Ubuntu 14.04 and JDK8.

Fig. 4.23 shows this trade-off for several values of M. Observe that M can be chosen to be as low as 50 with only a slight increase in median error

(from 3 to $4mm$) while achieving an almost $4\times$ reduction in computation time. At this chosen level of accuracy, RIO has a touch location tracking response time of one second. This computational overhead applies to both single and multi-tag setups. We note that these latencies relates to *motion tracking* only. A simple single-point touch-event can be detected within several milliseconds.

4.5.3.2 RIO on Large Multi-RFID Tag Arrays

We evaluate the performance of RIO-MULTI with 30 RFID tags, using the same experimental setup as that in §4.5. Fig 4.24 shows the tracking accuracy distribution of RIO with and without RFID spatial filtering. Observe that the median tracking error reduces from $14mm$ when no spatial filtering is used, to $6mm$ when filtering is enabled. Due to a large number of tags, when no filtering is used, there are time windows of T seconds when only a small number of phase data is obtained from the tag being touched. This results in reduced tracking accuracy. However, no such abnormalities are observed when PHY-layer tag filtering is used.

4.5.3.3 Robust Tracking under Varying Tag Tilt Angles

Fig. 4.25 shows the tracking accuracy of a medium speed swipe when the tags are placed at varying angles w.r.t. the plane of the RFID reader antenna. Observe that in both the single and multi-tag array, RIO can track the finger location with a tiny error (at 3 and $8mm$, respectively) when the tag is within 50°, of the reader antenna. This phenomenon happens because the

(a) Single tag.   (b) Multi-tag array.
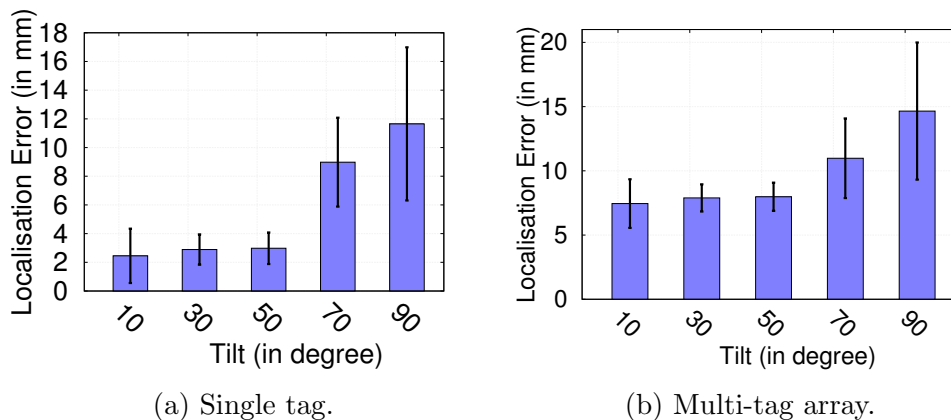
Figure 4.25: Tracking accuracy with varying tilt angle of the tag with respect to antenna.

RFID tags have linearly polarized directional antennas that focus the backscatter signals within a 120°, beam-width [28]. This result shows that *battery-free touch or gesture sensing is robust over a broad range of incident angles to the RFID reader.* As the tilt angle increases to greater than half the beam-width and the reader antenna moves outside the beam edge of the RFID tag, the tracking accuracy decreases. Note that changing the relative tilt angle of the tag is analogous to the change of the relative angle of the RFID antenna, and will thus yield similar accuracy results.

4.5.3.4   Robust Tracking at Varying Distances from Reader

Fig. 4.26 shows the tracking accuracy when a medium-speed swipe is performed on a tag that is at varying distances from the RFID reader. Observe that in the single tag case, a low error of no more than $8mm$ (10% error) is achievable up to $2m$ from the reader. This occurrence demonstrates that

(a) Single tag.   (b) Multi-tag array.
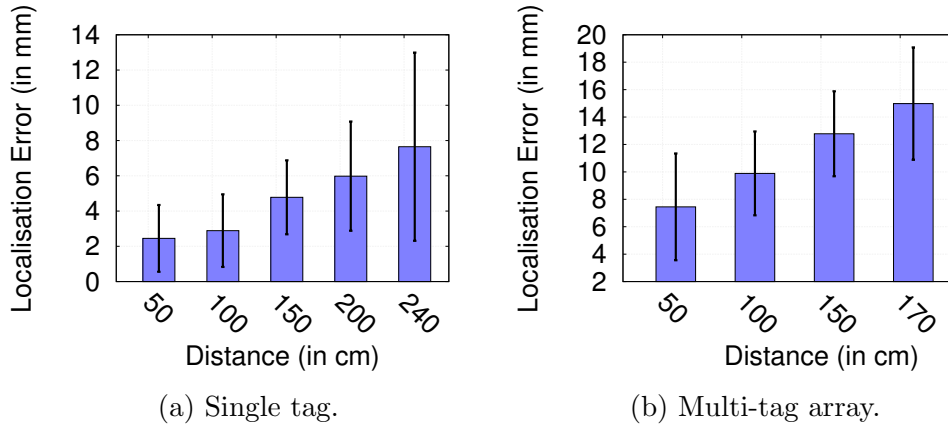
Figure 4.26: Tracking accuracy with varying distance of the tag from the reader antenna.

battery-free touch/swipe tracking is robust at varying distances from the reader. However, if we change multiple factors simultaneously (e.g., reading angle, tag tilt, blockage, etc.) or we change one of the impacting factors drastically (e.g., sudden increase of people in the room or introducing a new blockage between the tag and the antenna), we need to re-calibrate RIO to create the reference phase pattern to achieve mm-level accuracy.

4.5.4 Proof-of-Concept Applications

Rio is a touch sensing primitive for battery-free UI design. In this section, we describe and evaluate two proof-of-concept UI applications that are built using Rio.

Battery-Free Keyboard. A keyboard directly uses the touch-detection capability of RIO in a multi-tag environment. We use Rio to develop an 8-key musical keyboard (as shown in Fig. 4.27a), along with an accompanying

(a) Keyboard with 8 buttons.   (b) Numeric touchpad with digit "6" traced (shown rotated 90°).
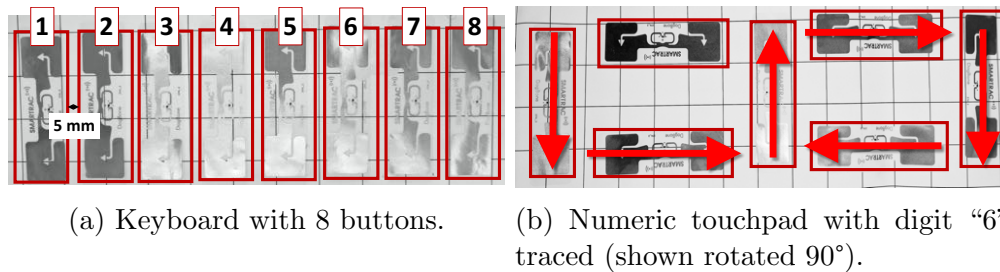
Figure 4.27: Example applications.

GUI. We can touch multiple keys simultaneously in this musical keyboard application. Fig. 4.28a shows the false positive (tag is mistakenly detected as being touched) and false negative (a touch event on a tag is missed). Observe that our simple threshold-based touch detection algorithm achieves high accuracy in this battery-free key detection system, with a total false positive and negative rates below 10%.

2D Numeric Touchpad. We have constructed a 2D numeric touchpad, as shown in Fig. 4.27b, using 7 COTS RFID tags. Each numeric digits is formed by tracing its shape over the RFID tags. Fig. 4.27b illustrates the outline of the number "6" (shown rotated 90°) traced on the touch-pad.

Fig. 4.28b shows the accuracy results when numbers 0 to 9 are drawn on this touch-pad. Each number is repeated 50 times, and the false positive and negative rates are reported here. Observe that all individual numbers can be detected with total errors of less than 15%. This shows that RIO with COTS tags can be used to design a general-purpose UI.

67
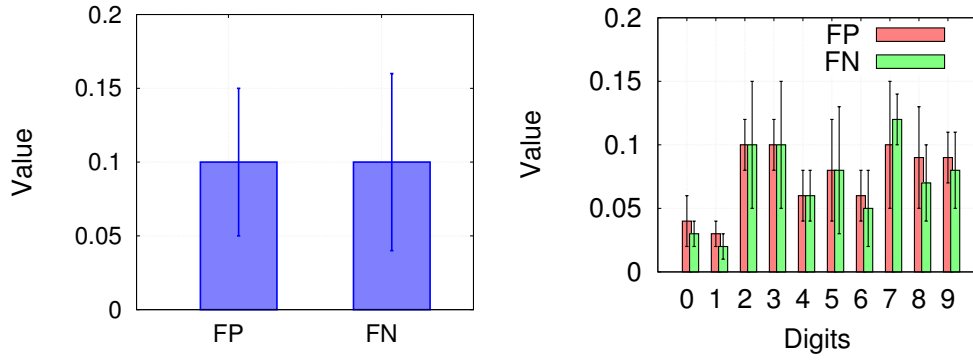
(a) Key press detection. (b) Numeric digit sensing.

Figure 4.28: False positive and negative rates for applications.

4.6 Points of Discussion

Naturally, there is much room for further work and possible improvements. We discuss a few points here.

Cost of Rio system: Rio can support multiple tags simultaneously for single-point touch tracking using a single antenna and single RFID reader. Currently, this combined unit with one antenna, one RFID reader, costs approximately $1600. We expect that dedicated RFID sensing platforms built upon lower-cost hardware (e.g., ThinkMagic reader hardware [36]), together with low-cost off-the-shelf tags will eventually be available to consumers.

Comparison with touch-based sensing: Capacitive touch screens [81] found in smartphones, tablets, laptops and the recently introduced PixelSense [27] offer a readily-available multi-touch interface. However, smart spaces demand low-cost, low-powered, flexible touch interfaces that can be readily integrated into existing off-the-self items. Current capacitive touch

screen technology cannot be easily and cost-effectively integrated into our envisioned smart spaces. We note that RIO offers a touch primitive to enable smart spaces and does not replace capacitive touch technology in all applications. Rather, we expect that RIO will integrate with and extend existing capacitive touch interfaces. For example, while RIO detects our direct interactions with the environment, these interactions can be managed through capacitive touch interfaces on our mobile devices.

Multi-touch tracking: RIO is basically a single touch-tracking system and in the near future, we plan to extend it to multi-touch tracking interface. This extension will broaden RIO's potential use-cases. However, for this, we have to model more complex mutual coupling phenomenon to provide accurate impedance tracking.

Impact of different blockage scenarios: Although we have shown in Fig. 4.5 that the phase pattern maintains its shape even in the presence of obstacles like door or wall, the experiments are not exhaustive for different static or dynamic blockage scenarios. In the near future, we plan to conduct more experiments in different types of blockage scenarios and different environment conditions to better understand the performance of RIO.

Chapter 5

TIMU: RFID based Motion Sensing

Sports analytics is a billion-dollar industry [47]. Many companies and startups are developing sports analytics for performance analysis, player fitness, safety, valuation, fan engagement, and broadcast management [48, 46, 49, 50]. An essential input to sports analytics is the sensed motion. For example, the rotation and translation movement speed and direction of a ball can predict the ball trajectory and game outcome. Therefore, it is critical for athletes, coaches, amateur players, and audiences.

Existing work: Recently there has been a surge of research interest in motion sensing. Many innovative sensing approaches have been proposed using a variety of wireless signals, including WiFi (*e.g.*, [162, 51, 173, 102, 195], acoustic (*e.g.*, [129, 142, 203, 207, 120, 204, 186]), RFID (*e.g.*, [185, 199, 183, 181, 179, 116]), 60 GHz (*e.g.*, [187, 109]), and THz (*e.g.*, [86]). Most of these works focus on estimating distance and angle of arrival to track translation movement.

Interestingly, rotation tracking is under-explored. On the other hand, rotation plays a significant role in sports analytics, especially involving balls (*e.g.*, tennis, basketball, ping-pong, racketball, baseball, cricket). Moreover,

existing device-free motion tracking systems, including WiFi, acoustic, and laser, do not work well for tracking ball movement due to the small cross-sectional area of the ball, limiting the amount of reflection and resulting in significant error.
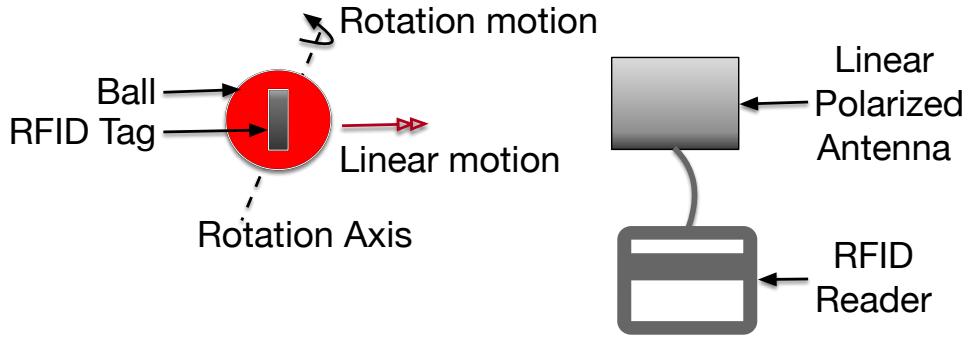
Figure 5.1: Architectural Overview of TIMU.

Gyroscope based approach is one way to sense rotational movement; however, gyroscope gets saturated within a few revolutions per second [41]. To improve accuracy, [88] combines gyroscope with magnetometer and UWB beacon with an antenna array to track a ball's rotation. However, it requires battery and significant modification to the ball [89]. Battery replacement is not only costly but also inconvenient. Moreover, the gyroscope, magnetometer, and UWB should be placed carefully inside a ball to track its rotation. This aspect significantly increases the manufacturing cost and the ball's weight, which may pose a problem to the players. Besides, it requires a way to communicate the sensed motion from the ball back to the analytics system. Long-range, high-resolution camera network is another option but suffers from occlusion

and high cost (\$100,000+) [88]. Moreover, it is not good at tracking fast rotation (*e.g.*, beyond 50 RPM) even with clear markers.

Tagyro [188] places multiple tags on an object and tracks the phase change from each tag to estimate the 3D orientation of a *static* object using two orthogonal RFID reader antennas. It models the phase change as a function of the distance change. COTS RFID uses below 1 GHz frequency (over 30 cm wavelength), limiting the accuracy of the phase-based tracking. Therefore [188] requires a static object with many widely separated tags (*e.g.*, 8.2 cm), multiple reader antennas, and extensive calibration, which is not suitable for sports analytics.

Motivated by the existing works and their limitations, we seek to develop a motion-sensing system using a commercial-off-the-shelf (COTS) reader, antenna, and RFID tags. We attach RFID tags to a ball and use a commercial-off-the-shelf (COTS) reader with a single antenna to sense both rotation and translation movement, as shown in Figure 5.1. We build an end-to-end system to integrate both rotation and translation tracking to handle general movement involving both rotation and translation. We build a system, called TIMU (Tag Inertial Measurement Unit), which turns COTS RFID Tags into battery-free IMUs. It measures motion parameters, including rotation axis, rotation speed, 3D position in a battery-free manner, while eliminating the need for an additional communication channel to report the tracked information.

We can use TIMU in different ball games, as shown in Fig. 5.2. For example, in cricket or baseball, we can put the RFID antenna behind the

batsman or the striker and attach the tags to the ball. In bowling or basketball, we can put the antenna behind the pins or hoop for motion tracking.

(a) Cricket.

(b) Basketball.

(c) Baseball.

(d) Bowling.
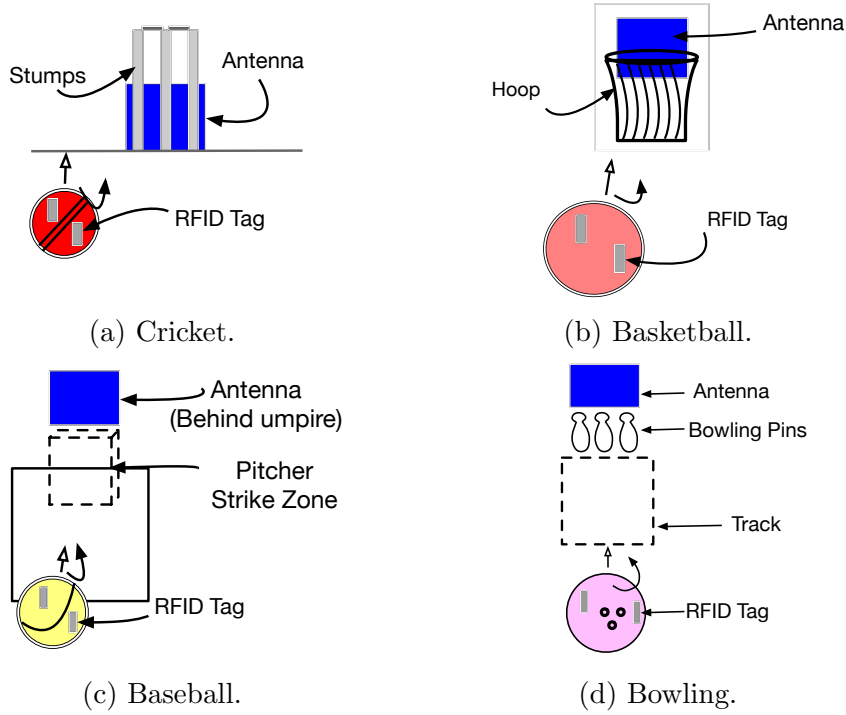
Figure 5.2: Possible sports applications of TIMU.

Our contribution can be summarized as follow:

- We develop a systematic model that captures the impact of polarization between an RFID tag and a reader antenna on the phase and magnitude of the received signal. It captures non-uniform gain between the RFID tags and reader antenna.

- We design a novel algorithm that uses the polarization to estimate the rotation axis and speed using a *single* RFID reader antenna. We extend

our algorithm to estimate further AoA and distance using a *single* RFID reader antenna. To the best of our knowledge, this is the *first* system that senses general motion, including both rotation and translation using a single RFID reader antenna.

- We implement and evaluate our approach and demonstrate its feasibility in various scenarios, including environments with static or dynamic multipath.

5.1 Analytical Model for TIMU

In this section, we describe an analytical model that captures the impact of the relative orientation of the RFID reader and tag on the received signal due to polarization and other factors. We borrow from several literatures to provide a comprehensive framework to understand the impact of motion on the RFID phase and received signal strength (RSS).

5.1.1 Model of Received Signal Phase

We first examine how the movement affects the phase of the received signal. Consider the RFID setup in Figure 5.3. Let r denote the distance between the reader antenna and tag. Therefore, the signal traverses a total distance of $2r$ due to back-scattering. The received phase is not only determined by the distance, but also by the additional phase offsets introduced by the transmitter, tag, and receiver circuits, denoted as θ_T, θ_{TAG} and θ_R, respectively. The total phase change [35] observed by the reader can be expressed

as:
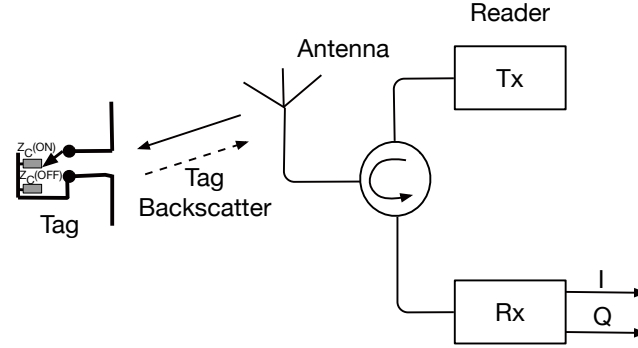
Figure 5.3: RFID Reader/Tag Communication Diagram.

$$\theta \; = \; (\; \frac{2\pi}{\lambda} \times 2r \; + \; \theta_T \; + \; \theta_{TAG} \; + \; \theta_R \;) \; mod \; 2\pi \qquad (5.1.1)$$

where λ is the wavelength. $\theta_T + \theta_R$ can be expressed as polarization mismatch $2\phi(\hat{r})$ or 2γ.

5.1.2   Received Signal Strength

When both the reader antenna and the tag antenna are linearly polarized, the polarization loss factor (ρ) can be expressed as $\rho = cos^2(\gamma)$, where γ is the polarization mismatch between the two antennas. Therefore, for a linearly polarized reader antenna and linearly polarized passive tag antenna pair, Equation (2.6.2) becomes as follow:

$$P_{tag} = (\frac{P_t G_t(\theta_t, \phi_t)}{4\pi r^2})(\frac{G_{tag}(\hat{\theta}_t, \hat{\phi}_t)cos^2(\gamma)\lambda^2}{4\pi}) \qquad (5.1.2)$$

75

Let P_{tag} denote the power impinged upon tag and P_{chip} denote the amount of harvested power that is transferred to the RFID chip (IC). It can be expressed as follow [62, 93]:

$$P_{chip} = KP_{tag} \tag{5.1.3}$$

where K is the modulation loss of the tag antenna (the value is less than 1) and depends on the impedance matching between the chip and tag antenna.

Using the free-space Friis' equation model in the reverse side, we get the received power (P_{rec}) as follows (similar to Eq. (5.1.2)):

$$P_{rec} = \left(\frac{P_{chip}G_{tag}(\hat{\theta}_t, \hat{\phi}_t)}{4\pi r^2}\right)\left(\frac{G_t(\theta_t, \phi_t)cos^2(\gamma)\lambda^2}{4\pi}\right) \tag{5.1.4}$$

which becomes Eq. (5.1.5) by substituting P_{chip} in Eq. (5.1.4) by using Eq. (5.1.2) and Eq. (5.1.3) :

$$P_{rec} = P_t G_t(\theta_t, \phi_t)^2 G_{tag}(\hat{\theta}_t, \hat{\phi}_t)^2 K cos^4(\gamma)\left(\frac{\lambda}{4\pi r}\right)^4 \tag{5.1.5}$$

This indicates that

$$P_{rec} \propto P_t G_t^2 G_{tag}^2 r^{-4} K cos^4(\gamma)\frac{1}{r^4} \tag{5.1.6}$$

To use our model, we need the gain values of the RFID tag and reader antennas. For each position, we derive the gain values of the tag and reader antennas based on their relative geometric positions according to their corresponding datasheets. Fig. 5.4 shows their gain patterns, where the tag's gain pattern follows a cylindrical shape, and the reader antenna's gain pattern has a main lobe with two side lobes.
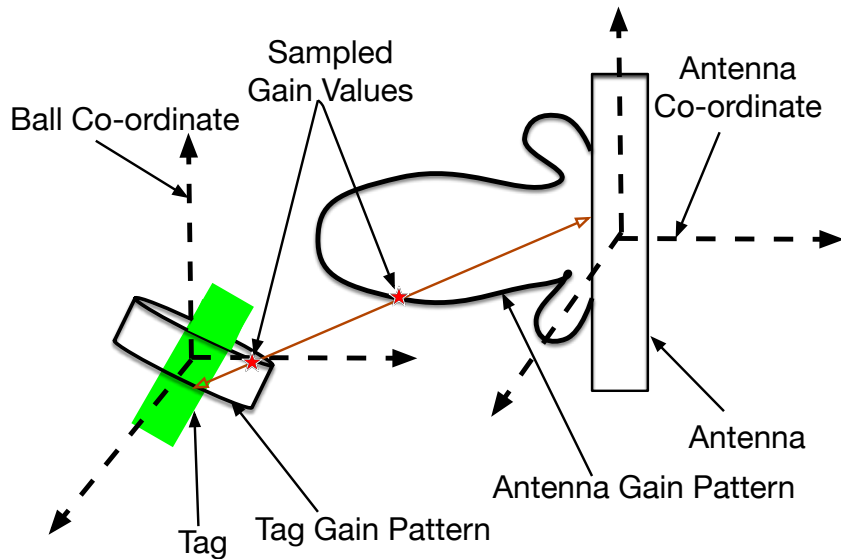
Figure 5.4: Explanation of gain value sampling.

5.1.3 Model Validation

Measured vs. modeled phase and RSS: We compare the model with the measurement from our RFID setup. Fig. 5.5 show the measured and modeled phase during a rotation when the ball is rotating around the following four different rotation axes: (0,0,30), (45, 0, 20), (0, 60, 60), and (45, 60, 5). Figure 5.6 compares the measured and modeled RSS under the same rotation axes. We make the following observations. First, different rotation axes tend to have different phases and RSS patterns. This phenomenon suggests that it is potentially feasible to use the phase and RSS patterns to estimate how the ball rotates. Second, our modeled phase and RSS closely follow the measurement. Therefore it is promising to use the modeled patterns to estimate the rotation axis.
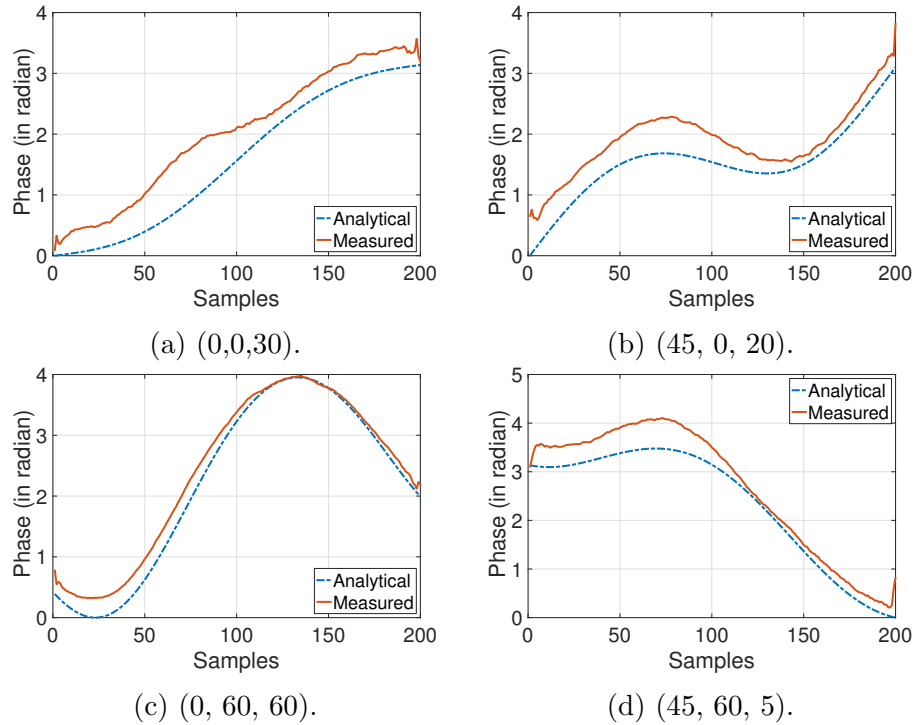
Figure 5.5: Validation of Phase with different Rotation Axis Configurations (Yaw, Pitch, Roll).

Modeling error: We further quantify the accuracy of our model by collecting received signals over 200 different rotation axes at a 0.5m distance. We rotate the balls at least 5 times and automatically detect the start and end of the rotation. We align the measurement samples across different rotations using correlation and compute the median across all rotations for each sample. We compute the difference between the samples from our measurement with those from our model and compute the average per template pair. Fig. 5.7(a) and (b) show the CDF of the modeling error for the phase and RSS, respectively. As we can see, the median phase error is around 0.1 radian, and the median

(a) (0,0,30).

(b) (45, 0, 20).

(c) (0, 60, 60).

(d) (45, 60, 5).
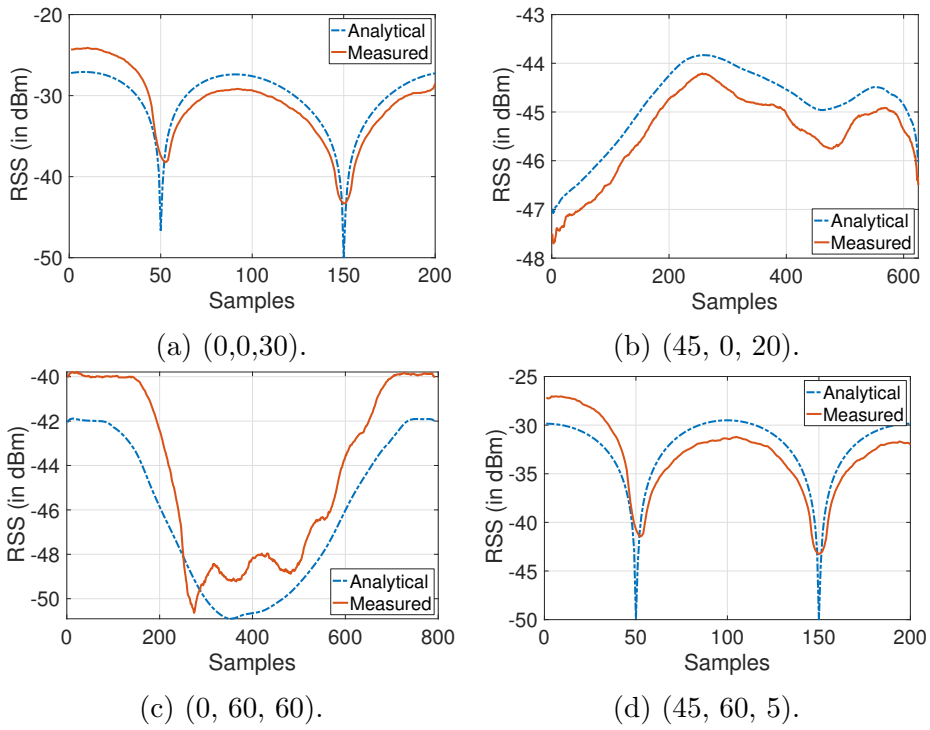
Figure 5.6: Validation of RSS with different Rotation Axis Configurations (Yaw, Pitch, Roll).

RSS error is around 3 dBm.

(a) Phase Modeling Error

(b) RSS Modeling Error
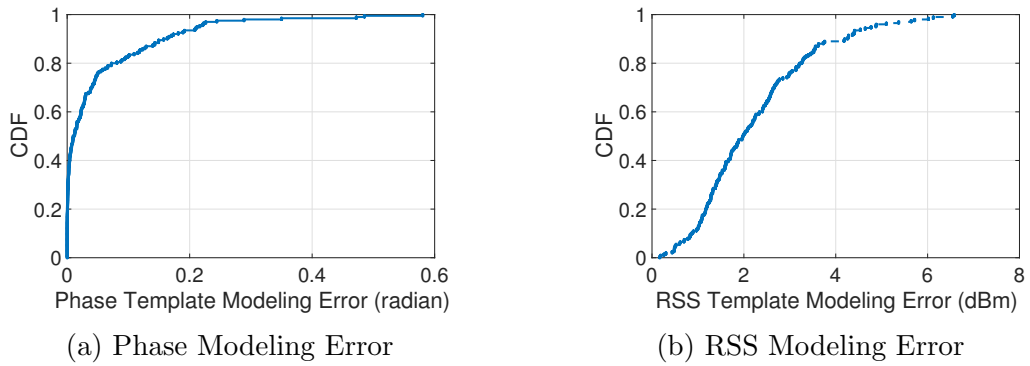
Figure 5.7: CDF of Modeling Error across 200 traces.

Impact of multipath : We further evaluate the impact of multipath by collecting additional measurements in two ways: one without intentionally adding multipath and one with intentionally adding multipath by placing 5 wooden reflectors ($1m \times 1m$ large and $1cm$ thick) wrapped with aluminum foil near As we can see, the modeled RSS and phase match well with the measurement. The match is close even under the multipath scenarios because linearly polarized tag and reader antenna significantly weaken the signals coming in other directions and limit multipath.

Furthermore, we create dynamic multipath situations: (i) by moving a wooden barrier (1 m × 1m large, 5 cm thick) around intermittently blocking the direct path between the tag and antenna, and (ii) by moving the wood around without blocking the direct path between the tag and the antenna. Fig. 5.8(c) and Fig. 5.8(d) shows that although there is distortion in the pattern in the blocking scenario, the overall shapes remain similar.

5.2   Tracking Algorithm

To track a ball, we attach multiple RFID tags to the ball. We develop a tracking algorithm to estimate its translation and rotation movement incrementally. First, we consider the ball's position is fixed and known, and design an algorithm to estimate its rotation axis and speed. Then we relax the assumption and estimate the ball's position in addition to its rotation axis and speed.

We use the setup shown in Fig. 5.9. We calculate the rotation axis

(a) Phase under static multipath.   (b) RSS under static multipath.

(c) Phase under dynamic multipath.   (d) RSS under dynamic multipath.
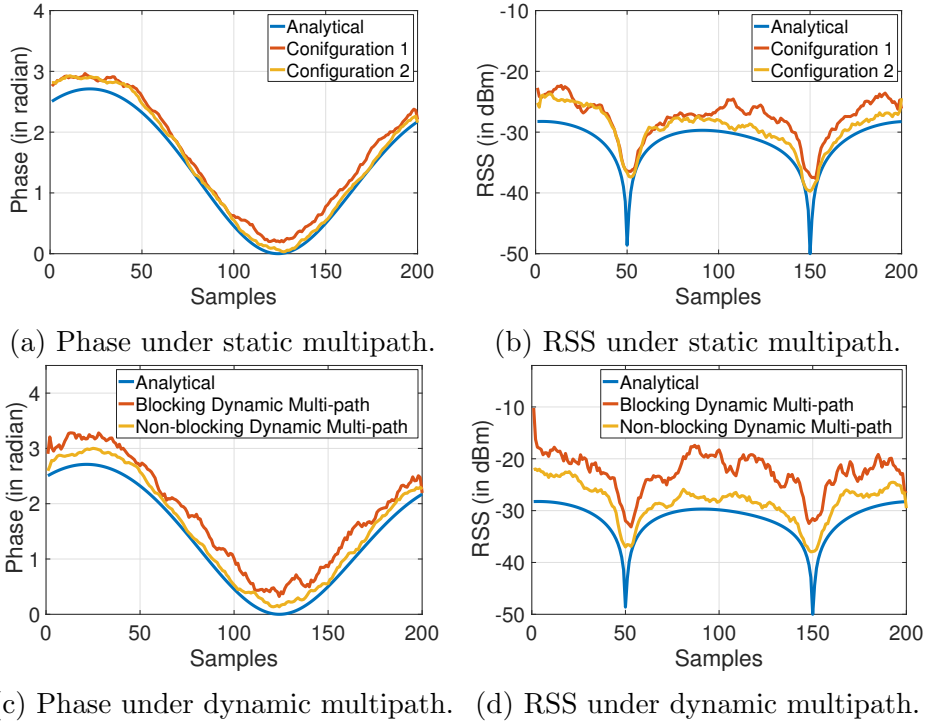
Figure 5.8: Measured vs. modeled phase and RSS under static and dynamic multipath when the ball rotates along the axis (70,30,15).

angles with respect to the ball's coordinate system. We set the center of the RFID antenna as the origin. We transform the ball coordinate using proper rotation matrix multiplication and translation transformation. The azimuth defines the horizontal angle between the ball and reader antenna, and the elevation defines the vertical angle between the ball and reader antenna. We choose linear polarized reader and tag antennas (*i.e.*, the electric magnetic field is confined to a plane as shown in Fig. 5.9) since it results in deterministic and distinguishable phase and RSS patterns during rotation. Furthermore, as shown in Fig. 5.9, we place multiple tags with different orientations with
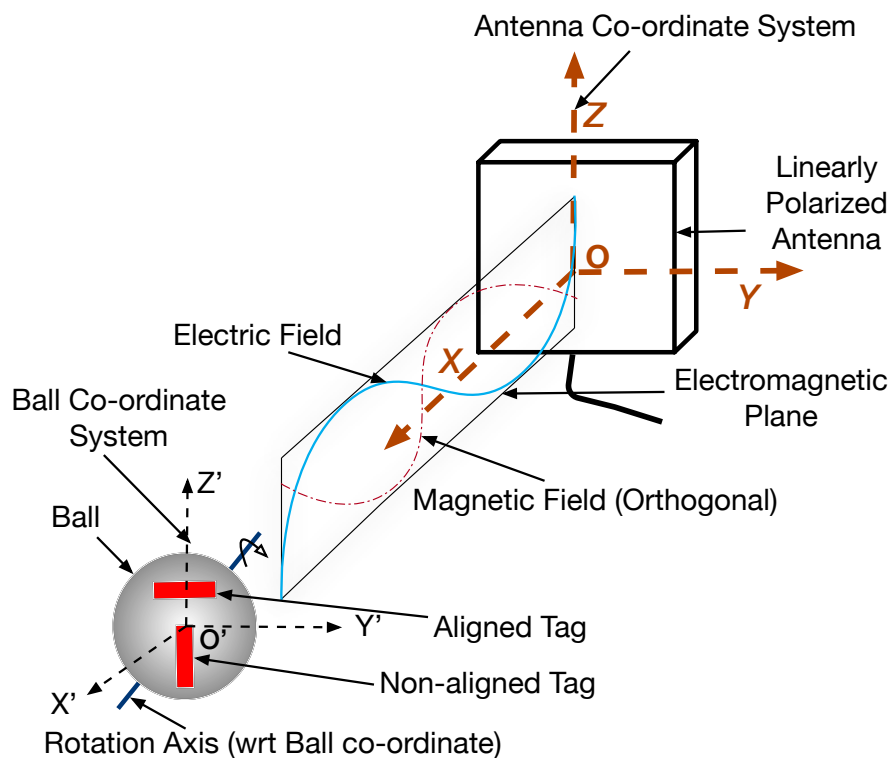
Figure 5.9: Polarization and co-ordinate Systems of TIMU.

respect to the polarization plane of the RFID reader antenna to maximize diversity and improve accuracy. We avoid 90 degree angles between the tag orientation and reader antenna's polarization plane since it would result in the minimum received signal.

5.2.1 Estimate Rotation Axis and Speed

In this section, we assume the ball's position is fixed and known, and estimate the rotation axis, speed, and direction.

5.2.1.1   Estimate Rotation Axis

First, we consider how to estimate the rotation axis. We observe different rotation axes result in different RSS and phase patterns during a rotation. Therefore we can use the RSS and phase measurements from a rotation to infer the rotation axis. In particular, we leverage the model in Section 5.1 to facilitate our estimation.

Problem formulation: Our goal is to search for the rotation axis $(\theta_1, \theta_2, \theta_3)$ such that the resulting received signals best matches the measured signals. We can detect the start and end of a rotation based on the periodic RSS pattern, as described in Sec. 5.2.1.2. Let r_k^i denote the i-th measured received signal from tag k during one rotation, N denote the total number of samples we get from each tag in one rotation, and M denote the total number of tags.

Given the ball size, position, rotation axis, and the number of samples per rotation, we can derive the tag trajectory during a rotation based on geometry. We uniformly sample the trajectory so that we generate the same number of samples like the one from the measurement. For each position on the trajectory, we compute its phase and RSS as described in Section 5.1 to get a complex signal. Let $m_k^i(\theta_1, \theta_2, \theta_3)$ denote the i-th received complex signal from tag k during the rotation estimated using our model when the rotation axis is $(\theta_1, \theta_2, \theta_3)$.

Our goal is to search for the rotation axis that minimizes the fitting

error with the measured signals across all tags. That is:

$$min_{\theta_1,\theta_2,\theta_3} \sum_k |m_k^i(\theta_1,\theta_2,\theta_3) - r_k^i| \qquad (5.2.1)$$

Signal alignment: This formulation assumes the modeled and measured signals are correctly synchronized. This synchronization is achieved by computing the correlation between the two signals at all offsets and finding the offset that yields a peak in the correlation.

Algorithm: The problem is challenging to solve since the objective is non-linear and has many local optimal. One option is to perform a binary search or a hierarchical search. However, it does not work well since a local optimal may be surrounded by points that are far from optimal. Another option is to generate profiles for all possible rotation axes at a given granularity using our model and exhaustively compare the measurement against all profiles from our model. This operation is expensive. If we resort to a coarse search resolution to speed up the search, the accuracy will degrade. Instead, we use non-linear optimization (*e.g.*, fmincons() in MatLab). We find the optimization results are sensitive to the initialization. In order to get a good solution, we need an initial solution that is not too far away from the optimal. This phenomenon is not surprising since when the search space is large, random initialization is not effective. Therefore, a good initial solution is important not only for speed but also for the high quality of the solution.

To improve the speed and quality of the search, we develop two strategies. First, we use a machine-learning algorithm to find an initial solution. We
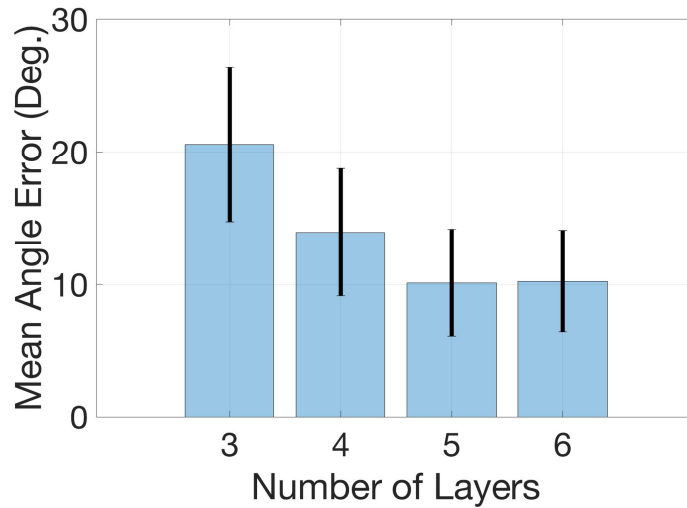
Figure 5.10: Empirical Parameter Selection of a fully-connected DNN for initialization.

use a deep neural network (DNN) as the machine learning algorithm. The advantage of using a DNN is that it can approximate any function with arbitrary accuracy. We use a fully connected 4-layer DNN, which has 600, 500, 400, and 300 neurons at the first, second, third, and fourth layers, respectively. The DNN maps the phase and RSS samples during one rotation to the 3D rotation axis. Following the common practice, we normalize the inputs using 'ReLu' transfer function for hidden layers and end with a single unit and a 'sigmoid' activation. The neural network is trained using Adam optimizer, the learning rate of 0.0000001, and the maximum iterations of 100000. We generate the training data using a combination of measurement data and synthetic data derived from our model. Our results show that the initial solution derived from the DNN significantly improves the solution quality and search speed. Before arriving at this specific architecture, we have empirically evaluated with

other configurations. Fig. 5.10 shows the average error reduces initially as we increase the number of layers from 3 to 5, and then tapers off as we further increase the number of layers.

Moreover, we observe that searching a rotation axis for each rotation independently is sub-optimal since it ignores the strong temporal correlation between consecutive rotations. To take into account the temporal locality, for each rotation, we generate multiple initial solutions by injecting a small random noise to the output from DNNs and feed each of the perturbed solutions to $fmincons$ in Matlab. In this way, we obtain L candidate solutions for each rotation. We select the candidate solution from each rotation to minimize the total difference between the consecutive rotation axes to capture the temporal locality. To achieve this goal, we construct a graph with $L \times R$ nodes (L nodes per rotation and R rotations). We fully connect the nodes in rotation i with those in rotation $i + 1$ with edge weights representing the Euclidean distance between their corresponding rotation axes. We find the shortest path in the graph. The solutions corresponding to the nodes on the shortest path are the final rotation axes. Our evaluation shows that $L = 5$ and $R = 3$ give the right balance between the computation cost and accuracy.

Figure 5.11 shows the CDF of estimation errors using random initialization, DNN, and DNN with the temporal locality. As we can see, the median error decreases from 32.5 degrees in random initialization to 9 degrees in DNN and 5 degrees in DNN with the temporal locality. Furthermore, to observe the dependence of data collection setup in our DNN initialization, we collected

86
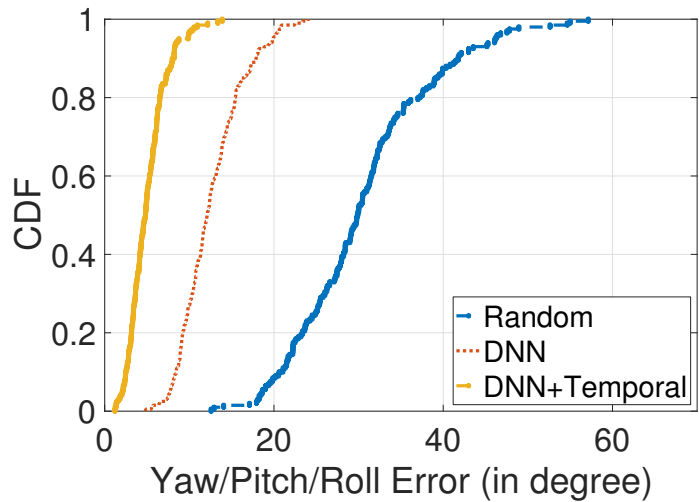
Figure 5.11: CDF of Error using different initialization.

rotation axes data in two different locations while using one for training and others for estimating and vice versa. If we use data from the same location compared to different locations in training and estimating for our DNN initialization, the median error for angular estimation goes from 5.5 degree to 7.5 degree. The error is not significant because the pattern templates remain similar for a particular rotation axis due to the polarization property.

Multiple tags: This optimization can support multiple tags by summing up the fitting error across all tags. This aspect helps to avoid the zones that have similar rotation templates and thus yielding more error. To balance the computation cost and accuracy, we use 3 tags. Fig. 5.13 shows that using three tags can reduce the median estimation error of the rotation axis from 15 degree to 5 degree.

We use a Macbook Pro running OS Sierra with a 8GB RAM and i5
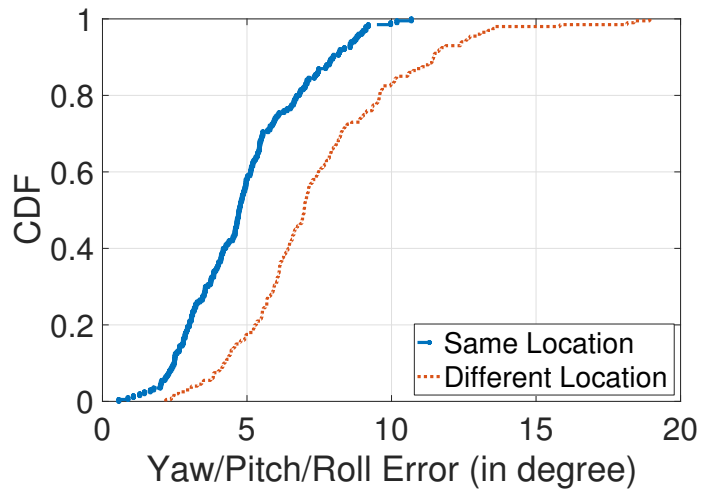
Figure 5.12: CDF of Error using training and testing in data collected from two different locations.
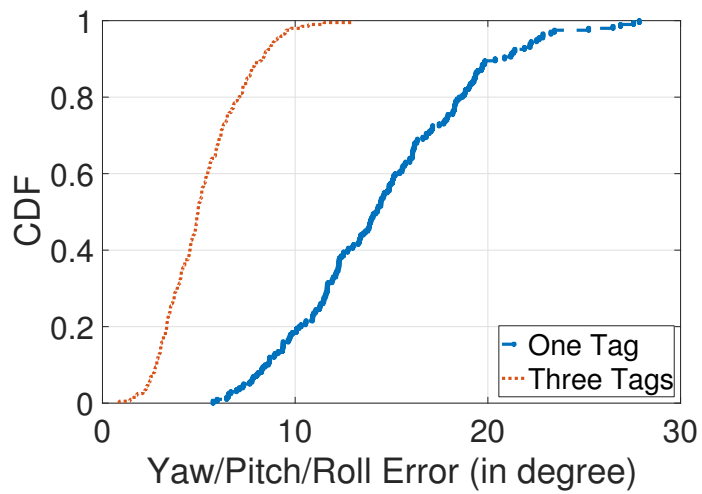
Figure 5.13: CDF of rotation axis error using 1 or 3 tags.

quad-core processor to process the data. It takes around 0.5 second to run the DNN based initialization and, on an average, 1.5 seconds to estimate the parameters of rotation with other related values.

5.2.1.2   Estimate Rotation Speed

As shown in Figure 5.14, the received signal strength (RSS) exhibits a periodic pattern as the ball is rotating. The RSS reaches a peak when the tag is parallel to the reader antenna (*e.g.*, their angles are at 0°, 180°, 360°, and so on). The RSS reaches a valley when the tag and reader antenna are perpendicular to each other. Therefore, by counting the number of peaks, we can estimate the number of rotations per minute (RPM).
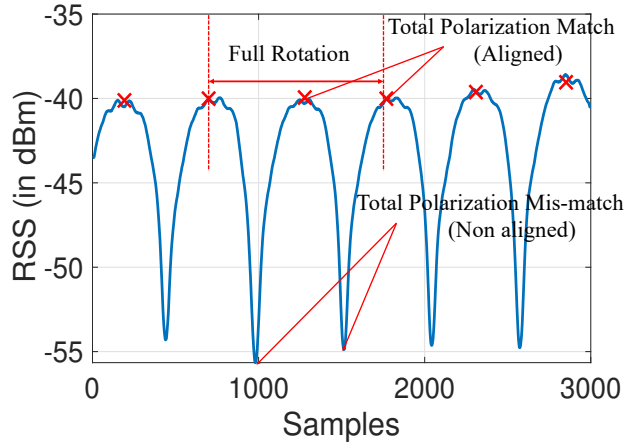
Figure 5.14: Example of RSS during two complete rotations at a 0.5m distance.

5.2.1.3   Estimate Rotation Direction

Rotation can happen clock-wise or counter-clockwise. For a given ball rotation axis and position, these opposite rotations produce reverse templates as shown in Fig. 5.15. Therefore, by analyzing the template pattern, we can infer the rotation direction.

89
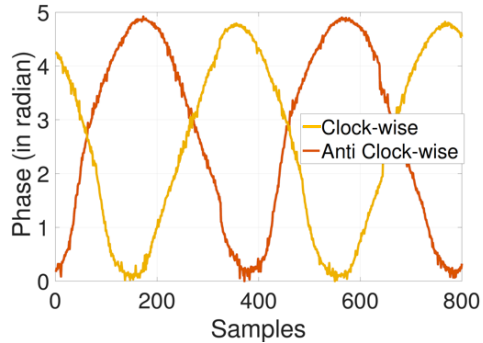
Figure 5.15: Rotation Clock-wise or Reverse Clock-wise.

5.2.2 Estimate Ball Position Using a Single Antenna

In this section, we focus on estimating the ball position using a single antenna (*i.e.*, the angle of arrival (AoA) and the distance from the ball). Our AoA estimation requires the ball to rotate, whereas the distance tracking assumes the translation movement dominates the phase change. We will further integrate rotation and translation tracking in Section 5.2.3.

5.2.2.1 Estimate AoA

Our algorithm: Existing approaches use an antenna array to estimate the angle of arrival (AoA). We explore the feasibility of using a single RFID reader antenna to estimate the AoA by exploiting the polarization and non-uniform gains of the reader antenna and tag. We observe that AoA affects the phase and RSS pattern during one rotation; therefore, it may be possible to use the phase and RSS measurements in a rotation to infer the AoA along with the rotation axis. We apply the same optimization framework in Section 5.2.1 ex-

cept that we now add two new unknowns: azimuth and elevation. To improve the search for the rotation axis and AoA, we use another DNN with the same structure as in Section 5.2.1 except that it has a 5-dimension output vector, which includes the rotation axis, azimuth, and elevation. As before, we find DNN based initialization works much better than random initialization since it uses the RSS and phase patterns to determine a good starting point.

Addressing symmetric issue: Another issue remains: the impact of AoA on the phase and RSS is symmetric. For example, the AoA of 30 degrees to the left has the same effect on the RSS and phase as 30 degrees to the right. To disambiguate the left versus right, we use the scheme as illustrated in Fig. 5.16, where we attach two tags in parallel to the ball. As shown in Fig. 5.16, the outer tag has a larger distance and smaller azimuth when the ball is on the right side and vice versa when the ball is on the left side. We estimate the absolute distance of the tags using our two-frequency based method as described in Section 5.2.2. We apply the above rule to determine whether the ball is on the left or right side to the reader antenna. Our evaluation does not distinguish the elevation since we assume the target has a positive elevation angle. However, in principle, we can apply a similar approach to distinguish whether the tag is above or below the reader antenna.

5.2.2.2   Estimate Distance

We use the phase of the received signal to estimate the distance based on Equation 2.4. According to the previous phase model, $\theta = \frac{2\pi}{\lambda} \times 2r +$
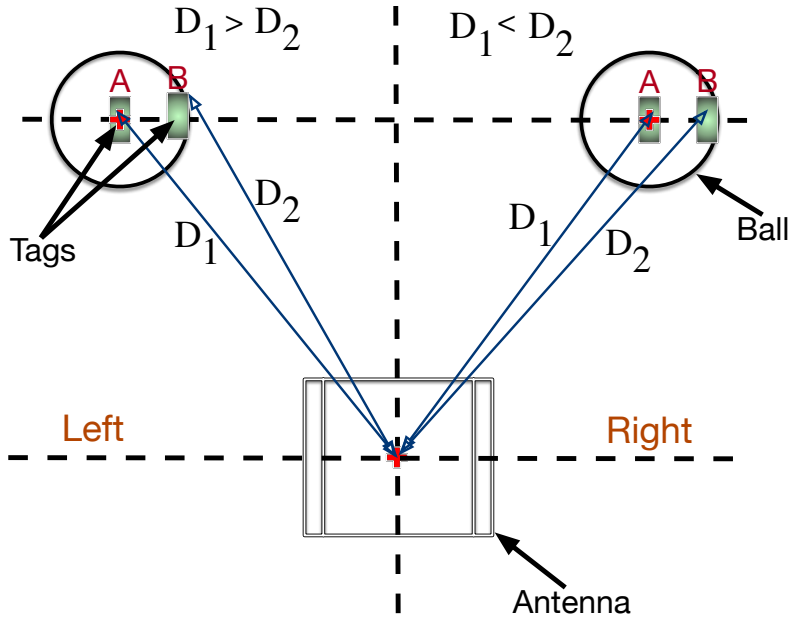
Figure 5.16: Distinguishing between the left and right.

$2\gamma + C$. So we estimate the change in the distance r based on the change in the phase θ. However, due to the phase wrap-around, it only gives the relative distance change. In order to estimate the absolute distance, we use multiple frequencies since they significantly increase the wrap-around period due to Chinese Remainder Theorem [189], which states that solution is unique modulo to Least Common Multiple (LCM) of $\lambda_1, \lambda_2, ..., \lambda_n$ (which is much larger than a single frequency), where n is the number of frequencies. We use two frequencies: 865.7MHz and 867.5MHz, which yields a wraparound period of around 250 ns. This value corresponds to around 75 m one way, which is large enough to avoid ambiguity in our context. There is a random phase offset at the reader antenna. To remove the random offset, following [147],

we attach an auxiliary tag to the RFID antenna and compute the difference between the phase obtained from the target tag and auxiliary tag. We use the phase difference between the two for distance estimation.

In practice, the commercial RFID reader can only transmit on one frequency at a time. So it performs frequency hopping and uses the two closest samples collected from the two frequencies to derive the absolute distance. The only difference is that we should compensate for the phase change arising from the samples collected at different times. Since we can easily derive the phase change between the previous two samples, we can use it to compensate for the phase change due to different sampling times.

5.2.3   Supporting Simultaneous Rotation and Translation

Next, we study how to estimate both rotation and translation movement at the same time. Fig. 5.17 shows an example phase pattern when a ball has both translation and rotation movement. We observe that the total phase change is the sum of the phase change due to rotation and due to translation movement. Therefore, to estimate the rotation axis, we should remove the impact of the translation movement on the phase change.

Based on the above observation, we integrate our rotation estimation in Section 5.2.1 with our translation motion estimation in Section 5.2.2 to support both translation and rotation movement. Algorithm 4 shows the pseudo-code. Steps 1, 2, 5, and 6 are described in Section 5.2.1 and Steps 3 and 7 are described in Section 5.2.2. In step 4, we compensate the phase change from
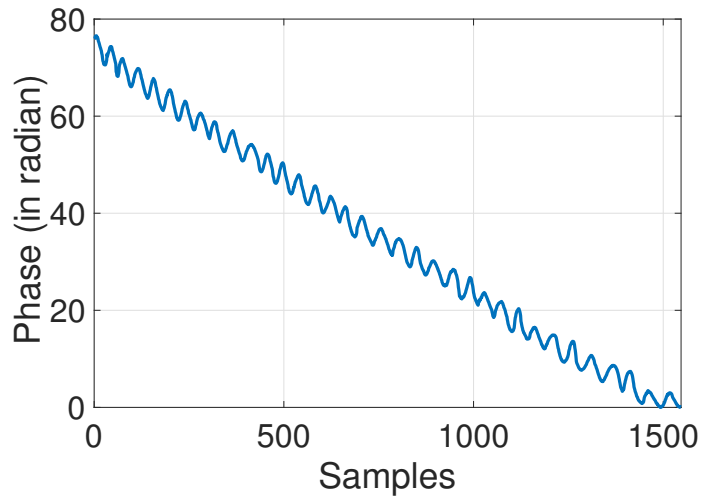
Figure 5.17: Example Phase Pattern of a Highly Rotating Moving Ball with Slow Linear Speed.

the translation movement by adjusting the phase of the i-th sample during a rotation by the $-\Delta\theta \times i/N$, where N is the number of samples in a rotation and $\Delta\theta$ is the phase change during one rotation, which is caused only by the translation movement since a complete rotation at a fixed position should not change the phase. This assumes constant translation movement during a rotation, which is likely to hold in practice since velocity tends to remain the same during a small time interval.

5.3   Evaluation

In this section, we first describe our evaluation setup and then present the evaluation results.

Algorithm 4 Final algorithm

1: Estimate the rotation speed based on RSS (Section 5.2.1.2)
2: Estimate the start and end time of each rotation as the consecutive RSS peaks (Section 5.2.1.2)
3: Estimate the distance change and direction during each rotation based on the phase change of the received signal (Section 5.2.2.2)
4: Compensate the phase change caused by the translation movement
5: Use the phase and RSS time series from each rotation after compensation to estimate the rotation axis, direction and AoA for the rotation (Section 5.2.1.1)
6: Estimate rotation direction (Section 5.2.1.3)
7: Estimate AoA (Section 5.2.2.1)
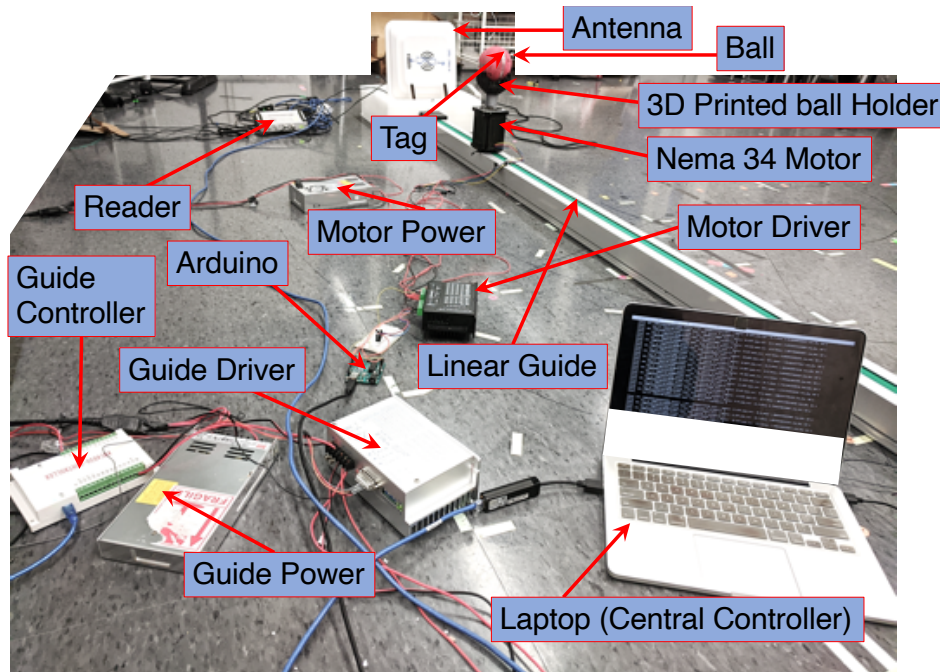
Figure 5.18: Experimental Setup of TIMU.

5.3.1 Evaluation Setup

To perform controlled movement experiments and quantify the accuracy of our tracking algorithm, we build a setup that allows us to control the

rotation axis, rotation speed, translation speed, and direction, as shown in Figure 5.18. To collect the ground truth, we use a moving track [42] whose movement can be programmed and controlled via a laptop using USB. The track is 2.5m long and supports a moving speed from 1cm/s to 3m/s. To drive the motion guide, we use an AMC430 controller [44], a motor driver, and a dedicated power source. Furthermore, to support different rotational axis configurations, we 3D print a Goniometer [40], as shown in Fig. 5.19. We place an RFID tag on the ball placed above the Goniometer, as shown in Fig. 5.20. To create rotational motion, we use Nema 34 motor [45] with a motor driver and power source [37]. This rotation motion is controlled by arduino [39], which in turn connected to the laptop. We vary the translation movement from 1cm/s to 3m/s and rotation speed from 1rpm to 400rpm. Unless otherwise specified, we use a 6cm radius rubber ball in our experiments, as shown in Fig. 5.20. The default translation speed, rotation speed, azimuth, elevation, Yaw, Pitch, and Roll values are 10 cm/s, 60 RPM, 20 degrees, 20 degrees, 0 degree, 0 degree, and 45 degree respectively. We further vary each of these parameters to understand its impact.

We use a commodity Impinj RFID reader R420 [25] (which is ETSI-compliant). It can support frequencies from 865.7MHz to 867.5MHz. We use a 9dBi linearly polarized (RHCP) RFID antenna to leverage its polarization for motion tracking [43], and it is connected to one of the RF port of the reader. The antenna hops between these two frequencies for absolute distance estimation. We use the highest allowable transmission power setting of 32.5dBm.

We use Alien Squiggle RFID clear wet inlay (ALN-9740) tags [38], which are tuned to work in 840 MHz to 960 Mhz (Global) for our experimental purposes. We can read these tags with our linearly polarized antenna from up to 10m in line-of-sight setting and up to 6m in a non-line-of-sight setting. We can achieve a sampling rate of around 200Hz for a single tag and around 50 Hz for three tags in our setup. For 3 tags, we put two tags in parallel 90 degree apart and another tag on the other side in an orthogonal orientation to this tag-pair. The reader interrogates tags using a Low-level Reader Protocol (LLRP) approved by EPCGlobal. It sends query reports containing information of ID, RSS, Phase, time-stamp, and channel, via Ethernet to a host laptop. We implement TIMU using RFID library and processing algorithms implemented in python and MATLAB. In all the following experiments, unless otherwise specified, we report the performance of 5 runs for each configuration using errorbars or CDFs. The center of the error-bar is the median, and its two ends correspond to 25-percentile and 75-percentile. We perform all of the experiments in a typical lab with several furniture (*e.g.*, tables, chairs, desks, shelves) and desktops nearby. To reduce noise in the data, we follow [188] to post-process the phase and RSS measurements by computing the median over a sliding window of 20 samples.

5.3.2   Evaluation Results

We evaluate each component of our motion tracking algorithm. We change one dimension at a time to quantify the tracking accuracy of the ro-

(a) 3D Printed Goniometer.   (b) Rotation Axis Change.
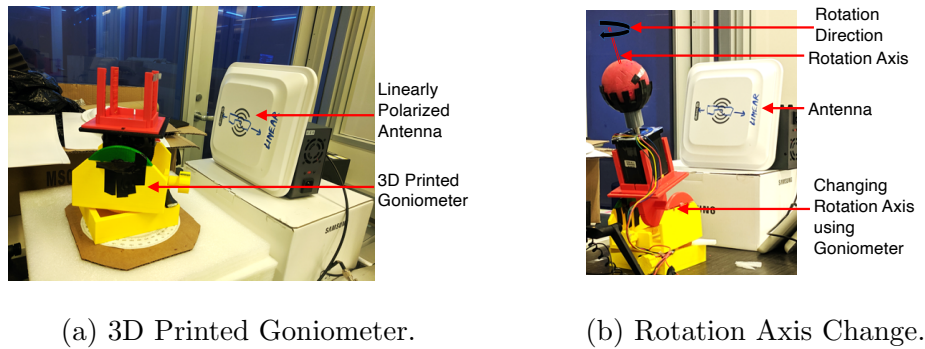
Figure 5.19: Rotation Setup for TIMU.
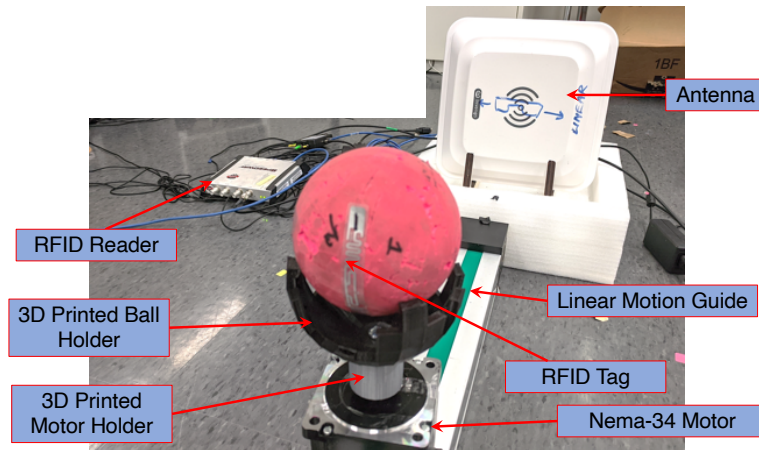
Figure 5.20: Magnified view of rotation Setup.

tation axis, rotation speed, distance, and AoA estimation. We then evaluate our algorithm under general motion involving both rotation and translation movement.

5.3.2.1 Estimate Rotation

First, we track rotation movement without translation motion. We fix the rotation axis in this experiment and put the ball in a static position. We

estimate the number of rotations per minute (RPM). For example, Fig. 5.21 shows the RSS patterns of different rotation speed (at 30RPM and 60RPM) at a fixed rotation axis.
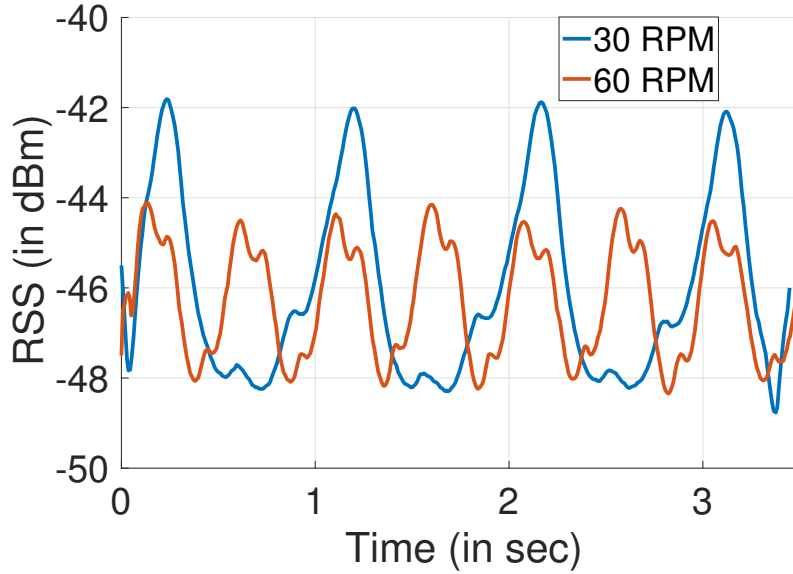
Figure 5.21: Example RSS patterns at Different RPM.

Estimating rotation speed: We use the periodic RSS change to estimate the rotation speed. Figure 5.22 plots the rotation speed estimation error as we vary the RPM, distance, rotation axis, and Angle-of-arrival (AoA) (azimuth in this case). As we can see, in all cases, we can accurately estimate the rotation speed. Fig. 5.22(a) because all errors in this case are 0. Overall, the error increases with the speed and distance we would expect due to false peak detection.Using the average of 3 tags reduces the RPM error by $20 - 25\%$ due to redundancy.

Estimating rotation axis: Next, we evaluate the rotation axis estimation

(a) Vary RPM

(b) Vary distance

(c) Vary rotation axis

(d) Vary AoA
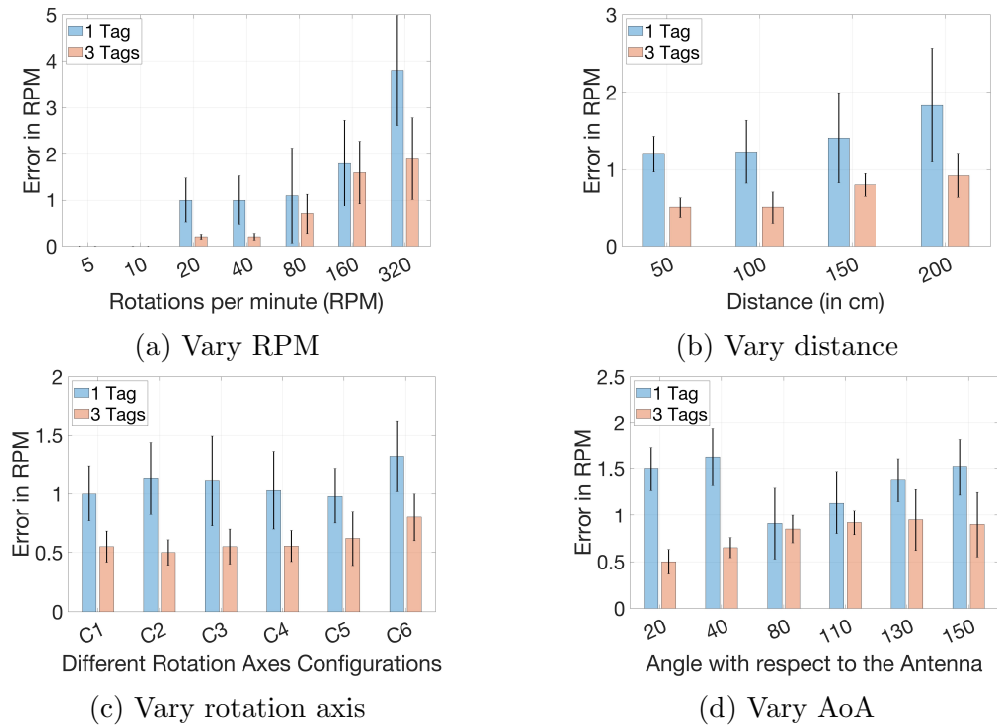
Figure 5.22: Rotation Speed vs RPM error.

(*i.e.*, the relative angle with each of the axes: Yaw (X), Pitch(Y), and Roll(Z)). Figure 5.23(a) plots the error in estimating the rotation axis as we vary the rotation speed. In this experiment, we create 36 possible configurations by changing X, Y, Z angles using a Goniometer. As we can see, the rotation axis errors are similar as we vary the rotation speed. Figure 5.23(a) shows that the errors in the three axes are around 5 degrees in all cases. Figure 5.23(b) shows that the error increases with the distance due to reduced received signal strength (RSS) resolution. Next, we separately vary the azimuth from 20 to 160 degree (20 degree apart), vary the elevation from 10 degree to 70 degree (20 degree apart), and their combinations to generate different $3D$ positions.

100

As shown in Figure 5.23(c), the median error is around 5 degrees when we vary only the azimuth or elevation axis. When we vary both, the error increases to 6 degrees.

(a) Vary speed (1m)

(b) Vary distance (80 RPM)

(c) Vary AoA (1m, 80 RPM)
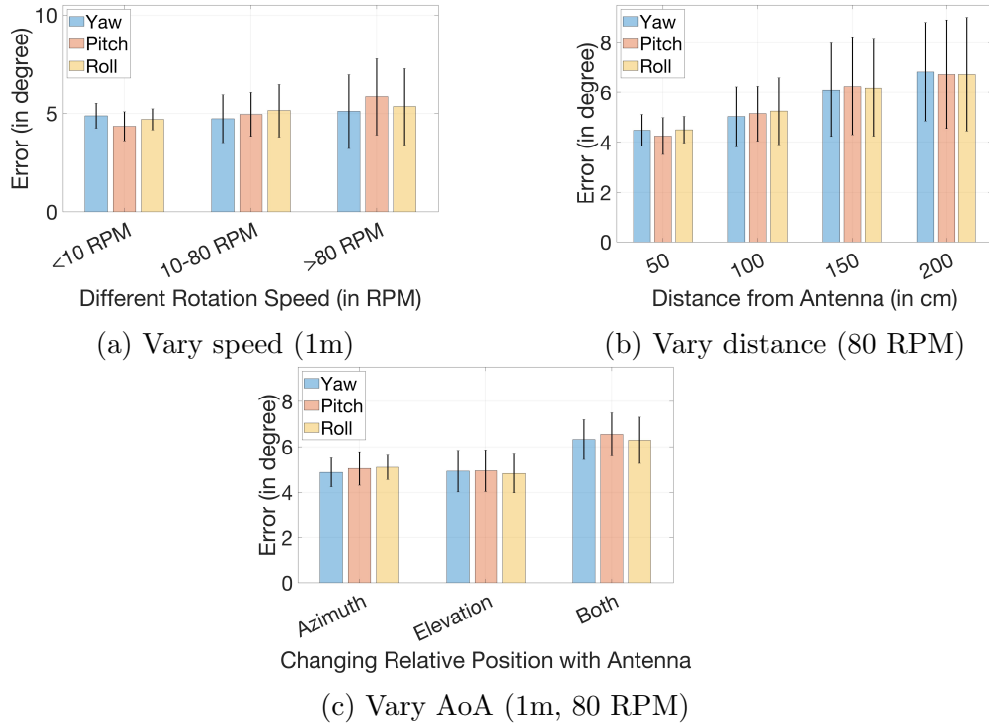
Figure 5.23: Rotation axis error along different axis with 36 possible configurations.

5.3.2.2 Estimation Translation Distance

Next, we consider the translation movement without rotation. Figure 5.24 compares the relative distance change error when we move the ball on the guide with translation movement at different speeds. We calculate the relative distance change using the phase change in one frequency. Fig. 5.24(a)

shows the CDF of the distance estimation error as we vary the speed. It shows that the error tends to increase with speed. Nevertheless, even at high speed (*e.g.*, over 0.5 m/s), the 90-percentile error is within 2 cm over a 2.5m travel range. Next, we change the azimuth from 20 degree to 150 degree while setting the ball speed at 10 cm/s. Fig. 5.24(b) shows the impact of azimuth on the distance estimation error is small.

(a) Vary Speed   (b) Vary Azimuth
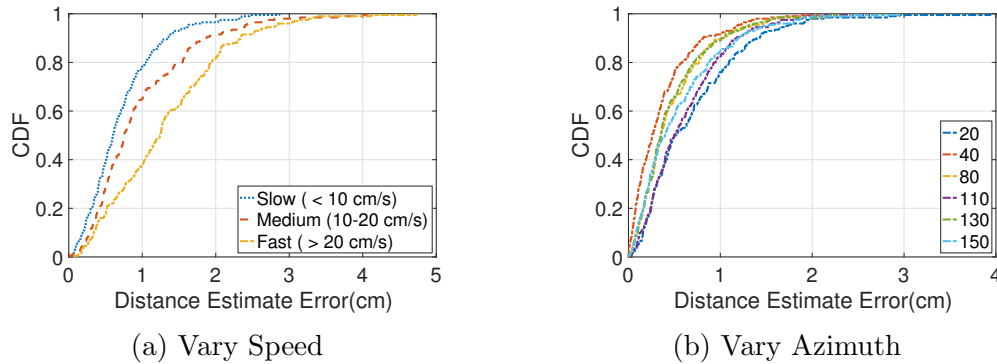
Figure 5.24: Relative Distance Error using 1 Frequency.

Next, we use two frequencies to estimate the absolute distance. Figure 5.25(a) compares the absolute distance error when the ball is stationary, and shows that even at different distances (up to 2m), the 90 percentile error is within 1.5 cm. Note that the data collection duration needs to be longer than the time required to get measurements from different frequencies for absolute distance estimation. Figure 5.25(b) compares the absolute distance error when the ball is moving at different speeds. As we can see, the 90 percentile distance estimation error is within 2.5cm.

(a) Vary Distances   (b) Vary Speed
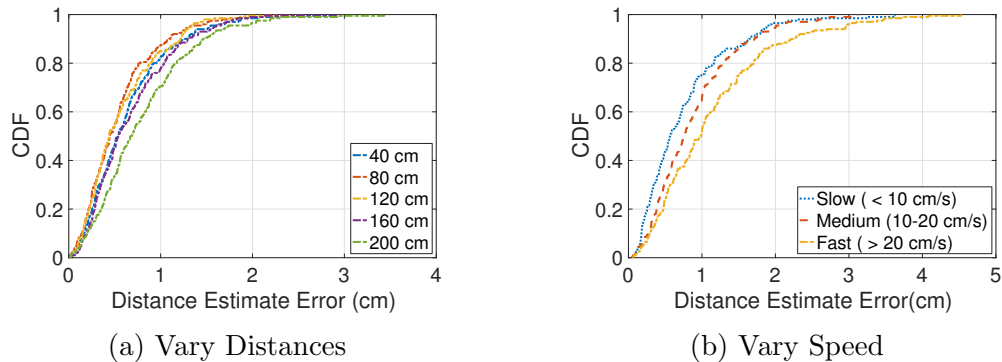
Figure 5.25: Distance Estimation Error using 2 Frequencies.

5.3.2.3 Estimating Azimuth and Elevation

Next, we estimate the azimuth (*i.e.*, the relative 2D angle with the antenna) and elevation (*i.e.*, the relative angle with the orthogonal plane), while keeping the other parameters the same. We change the azimuth from 20 to 160 degree (20 degree apart) and change the elevation 10 degree to 70 degree (20 degree apart), which cover 32 possible configurations. Fig. 5.26(a) shows that the azimuth estimation error is within 6 degree up to 2 m away when we change either the azimuth or elevation. Fig. 5.26(b) shows that when we change the azimuth and elevation together, our tracking achieves within 6.5 degree error at 1 m away. Fig. 5.26(c) and Fig. 5.26(d) show that both 90-percentile azimuth and elevation errors remain within 8 degree even if we vary the rotation speed at a 1m distance, validating the effectiveness of our algorithm for AoA tracking under different scenarios. As before, increasing distance and speed increases the error due to lower SNR and fewer samples during a rotation.

103

(a) Vary Distance (b) Vary configurations

(c) Vary rotation speed (2D) (d) Vary rotation speed (3D)
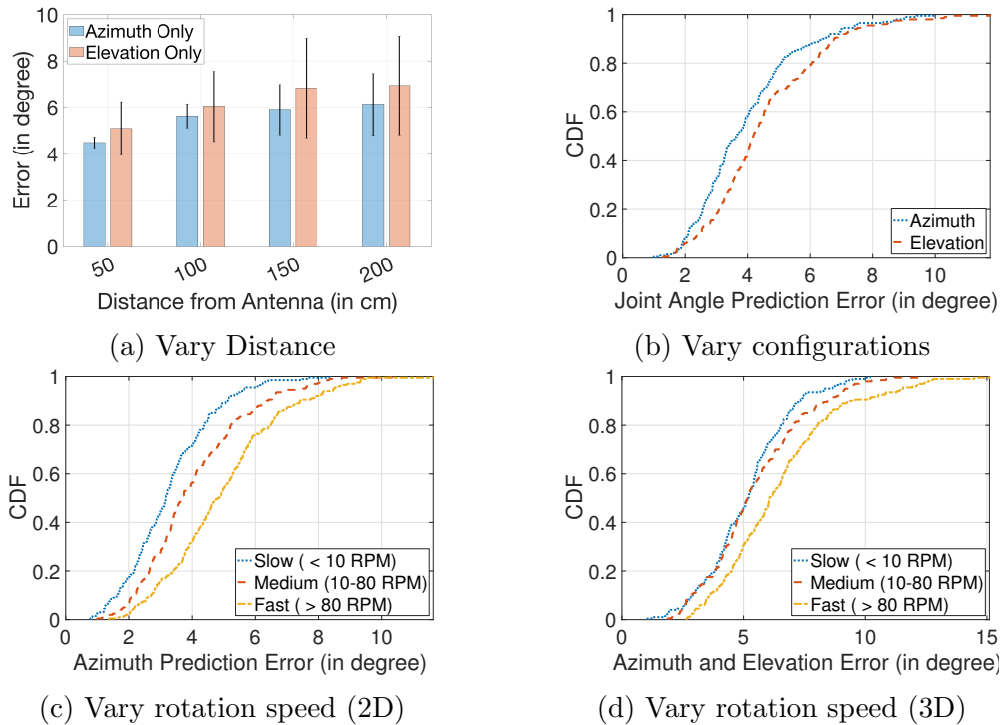
Figure 5.26: Azimuth & Elevation Error.

5.3.2.4 Estimate Moving Direction

To estimate the rotation direction, we change the rotation direction from 1m away by changing the azimuth from 20 to 160 degree (20 degree apart) with 6 different rotation axes. Using the same set of configurations, we move the ball from 2m distance toward and away from the RFID antenna to estimate the translation. As shown in Fig. 5.27(a), we can estimate the direction of translation movement with almost 100% accuracy at different speeds. Moreover, Fig. 5.27(b) shows that we can estimate the rotation direction accurately over 95% cases at a high rotation speed. We miss some of the cases due

to fewer samples and smaller change during a rotation in some configurations.

(a) Translation Direction   (b) Rotation Direction
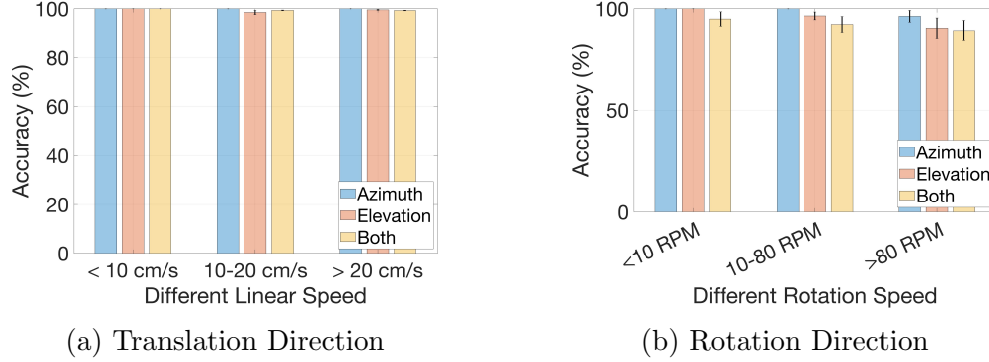
Figure 5.27: Moving Direction Estimation.

5.3.2.5 Rotation and Translation Movement

We change the rotation speed from 5 RPM to 100 RPM and the translation movement speed from 1 cm/s to 100 cm/s. By varying the azimuth from 20 to 160 degrees in 10 degrees apart and the elevation from 10 to 70 degrees in 10 degrees apart, and the rotation axes, we generate 64 possible rotation axis configurations. As shown in Fig. 5.28(a), when both the rotation and translation speeds are small, the 90 percentile error is within 2cm; when both speeds increase, this error increases up to 6.5cm. Fig. 5.28(b) shows the 90 percentile RPM errors are around 2 and 4 for these two scenarios, respectively.

Fig. 5.29 shows CDFs of the azimuth and elevation estimation error for a similar setup. As it shows, the 90 percentile estimation errors increase to 6 and 7.5 degree, respectively.

Furthermore, Fig. 5.30(a) shows the estimation error of different axes

105

(a) Distance Estimation

(b) Rotation Estimation
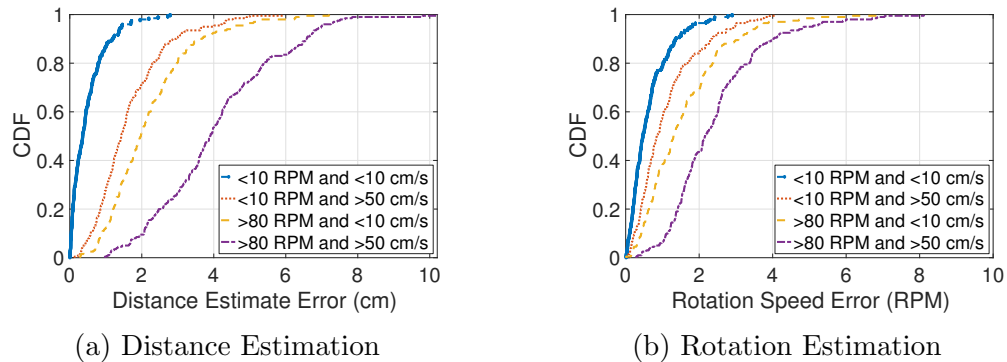
Figure 5.28: Error in Rotation & Translation Speed Estimation.

(a) Azimuth Estimation

(b) Elevation Estimation
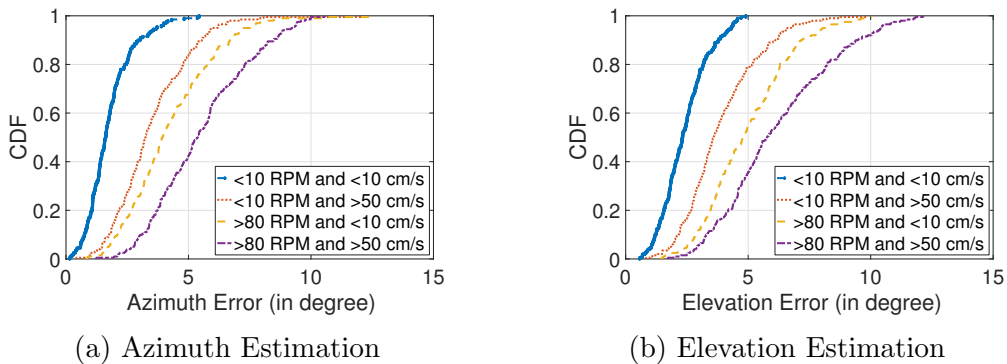
Figure 5.29: Error in Azimuth & Elevation Estimation.

at different rotation and translation speeds. The median error of rotation axis estimation is within 5 degree and the 90 percentile error is within 7.5 degree. Fig. 5.30(b) further compares the estimation error using our received signal model versus a simpler model that only considers the impact of the distance as in Tagyro [188]. As we can see, our algorithm yields much lower error: the median errors is within 5 degrees in our case versus 40 degrees in the other case.

Impact of blockage and multipath : We create a blockage by putting a

(a) Error in Rotation Axis Estimation.

(b) Comparing with Distance only Model.
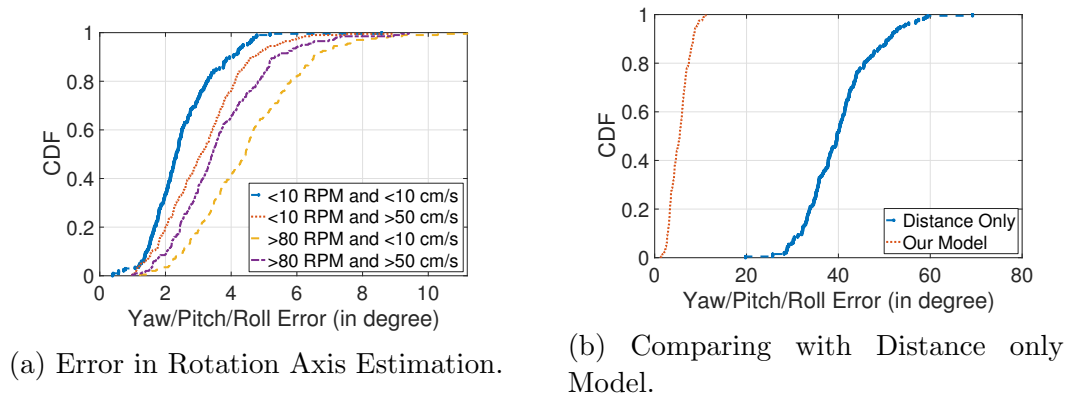
Figure 5.30: Error in Rotation Axis Estimation.

(a) LoS and NLoS (created via putting blockage before antenna) settings.

(b) Different configurations created by introducing 5 wooden (aluminium foil wrapped) reflectors.
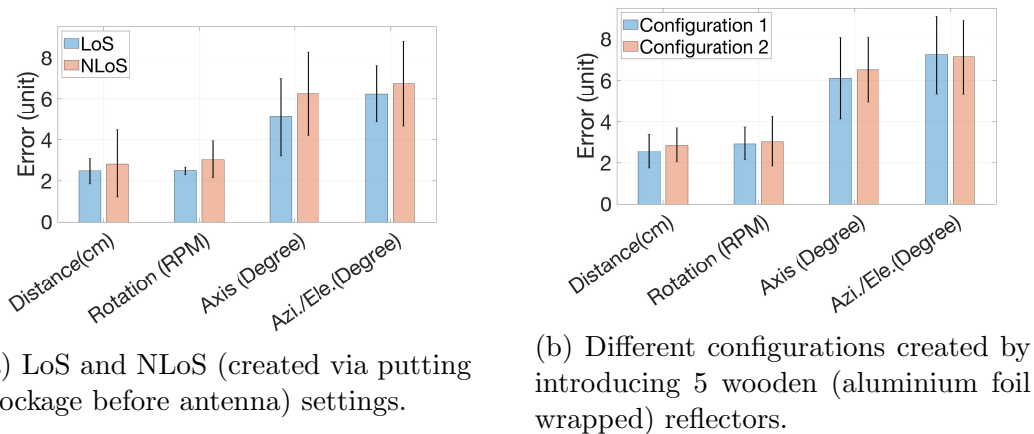
Figure 5.31: Performance in Non-line-of-sight (NLoS) setting and different static multipath setting.

wooden barrier (1 m × 1m large, 5 cm thick) in front of the reader antenna. We perform a subset of the previous experiments involving both rotation and translation. Fig. 5.31(a) shows that error increases within 10%. Blockage does not significantly increase the error since the RFID signal can penetrate through the obstacle.

Next, we introduce static multipath by placing 5 wooden reflectors
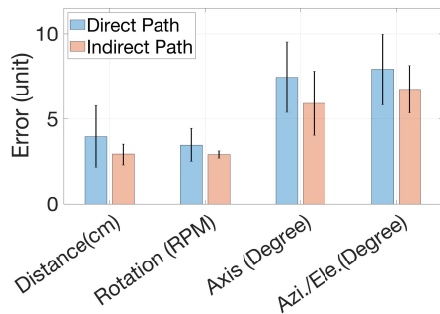
(a) Dynamic Multi-path situation is created when a user moves around impacting the direct and indirect paths.
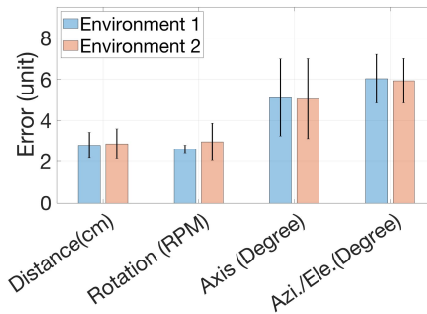
(b) Different Environments introducing different Multi-path related effect.

Figure 5.32: Environment 1 and Environment 2 differ in relative locations of the furniture and desktops in the lab.

wrapped with aluminum foil in the same way as the multipath experiments in Section 5.1.3. As shown in Fig. 5.31(b), the rotation axis and relative angle error are within 8 degree in both configurations. Moreover, the distance estimation and rotation speed estimation error remain small: within 3cm and 4 RPM, respectively.

To further evaluate the impact of multipath, we create dynamic multipath by moving the same wood barrier randomly between the tag and reader antenna (blocking) or near the tag and reader antenna (non-blocking). As shown in Fig. 5.32(a), the errors under dynamic multipath with and without blocking are 20% and 8-10% higher than in the typical setting (*i.e.*, LoS without dynamic multipath), respectively. Dynamic multipath increase errors in both cases. Blocking has higher errors due to reduced RSS. Nevertheless, the errors in both cases are low since the general trends under dynamic multipath remain similar, as shown in Fig. 5.8(c) and (d) (in Section 5.1.3).

We further evaluate the performance in two locations – a lab and a conference room when the calibration is performed in the lab. Fig. 5.32(b) shows that the errors are similar, which indicates the scheme is reasonably robust to the environment change.

Chapter 6

RTSense: RFID based Temperature Sensing

In this chapter, we propose and develop a passive RFID tag-based temperature sensing method called RTSENSE.

6.1   Overview

Accurate temperature information inside the buildings is essential, as people spend most (around 90 percent) of their time indoors [12]. Furthermore, there is also significant variation in temperature across a large building or even within a spacious room, which we also confirm using empirical measurement (as illustrated in Fig. 6.2). *Fine-grained real-time knowledge* of indoor temperature empower the future smart-spaces by enabling personalized thermal comfort systems for the occupants to promote their well-being [131, 96, 20, 92]. Furthermore, it can potentially be used to monitor the *heating, ventilation, and air conditioning* (HVAC) systems.

Inspired by this tag-antenna based sensing and due to the growing popularity of low-cost passive RFID tags, we explore the possibility of using passive RFID tags as temperature sensors. We observe, like [65], that temperature change can result in variation in the impedance of the RFID tag, and
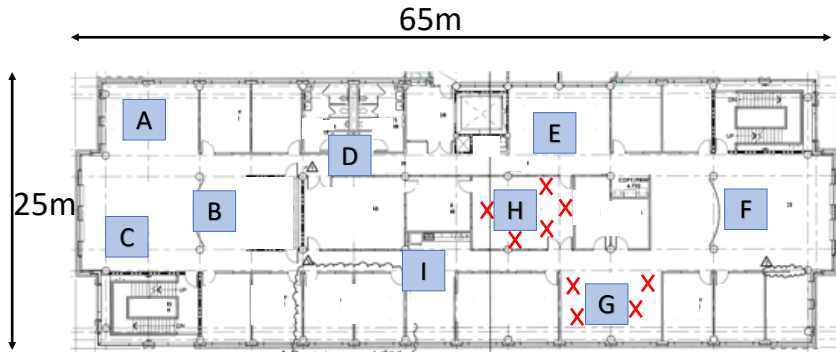
Figure 6.1: Building floor map and different temperature measurement sites. The box symbols denote the floor-level measurement locations and the cross symbols denote the room-level locations.

(a) Location Variation.
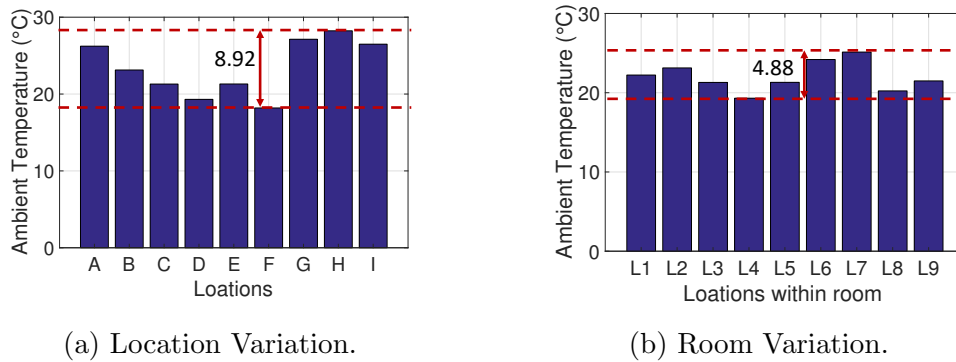
(b) Room Variation.

Figure 6.2: Temperature measurement variation across different locations and within the room. The temperature variation can go up to 9 degrees. The ambient temperature snapshots are taken in the 11 a.m. and 5 p.m. Non-uniform indoor temperature illustrates that ubiquitous temperature sensing is crucial to achieving indoor thermal comfort.

such a change can be captured using the phase of the received signal reflected by the RFID tag (like [68] with customized tags). Based on this relation, one can potentially map the phase change back to the temperature change. While intuitive, making it work well in practice involves several challenges: (i) how to

111

achieve high accuracy, (ii) how to be robust against the environmental change (since phase can change not only with the temperature but also with the environment and movement), and (iii) how not to decrease the sensing range [135]. These challenges are side-stepped in the previous tag-antenna based sensing works [64, 65, 68]. Closest to our work is [178], which although takes into account environmental impact in design while using Commercial Off-the-Shelf (COTS) setup, but suffers from lower sensing resolution and range due to the use of power-based metric [138, 135].
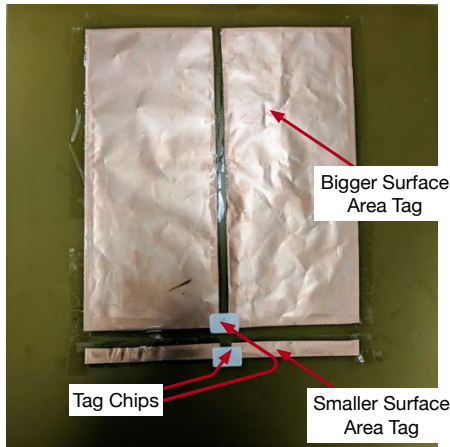
Figure 6.3: Tag-pair of RTSENSE.

To address (i), we develop an analytical model that captures the impact of temperature change on the reflected signal phase. The model helps us gain insight that larger antenna surface area results in more impedance change, which can be exploited in differential sensing. This approach opens up the possibility of achieving better resolution by exploiting the antenna surface. To address (ii), we use a pair of tags that respond differently to the

temperature and measure the phase difference between the two tags. The use of two tags allows us to cancel out the impact of environmental changes since both tags experience the same environmental change. Using these observations, we build the tag-pair by attaching RFID chip transponders to the dipole antennas, as shown in Fig. 6.3. This area-based tag-pair design helps us to develop an environment independent way of sensing room temperature, which in turn circumvents the problem of sensing range reduction (issue (iii)). Before arriving into the final design, we experiment with a variety of RFID setups for temperature sensing. We converge to a simple commercial RFID tag coupled with a custom-designed copper dipole antenna-based temperature sensor through experiments. Thus, we build a system called RTSENSE (*R*FID-based *T*emperature Sensing) using this tag-pair, which can be easily deployed in the walls of current buildings or future smart-spaces. We also use a specific phase-difference based metric to increase the robustness of the system. Fig. 6.4 illustrates the outline design of RTSENSE, which can facilitate the construction of a room-level thermal map of any building and help improve occupants' indoor thermal comfort.

6.2   Model-aided Design of RTSense

In this section, we will describe the underlying model of the impact of ambient temperature on phase manifestation and how this model helps create a phase-based metric for RTSENSE to predict the temperature in an environment-agnostic way. We will first describe different components of the

113
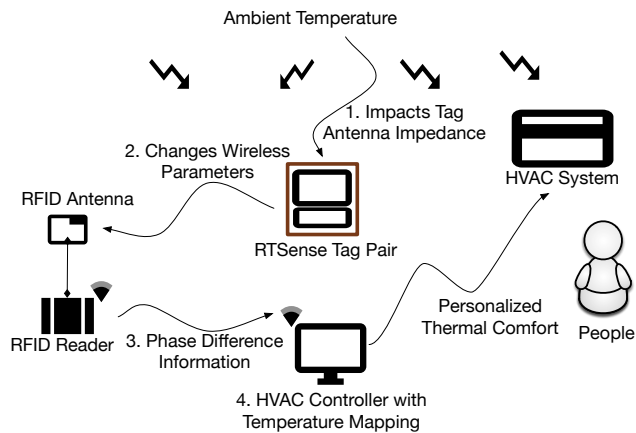
Figure 6.4: Design of RTSENSE.

analytical model by providing a brief context and then end with the phase-based metric used in RTSENSE.

6.2.1 Context

In RTSENSE, to simplify the antenna specific artifacts, we design and build the simplest possible antenna element, *i.e.*, dipole antenna, which is also a popular commercial RFID tag design [153, 79, 66]. According to [122, 136], the basic design guideline for any chipped RFID tag antenna is size reduction without sacrificing the conjugate matching [64, 122]. The key idea in our work is to relax this requirement of size reduction, as our use-case of temperature sensing inside buildings does not necessarily require that. Secondly, we use the variation of wireless parameter (more specifically phase) due to the impedance change in the passive antenna elements due to ambient temperature change. There are many previous works [64, 66, 138, 118], which reported this insight
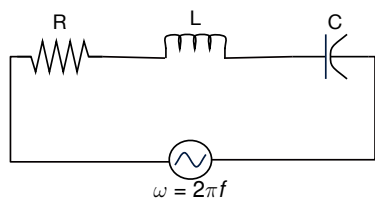
(a) Configuration 1 (C1).
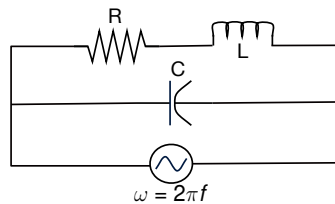
(b) Configuration 2 (C2).
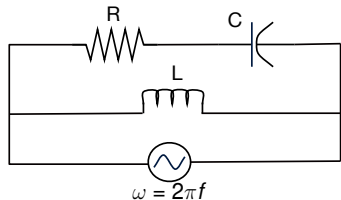
(c) Configuration 3 (C3).
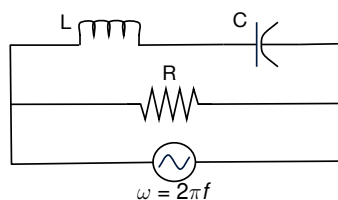
(d) Configuration 4 (C4).
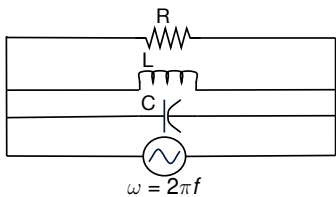
(e) Configuration 5 (C5).
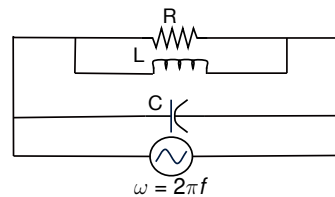
(f) Configuration 6 (C6).
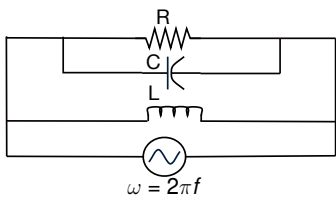
(g) Configuration 7 (C7).
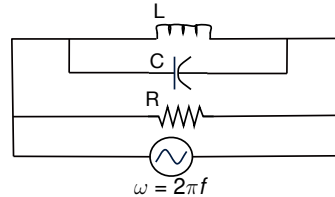
(h) Configuration 8 (C8).

Figure 6.5: Possible configurations of a RFID tag antenna.

and exploited this feature for sensing purposes. Unlike these works, we present an analytical model (rather than a data-driven approach) and incorporate that insight into our antenna design process by exploiting the antenna surface area. In the following, we first present the main components of analytical modeling.

6.2.2 Mapping Temperature to Impedance

In RTSENSE, we are employing tag-antenna based sensing and utilizing the manifestation of impedance change in the tag-antenna caused by the temperature variation. Therefore, we need to validate the impedance change modeling part. For achieving this, we need to know different electromagnetic components of a tag-dipole antenna, the configuration among these components, and the impact of temperature on these.

6.2.2.1 Components of antenna

As we have chosen the simplest possible dipole antenna design (other sophisticated antenna design varieties are left for future work), we first have to find the resistive, inductive, and capacitive components. Assume that, simple dipole antenna has a specific length (l), width (w), and thickness (t), and the frequency of the RFID continuous wave is given by f and the wave-length is λ. According to [171], the inductance (L) of this type antenna strip is

$$L[nH] = 0.2l[mm][ln(\frac{2l}{w+t}) + 0.5 + \frac{w+t}{3l}] \qquad (6.2.1)$$

Furthermore, resistance (R) has two components: AC resistance (which happens due to inductive coupling) and real DC resistance (which is the intrinsic characteristic of the metal strip). The DC resistance of this type of strip can be given by $\rho l/wt$ (where ρ is the resistivity constant depending upon metal, and for copper, the value is 1.68×10^{-8}) and the AC resistance is given by $80\alpha^2(\frac{\pi l}{\lambda})^2$ [66, 60] (Here, α is the term dependent upon the current distribution along the dipole). This AC resistance depends upon the skin-depth,

116

which increases with frequency [66, 144]. Suppose the current distribution is triangular (*i.e.*, maximum at the center and zero at the ends), then $\alpha = 0.5$ (we assume that). This phenomenon can only happen if the length of the dipole is $\lambda/2$, and we build our dipole taking into the frequency of operation. Furthermore, the capacitance (C) of the metal strip is given by $C = wt\epsilon/d$, where d is the distance between two dipole antenna halves. We get these initial components (R, L, and C) using these analytical models, and verify both with Ansys HFSS software [1] and LCR meter [10] (the analytical model matches very closely with the simulation in HFSS and LCR meter values).

6.2.2.2 Configurations with these components

The next step is to build an equivalent circuit with these components for executing the temperature based analysis. Although a few previous pieces of literature assume a simpler series R-L-C model like Fig. 6.5a, we found out that it does not reflect accurately in reality. For a given frequency f when we measure the impedance of the RFID tag using Array Solutions Vector Network Analyzer (VNA) [23] using an SMA connector. We observe that the real components of the measured impedance vector change across different samples at a fixed temperature, contrary to the series configuration. Because, if the tag antenna has an equivalent circuit according to the Fig. 6.5a, *i.e.*, a simple series R-L-C model, then the real components should have remained constant (as the following equation gives the equivalent impedance: $Z_{eq} = R + j(\omega L - \frac{1}{\omega C})$). Therefore, we create all 8 possible configurations, shown in

117

Fig. 6.5 and compare their measured impedance values (through VNA) with their simulated impedance values. We procure the simulated impedance values from the impedance equations using the standard electromagnetic models. For example, the impedance equations of Fig. 6.5e and Fig. 6.5b generally look like these:

$$Z_{eq} = \frac{R}{1 - R^2(\omega C - \frac{1}{\omega L})^2} - j\frac{R^2(\omega C - \frac{1}{\omega L})}{1 - R^2(\omega C - \frac{1}{\omega L})^2} \qquad (6.2.2)$$

and

$$Z_{eq} = \frac{R}{1 + \omega^2(R^2 C^2 - 2LC) + \omega^4 L^2 C^2} + j\frac{\omega(L - R^2 C) - \omega^3 L^2 C}{1 + \omega^2(R^2 C^2 - 2LC) + \omega^4 L^2 C^2}$$
$$(6.2.3)$$

respectively. Fig. 6.6 illustrates the average error for impedance magnitude of different configurations and shows that Fig. 6.5b provides the least error for impedance magnitude prediction. For the experiments in Fig. 6.6, we have selected copper dipole antennas of different area/length and measured the impedance using VNA at a fixed room temperature. This selection of parallel configuration instead of a series configuration also align with a few recent works [153, 69, 66]. Therefore, for our modeling impedance of dipole antenna in this chapter, we consider this configuration.

6.2.2.3 Temperature impact on impedance

If the physical parameter (Λ) (discussed in the previous section) is temperature, then we first need to analyze the impact on the impedance. The resistance of a given metal changes with the following equation [144]:

$$R_T = R(1 + \alpha(T - T_0)) \qquad (6.2.4)$$
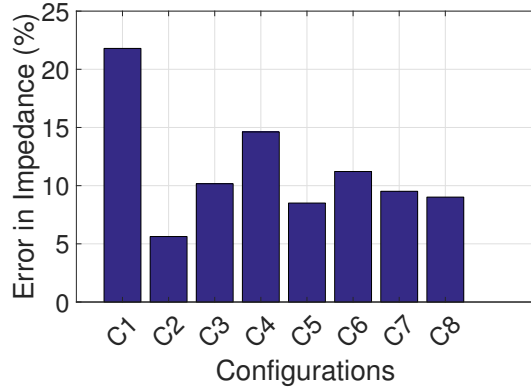
Figure 6.6: Average percentage error in impedance magnitude among different configurations in Fig. 6.5.
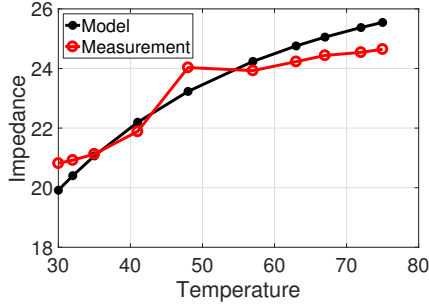
(a) Larger Width (30cm).
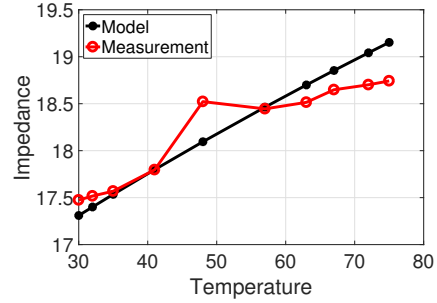
(b) Smaller Width (5cm).

Figure 6.7: Impedance prediction (Model vs VNA).

where, R_T is the temperature at T degree centigrade, T_0 is the room temperature, and α is the temperature coefficient of resistance change. We have chosen copper for our dipole antenna design, and the value of α for copper is 0.004041. The following equation gives the change of inductance with temperature:

$$L_T = \frac{1}{2\pi f w} \sqrt{\pi f \mu_0 \rho} \sqrt{1 + \gamma(T - T_0)} \qquad (6.2.5)$$

where μ_0 is the magnetic permeability, $\gamma = 0.0034$ per degree centigrade, and T_0 is considered as standard room temperature. Within our temperature

prediction interest zone, the change of capacitance of metal strip is very minimal [144], and we ignore that. For a given configuration, the impedance change will be the resultant change due to the temperature variation and impact on both resistance and inductance. We employ these values of resistive and inductive components with temperature variation in our configuration model to get the resultant impedance change. Then, we compare these results with the impedance calculated using VNA. We observe that for different antenna dimensions (5cm and 30cm respectively), the model and the measurement match very closely (as shown in Fig. 6.7). We also see that there is expectedly less impedance change for smaller area antenna (5cm compared to 30cm) because there are smaller values of R/L/C. This insight motivates us to exploit the antenna surface area for the differential sensing purpose.

6.2.3   Mapping Impedance to Phase

Now, we need to map this impedance change to the manifested phase. If we assume that r is the distance between the reader antenna and the tag (Therefore, the signal traverses a total distance of $2r$ due to back-scattering). Besides the phase change over distance, the transmitter, tag, and receiver circuits will all introduce some additional phase offsets, denoted as θ_T, θ_{TAG} and θ_R, respectively. The total phase change [35] observed by the reader can be expressed as:

$$\theta = (\frac{2\pi}{\lambda} \times 2r + \theta_T + \theta_{TAG} + \theta_R) \; mod \; 2\pi \qquad (6.2.6)$$

where λ is the wavelength. $\theta_T + \theta_R$ can be expressed as polarization mismatch $2\phi(\hat{r})$. θ_{TAG} can be expressed as $arg(\frac{1}{Z_A+Z_C(OFF)} - \frac{1}{Z_A+Z_C(ON)})$. If we assume $Z_C(OFF) \rightarrow \infty$ (*i.e.*practically very large) [68, 118], then the above equation can be expressed as:

$$\theta = (\frac{2\pi}{\lambda} \times 2r + 2\phi(\hat{r}) + arg(-\frac{1}{Z_A + Z_C(ON)})) \; mod \; 2\pi \qquad (6.2.7)$$

Λ changes the tag antenna impedance thus, the phase will be expressed as:

$$\theta = (\frac{2\pi}{\lambda} \times 2r + 2\phi(\hat{r}) + arg(-\frac{1}{Z_A(\Lambda) + Z_C(ON)})) \; mod \; 2\pi \qquad (6.2.8)$$

We now know that tag antenna impedance, dual tag chip impedance, voltage leakage, tag to reader antenna distance, polarization mismatch, and tag orientation impact the phase measurement at the reader side. In all these factors impacting the phase measurement of the back-scattered signal coming from the passive RFID tags, at a given location, we can assume that all the factors except impedance change due to temperature change and variable multi-path variation due to clutter, introduces a constant phase offset into the over-all phase measurement. Now, for the time being, if we ignore the impact of multi-path due to clutter, we can take the temporal phase difference from a single tag, and we can create an equation which only depends on the antenna impedance change, like the following:

$$\theta_{Diff.} = arg(-\frac{1}{Z_A + Z_C(ON)}) - arg(-\frac{1}{Z_A(\Lambda) + Z_C(ON)}) \qquad (6.2.9)$$

121
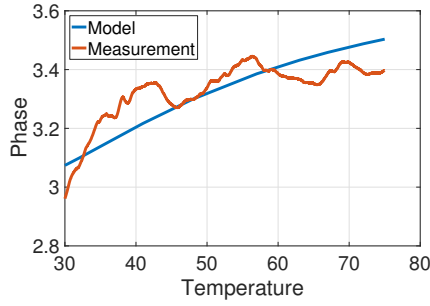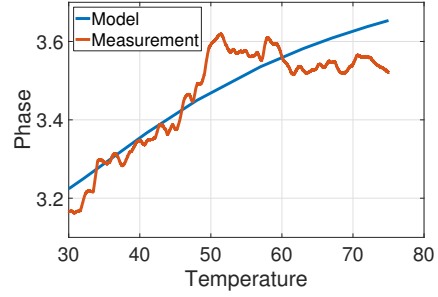
(a) Location 1. (b) Location 2.

Figure 6.8: Modeling phase change with temperature for 5cm width antenna.

Using this, we performed an experiment at a very small distance (within 10cm) (to ignore the clutter driven multi-path) inside an iso-temperature oven (as described in the setup later) and recorded the phase measurement from copper-based dipole tags of different areas. As illustrated in Fig, 6.8 and Fig. 6.9, the model-based phase difference measurement ($\theta_{Diff.}$) matches very closely with the measurement-based phase measurement. We perform the experiments at two different distances: 10cm and 15cm for a 5cm width and 30cm width antennas. Although there is a small variation in both figures (Fig. 6.8 and Fig. 6.9) due to multi-path artifact, the trends and the variation range match relatively well. This validates our configuration based temperature to phase modeling part. Now, in the absence of multi-path, we can ideally map from the phase measurement values to the temperature values if we have initial calibrated temperature reading. In the following sub-section, we introduce the system overview of RTSENSE, which shows how the temperature can be predicted accurately, even in the presence of the clutter.
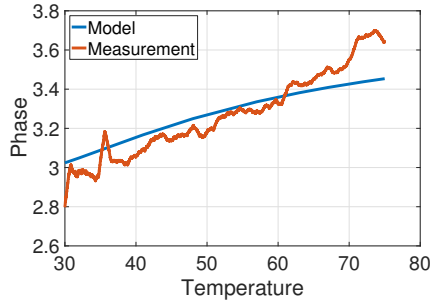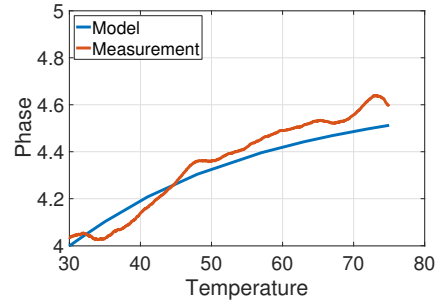
(a) Location 1.   (b) Location 2.

Figure 6.9: Modeling phase change with temperature modeling for 30cm width antenna.

6.2.4 Phase Difference Metric of RTSense

Context: To make RTSENSE robust for temperature prediction by using this tag-antenna based sensing, we have to address the issue of multi-path. The previously described model, inform us the following things: (i) Absolute metrics like a raw phase or power threshold or received signal strength (RSS) is setup-dependent and can not be used for any kind of generalized sensing which has also been reported in a few recent works [70, 138, 66], (ii) Differential sensing, *i.e.*, taking the difference with a reference value, is a more robust way forward. However, any power-based metrics (like the received signal strength or minimum threshold power) depend non-linearly upon many factors like antenna gains, transmitted power resolution, power transfer coefficients, etc. (as described in Eq. 6.2.9 and Eq. 2.5.2). Therefore, differential phase-based sensing (due to more straightforward relation) is a more pragmatic choice, (iii) Bigger the area of the dipole antenna (given a fixed length), the impedance change is more significant (Fig. 6.7(b)) and thus the finer phase

resolution. Building on these insights drawn from the model-design, we have opted for differential phase-based sensing through a tag-pair approach. In this case, one of the tags amplifies the temperature impact by utilizing the bigger surface area.
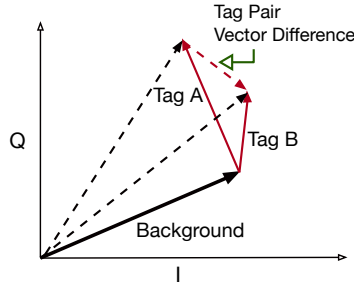
Figure 6.10: Tag vector phase difference.

Defining Metric: As discussed earlier, the measured wireless parameters ($P_{threshold}$, θ, δP_{rec} etc.) are dependent upon many factors, namely from the *distance*, *orientation* (both of the tag and the reader antenna), the type of antennas (*i.e.*, polarization mismatch), and the presence of reflectors in the tag read range (*i.e.*, multi-path). If we take the differential sensing approach (*i.e.*, the difference between two consecutive readings of the same type), we can only remove the static constant offsets like *distance*, *orientation* (both of the tag and the reader antenna) at a single particular location/configuration; however, we need to factor in the clutter-driven multi-path and different locations. To address that, we opt for the tag pair approach as in [70, 178], where we select two tags (say, Tag_{Big} and Tag_{Small}) of different areas as different areas exhibit

124

different impedance change (as $Z(\Lambda)_{Tag_{Big}} > Z(\Lambda)_{Tag_{Small}}$. Thus measured phase change due to the temperature variation, as $Z_C(ON)$ is the same in both tags due to the use of the same RFID chip/transponder.

We put these two tags very close-by (assuming there is similar mutual coupling impact on both of them) such that the background reflected backscatter signals are similar, as illustrated in Fig. 6.10. We create the signal vector coming from the back-scattered signals coming from the tag (by mapping RSS to the amplitude A and phase ϕ) as $A\exp^{j\phi}$. We then take the vector difference of two tag vectors, as shown in Fig. 6.10 and get the *argument* value of that difference. This vector difference helps us eliminate the background multi-path signal, as illustrated in Fig. 6.10. We collect these phase-vector differences of tag pairs for different temperatures and unwrap the value series for temperature prediction. In the next section, we describe how we utilize this phase difference parameter for temperature estimation.

6.3   RTSense: System Design

In this section, we describe how we utilize the model-aided tag-pair design and the phase-based metric for temperature sensing in RTSENSE. Temperature prediction system of RTSENSE tracking works in two stages: the calibration stage and the estimation stage.

Calibration stage: The initial calibration step is performed during the installation time. It is a simple low-cost step to record the phase difference

at the reader. During this step, Impinj R420 RFID reader continuously reads the tag-pair at a rate of 200 reads/second, and records the phases of all backscatter responses. Note that this is one-time effort and does not need to be repeated even when the tag orientation or distance changes. RTSENSE *normalizes* the phase-difference (after unwrapping them) with respect to the lowest value:

$$p(x) = r(x) - \min_x r(x), \quad T_{min} \leq x \leq T_{max} \tag{6.3.1}$$

where $r(x)$ is the (unwrapped) raw phase difference at temperature T, which changes from T_{min} to T_{max}. We calculate the normalized $r_{TagBig} - r_{TagSmall}$ during the calibration step. The temperature and phase are measured after installing the copper tag-pair with a ground plane. RTSENSE then uses polynomial curve-fitting to find the *third-order* polynomial that best fits the normalized calibration data. This calibrated polynomial is used for temperature estimation, even if the location or orientation of the tag-pair and RFID antenna changes. We apply the model calibrated using the data collected from a lab to the measurement collected in a conference room and observe 0.9 degree increase in the median error. This aspect suggests that calibration can potentially be done once and used later in an environment-independent way. To improve the temperature estimation accuracy through diversity, we extend our system to use three antennas 1m apart to estimate the temperature. We aggregate the estimations using a weighted average, and we call this approach RTSENSE (Multi).

To exploit frequency diversity (called RTSENSE (FD)) with multiple

126

antennas, we calibrate $p(x)$ using 30 channels ranging from 860 MHz to 920 MHz (2 MHz apart). We use USRP N2100 with SBX daughter-board. We capture the I/Q samples from the USRP to extract the relevant RF parameters. We use these calibrated polynomials to estimate the temperature and aggregate the estimations using a weighted average.
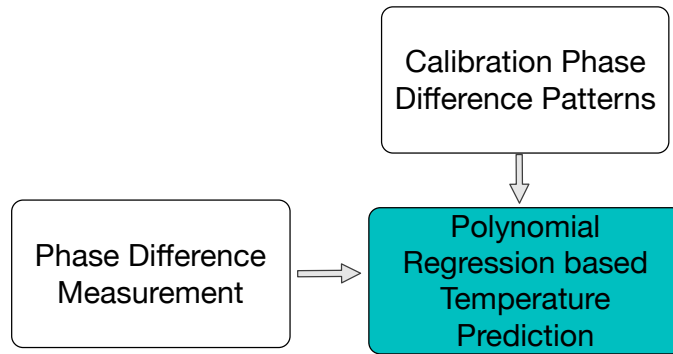
Figure 6.11: Algorithmic overview of RTSENSE.

Estimation stage: At the estimation stage, we use the newly measured phase difference to estimate the temperature, as shown in Fig. 6.11. We record the phase difference during 10 second and take an average. Then we put this average phase difference in the previously calibrated polynomial regression model to estimate the temperature. We can further leverage frequency diversity to calibrate and estimate for each frequency and combine the estimation results with improving the accuracy. We combine estimations from multiple frequencies using the weighted average, where the weights are inversely proportional to the RSS variation. A similar combination strategy is used to leverage

MIMO diversity [148]. We combine estimations from multiple antennas in the same way. We further compare with other combining schemes in Fig. 6.21.

6.4 Experimental Setup and Related Methodologies

In this section, we first describe the different experimental setups used to validate various observations, which are critical in building the *end-to-end* system of RTSENSE. Here we also describe other comparable methodologies that can be utilized for RFID-based temperature sensing.

6.4.1 Setup

Oven Setup: While validating the modeling part of temperature to phase of the copper-based dipole antennas, we experiment in a Fischer-Scientific iso-temperature oven [6] (shown in Fig. 6.12). This oven gives us the flexibility to fix the temperature and ensures that the temperature level remains the same throughout the setup. We connect the 0.02inch thick copper dipole antennas to the Vector Network Analyzer (VNA) [23] through the SMA connector (Fig. 6.13a) and use it inside the oven for validating the modeling part. Fig. 6.12 shows the experimental setup inside the oven and how the VNA is connected. We use an arduino [2] based temperature sensor Fig. 6.13b) [3] to capture the ground-truth of the temperature. This temperature sensing reading is time synchronized with the reader software and the VNA through a laptop.
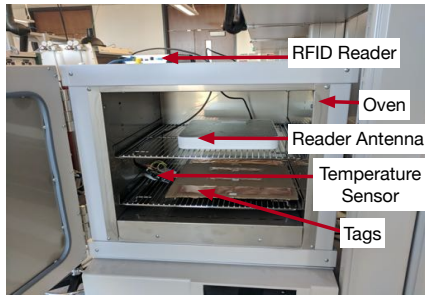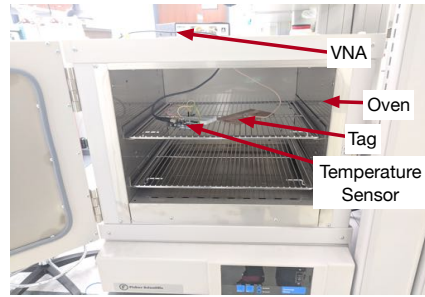
(a) Oven experiment.   (b) Oven experiment with VNA.

Figure 6.12: Iso-temperature oven experiment setup.

Lab Setup: We also perform the experiments with COTS UHF tags of four different varieties in the same oven experimental setup. The tags are Alien-9654 Higgs 3 (Tag1), Smartrac Frog-3D (Tag2), Alien-9640 Higgs-3 (Tag3), and, Alien-9768 Higgs 4 (Tag4) [18]. We also measure different ground-truth values of L-C-R through an LCR meter [10], to compare with our analytical model and Ansys HFSS software-based model. For performing different experiments by changing the distance and the orientation, we use a heat-gun in a cardboard setup, as shown in Fig. 6.14. We use the temperature sensor in tandem to record the ground-truth, and the cardboard box is used to contain the temperature in a closed space. We also perform the micro-benchmark experiments by changing the orientation, distance, etc. in this lab setup. Like the previous setup, the RFID reader, the temperature sensor, etc. are connected and synchronized through a laptop. To support multiple frequencies, we also use USRP N2100 [19] with SBX daughter-board [17] and two antennas as a reader, as shown in Fig. 6.15.
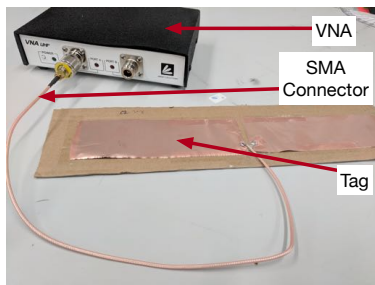
(a) VNA Setup.
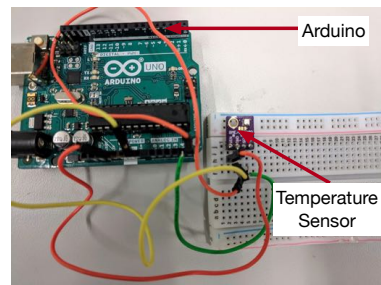
(b) Temperature Setup.

Figure 6.13: Different setup components.
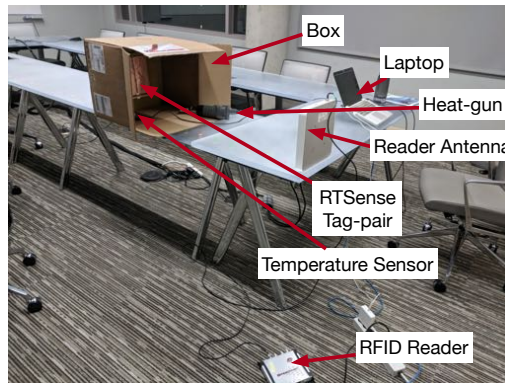
Figure 6.14: Experimental setup with a heat-gun.
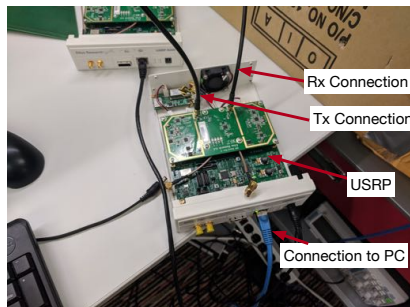
(a) USRP SBX Connection.
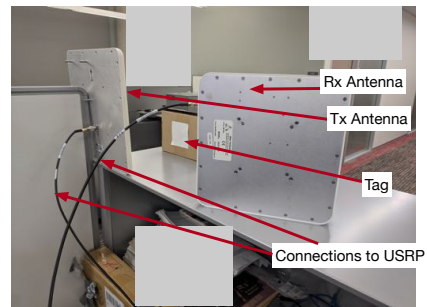
(b) USRP Antennas and Tag.

Figure 6.15: USRP Setup for RTSense (FD).

(a) Tag Design Type 1   (b) Tag Design Type 2
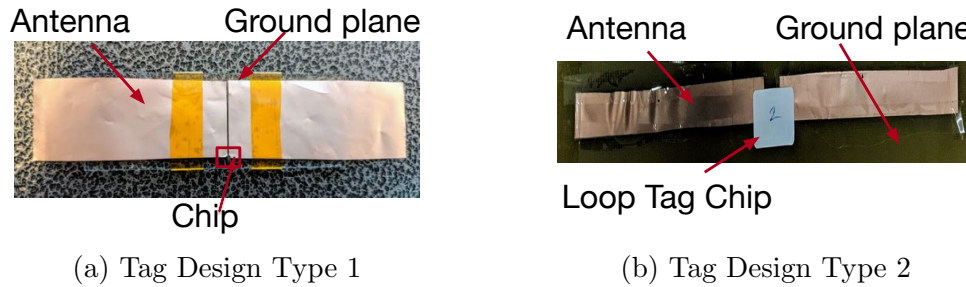
Figure 6.16: Two types of tag design.

Tag Design: In the following figures, we show two possible designs of custom copper tags used in RTSENSE. We create a simple copper dipole antenna based chipped passive RFID tags. In one design shown in Fig. 6.16a, we use the off-the-shelf transponder and carefully solder with the tag antennas. We have to connect two of the transponder connections to the separate dipole without shorting these for successful communication with the COTS reader. In an alternative design depicted in Fig. 6.16b, we use a smaller loop chipped tag (Alien-9613 Higgs-3) as the communicating element. The purpose of using this type of design is to promote a more accessible building of custom RFID tags for sensing purposes. If not specified explicitly, assume that we use the second type of tag design.

6.4.2   Methodologies

In this sub-section, we describe different comparable techniques that can be used for temperature sensing like RTSENSE. Although all these techniques are not originally designed or proposed for temperature sensing, we use these for comparison as these fall inside a similar landscape. Before discussing

the exact metrics used in the methodology, we also provide a brief background on a few parameters used.

Temperature Sensing with AID: An interesting metric has been presented in [124, 68], where a new parameter, the Analog Identifier (AID), has been proposed and evaluated. Through the intelligent combination of direct and reverse link power parameters, the AID attempts to eliminate the environmental influence, and it is given by the following equation:

$$AID = \frac{p_c}{2\sqrt{P_{R \leftarrow T} P_{threshold}}} = \alpha R_C \mid \frac{1}{Z_A + Z_C} \mid \tag{6.4.1}$$

where p_c is the chip sensitivity (*i.e.*, minimum amount of power (in dB) required to power up the chip which can be procured from the data-sheet), and $P_{R \leftarrow T}$ is the back-scattered signal strength. However, inherently, AID suffers from the limited resolution available both for $P_{threshold}$ (Eq. 2.5.2) and $P_{R \leftarrow T}$ (0.25 dBm for Impinj R420 reader [25]) and the dependence on RSS, *i.e.*, $P_{R \leftarrow T}$ for value calculation. We calculate AID for both COTS UHF tags and copper tags for temperature prediction in our experiments as this is a single-tag based metric.

Temperature Sensing with single tag Phase Difference (PD): Like this paper [70] used the phase difference metric for chemical sensing purpose, we use the same metric $\Delta\phi(t) = \phi(t) - \phi(0)$, where $\phi(0)$ is the reference state. We use similar calibration and regression based technique of RTSENSE, to predict the temperature value using this single-tag phase difference metric.

132

Temperature Sensing with Differential Minimum Threshold Power (DMRT): Recently a paper [178] proposed to use a commercial UHF tag-pair and to instrument one of the tags with a related sensor. We adopt this *hackable* way for our temperature sensing use-case using the mentioned sensor using *Tag3*, where we calculate the $P_{threshold}(A) - P_{threshold}(B)$ (Eq. 2.5.2) where Tag_A is the instrumented tag and Tag_B is not. This technique is power-based technique like AID and non-real-time. It depends upon a set of tag-pair like RTSENSE.

Temperature Sensing with tag-pair Phase Difference (PPD): We also compare with a variation of our phase-difference based metric, but it just uses the absolute phase difference between tag-pair at the reader side without taking the vector based phase difference. Specifically, for this metric, we calculate: $\phi_{Tag_A} - \phi_{Tag_B}$ where Tag_A is the tag with bigger antenna surface area (*i.e.*, prone to more phase change w.r.t. same temperature change) and Tag_B is the tag with smaller antenna surface area.

6.5   Implementation Details

Next, we describe the implementation detail of the tag designs and the hardware used in RTSENSE. The RFID setup used in RTSENSE consists of an ETSI-based Impinj R420 reader, which continuously queries the tag-pair in the range at around 200 reads/second using circular polarized antennas with 9dBi gain [16]. We use 867.5MHz for our experiments and record the responses of the tags at different temperature levels in both the oven and heating gun

setup. Apart from this basic COTS reader setup, we implement a software-based RFID reader [8] in USRP N2100 [19] with a SBX daughter-board [17] with two circularly polarized antennas (in GNURadio v3.74). Then we collect the I/Q samples of the reflected signal from the tag to extract the RSS and phase of the signal. The USRP is necessary to support higher bandwidth (*e.g.*, 860 MHz to 920 MHz) to achieve higher accuracy. We also use the Vector Network Analyzer (VNA) of Array Solutions, which sweeps up to 1GHz to measure the antennas' impedance. The VNA is connected to the copper dipole antenna with an SMA connector, as shown in Fig. 6.13a. We record the impedance components in the connected laptop through simultaneous queries.

Apart from the tag and transponder used in RTSense, we also use commercial RFID tags, as shown in Fig. 6.17. It operates between $860 - 920$ MHz. These tags include different types of dipole antennas, such as clover-leaf, tip-load, T-match, and spiral shape. For AID and DMRT, we change different power levels using LLRP protocol through JAVA SDK in Impinj Reader and record the RF phase and RSS in all responses. In our frequency diversity approach, we employ the frequency sweep of 80 MHz through a USRP based implementation. We use 0.02 inch thick copper [4, 76] with a particular RFID transponder [13] and the ground-plane of FR4 substrate [7]. We use Fisher Scientific's iso-temperature oven [6] in our experiments and an Arduino-based [2] temperature sensor [3] in Fig. 6.13b to record the ground-truth temperature for quantifying the sensing error. This temperature sensor module [3] has 0.5°

134

C accuracy. We use a Macbook Pro running OS Sierra with a 8GB RAM and i5 quad-core processor to process the data. We also try processing the data on Raspberry Pi 3 Model B [14] with 1.2 GHz quad-core Broadcom processor and 1 GB RAM. It takes around 1 second on the laptop and 6.5 second on the Raspberry Pi 3 to process the temperature estimation data. Both processing speeds are adequate for real-time monitoring.

6.6   Evaluation

We perform extensive experiments to evaluate RTSENSE. Initially, we start with the basic observation of phase change with the temperature in both COTS UHF tags and custom-designed copper-based dipole tags and justify the design choice. We show a simple copper-dipole based tag-pair design that can open up an exciting sensing opportunity. Next, we compare phase-based sensing with other power-driven methods. We also show that multiple antennas and frequency diversity also help improve sensing accuracy. We perform some micro-benchmark experiments by changing the multi-path setting, distance, area of the tag antenna, and orientation of the tag-pair relative to the RFID antenna setup. We also show the performance of alternative curve-fitting based techniques in the estimation stage of RTSENSE.

6.6.1   Rationale behind tag-pair design

Why not COTS UHF Tags? We start with COTS UHF RFID tags with different types of dipole antenna design, as shown in Fig. 6.17. Fig. 6.18

135
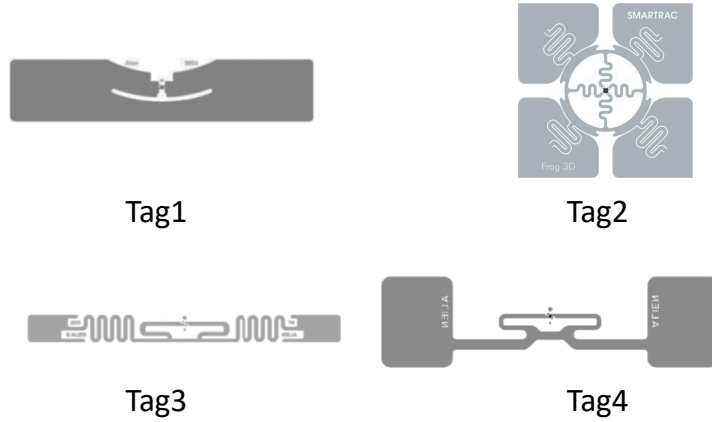
Figure 6.17: Types of COTS UHF tags used.

shows the phase change for the four types of tags when we vary the temperature. As we can see, the phase does not change monotonically, making it challenging for temperature sensing. The non-monotonic phase change is primarily due to the complex antenna-design artifacts, which causes polarization mismatch and mutual coupling between tag antenna elements [122]. If one looks carefully at Fig. 6.18, one can find out more variation in phase-change patterns in *Tag2* and *Tag3*. This phenomenon happens due to their folded-dipole design, which influences two electromagnetic fields, and spiral-design with T-match loading causes non-uniform current distribution [79, 60]. Since it is hard to modify antenna design and material used in COTS UHF tags through fabrication, we choose to attach a rectangular dipole antenna to COTS loop tags, which involves minimum modification. Therefore, the fundamental reason behind this behavior is the shape and the material used in COTS UHF tags. Furthermore, because of this non-monotonic non-uniform

136

behavior, the phase difference metric between two different UHF tags with the different areas will not yield good results.
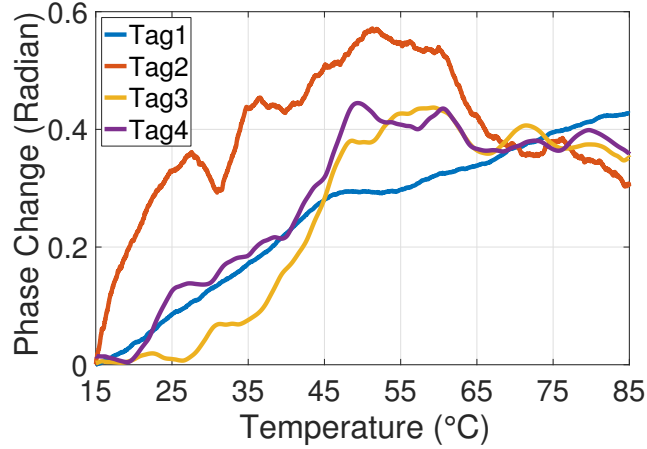
Figure 6.18: Single COTS UHF tag phase change pattern. Experiments are performed in the oven.

Why area-based tag pair? We use a simpler antenna design (*i.e.*, a dipole antenna) with a widely-available copper. Our model suggests that under the same temperature change, a larger antenna results in larger impedance change and more phase variation. To further confirm this insight, we perform an experiment by changing the antenna surface area of copper dipole tag from 2cm to 30cm while fixing the dipole length constant (17.30cm), which is equivalent to half the wavelength according to [60, 122, 66]). Fig. 6.19 shows a larger surface area yields a larger phase change. For example, 70 degree celsius change results in 1.7 radian phase change in a 30cm wide dipole antenna, but only 0.3 radian phase change in 2 cm wide antenna. Therefore, a larger copper dipole-antenna based tag provides better resolution and higher accuracy

137

in temperature sensing. We use a tag-pair to cancel out the impact of other environmental factors.
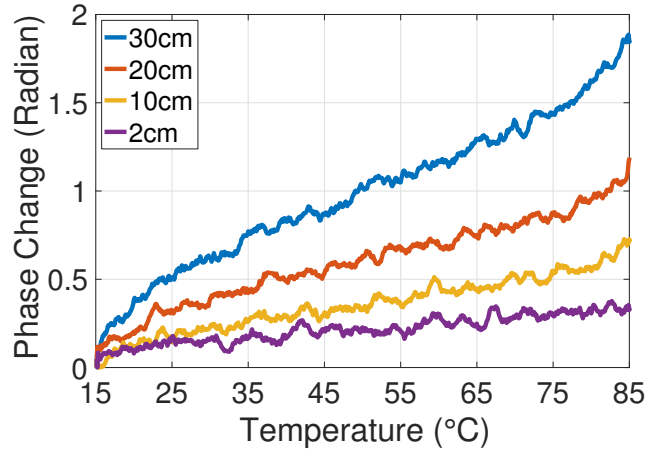
Figure 6.19: Phase change pattern of custom-designed tags with different areas. Experiments are performed in the oven.

Fig. 6.19 shows the phase changes increases with the antenna size. Fig. 6.20 shows that changing the temperature from 15 degree celsius to 85 degree celsius results in 1.32 radian phase difference in the 30cm-2cm tag-pair, but only results in 0.3 radian phase change in the 10cm-2cm tag-pair. We add the chip to this tag-pair design by attaching either a chip transponder or smaller loop tags, as explained earlier. This phenomenon also makes the design process simple. Note that we do not go beyond 30cm area since exceeding 30 cm will result in detuning. To reduce the surface area in certain applications, one can *fold* the copper to reduce the area.
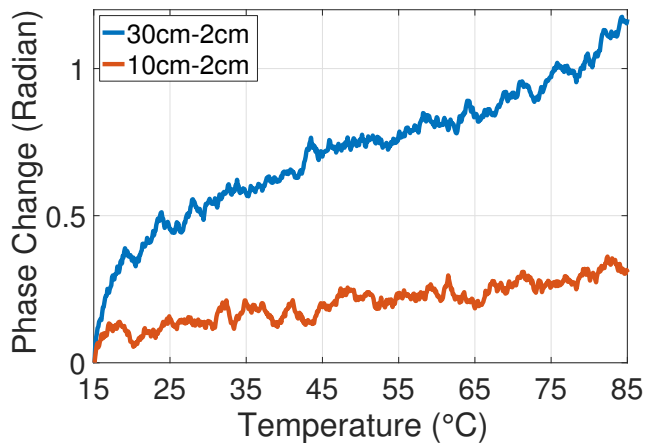
Figure 6.20: Phase change pattern of a pair of custom-designed copper tags with different areas in the oven.

6.6.2 Comparison with Other Methodologies

In this subsection, we compare RTSENSE with other methodologies mentioned before. Before comparing with other methodologies, We first evaluate RTSENSE (FD), which uses multiple frequencies. In Fig. 6.21, we combine the temperature estimations from different frequencies using the following schemes: (i) assigning weights inversely proportionally to the signal strength variation, i.e., giving more weight to the frequencies which have less variation in signal strength at any particular temperature, (ii) assigning equal weights to all frequencies, and (iii) selecting the maximum or minimum of the temperature estimations across frequencies. In all these combination schemes, weights are normalized such that the weights sum up to 1 across all frequencies. As we can see from Fig. 6.22, (i) performs the best and yields around 2.9° centigrade median error.

Fig. 6.22 shows that RTSENSE performs better than the other schemes. We perform these temperature experiments using a heating-gun from 200cm away. The median error of RTSENSE using one antenna is around 6°. Using 3 antennas (1 m apart) reduces the median error to around 4° (RTSENSE (Multi)). Using 60 MHz bandwidth (consisting of 30 channels 2 MHz apart) and 3 antennas (RTSENSE (FD)) further reduces the error to 2.9° celsius by exploiting the frequency diversity. In comparison, AID and DMRT yield around 24°, which is consistent with the 20 degree resolution and 32° error reported by the authors of AID and DMRT. Moreover, the power changes non-monotonically with the temperature, as shown in Fig. 6.23.

Besides, the power-based schemes degrade if there is a minor change in the setup due to the impact of the multi-path and lower resolution of the power level of commercial devices. According to Eq. 2.5.2, power is a non-linear function of many factors, including the gain of tag-antenna and transmit power, etc. Furthermore, this moderate resolution is also due to the coarse power resolution. In our case, it is 0.25dBm in the Impinj RFID reader.

The range of DMRT or AID based metric is limited. For these two methods, we only report the error up to 1.5m distance, which is the maximum range we can collect the data. DMRT is not easy to repeat since it is sensitive to the multi-path. Adding a sensor to the tag also detunes the tag heavily, and the impact is amplified when the temperature changes, which may cause failure in reading the tag. AID has limited accuracy due to the coarse resolution of received signal strength and $P_{threshold}$. Furthermore, performing a sweep across
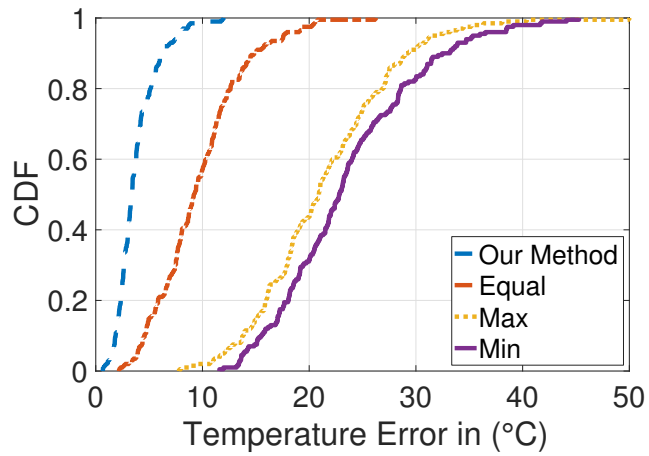
Figure 6.21: Temperature estimation error with different strategies in RTSense (FD).
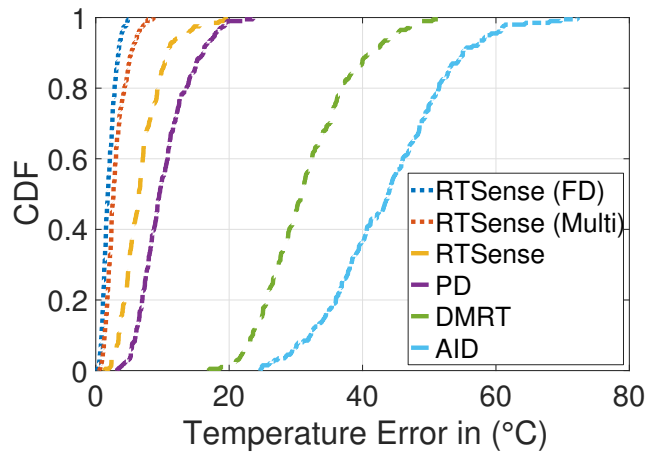
Figure 6.22: Temperature estimation error with different strategies in RTSense (FD).

different power levels is time-consuming. For example, it takes several minutes to sweep all power levels for our reader.

In comparison, the phase-based metric performs better in terms of range, resolution, robustness, and delay. RTSense works up to 3.5m range,

(a) AID Example.　　　　　　　　(b) DMRT example.
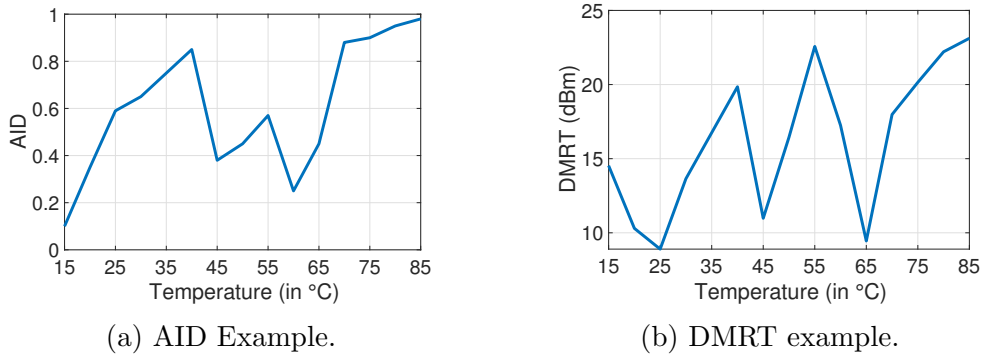
Figure 6.23: Example patterns with temperature change.

even in non-line-of-sight. Interestingly, other phase-based techniques (namely PD) also out-performs the power-based approach. As shown in Fig. 6.22, PD yields a median error of $10°$ centigrade since it is sensitive to other environmental change due to the lack of differential sensing approach.

6.6.3　Micro-benchmark Experiments

In this subsection, we perform different micro-benchmark experiments by changing the tag orientation, tag to antenna distance, and antenna surface area. We also change the static multi-path by moving the furniture around and perform experiments in different locations.

Impact of Distance:　We first evaluate the impact of the distance on RTSENSE. We change the distance of the antenna from 50cm to 350cm. We calibrate the phase-difference trend at 50cm distance. Fig. 6.24a shows that although the temperature estimation error increases slightly with the distance,

(a) Distance change. (b) Different schemes.
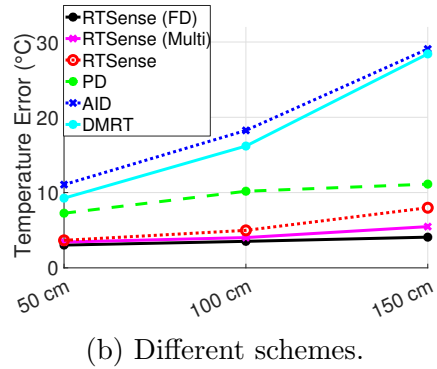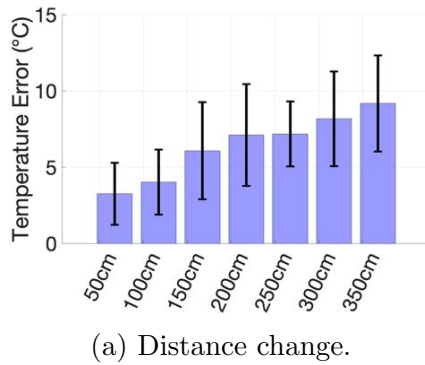
Figure 6.24: Temperature estimation error with distance change. Experiments are performed using the heat-gun setup.

(a) Orientation change. (b) Different schemes.
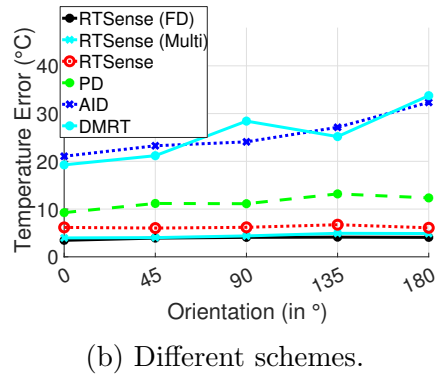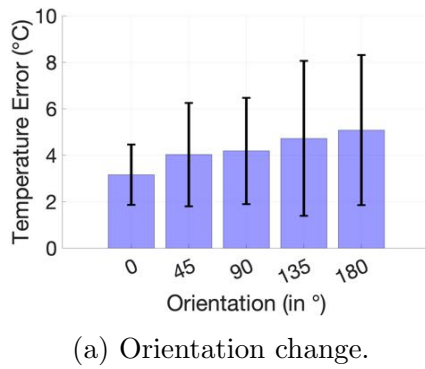
Figure 6.25: Temperature estimation error with orientation change. Experiments are performed with the heat-gun setup.

but the median error remains within 7.5° error even when it is 3.5m away. We also compared with other techniques within the 1.5m range due to the range limitation in power based schemes and observe that RTSense performs the best, as shown in Fig. 6.24b. The error in AID or DMRT can go up to around 30° centigrade. We can further increase the sensing range by using a higher gain antenna or MIMO technique (*e.g.*, beam-forming [177]).

Impact of Orientation: Next we change the tag orientation from 0° to 180° on a single plane, as shown in Fig. 6.25b. Since we use the tag-pair based approach in RTSense, the polarization mismatch due to different orientations cancels out. Therefore, we observe similar error range at different orientations for RTSense, as shown in Fig. 6.25a. Fig. 6.25b shows that the single-tag based techniques like PD or AID suffers significantly from polarization mismatch, and their errors can go beyond 30° centigrade. In this experiment, we perform calibration at 100cm distance with 0° orientation and measure at 100cm distance while changing the temperature.

Impact of Antenna Area Change: In this experiment, we perform the calibration at 100cm away with 0° orientation and measure at 100cm away while changing the temperature. We change the surface area of the larger tag-antenna from 5cm to 50cm. As shown in Fig. 6.26a, 30cm is the optimal in our copper-dipole tag-pair based setup with the COTS chips. Note that the performance does not monotonically increase with the antenna size since while increasing the antenna size increases the phase difference between the two antennas, but it can cause antenna and tag chip impedance mismatch, which can degrade the accuracy. 30 cm provides a good trade-off between these two factors.

Impact of Calibration Location: To evaluate the dependence of location in the calibration stage, we perform the calibration from the data

144

(a) Antenna area change.

(b) Temperature estimation error when there is dynamic multi-path present.
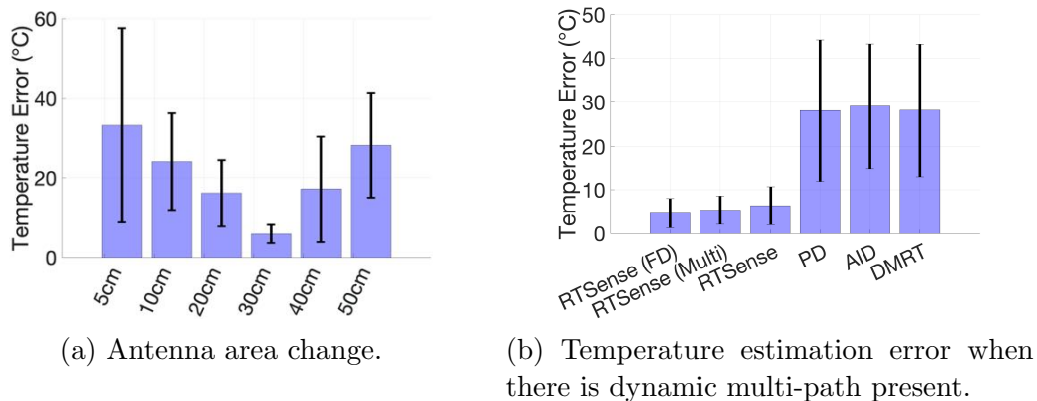
Figure 6.26: Temperature estimation error with antenna area change and change in dynamic multi-path. Experiments are performed with the heat-gun setup.
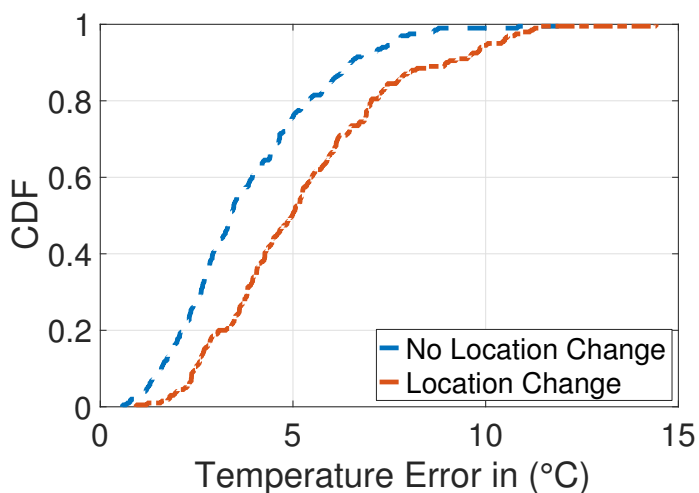
Figure 6.27: CDF of Temperature estimation error in RTSense(FD) when the calibration is performed in same and different location respectively.

collected at a conference room and perform the estimation in another room and vice versa. For these experiments, we have collected 5 sample runs at 5 different distances starting from 50cm and ranging up to 350cm. However, we did not change the antenna orientation for these experiments. Fig. 6.27

145

illustrates that the median temperature estimation error does not veer away much, and the overall trend remains similar. The median estimation error worsens approximately 0.9 degree when the location is different in calibration and estimation stages.

(a) Location 1.   (b) Location 2.
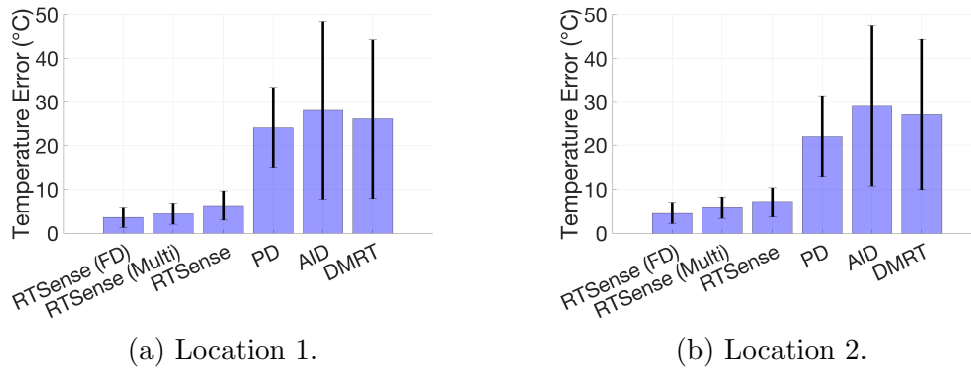
Figure 6.28: Temperature estimation error with static multi-path changes at two different locations. Experiments are performed with the heat-gun setup and multi-path change is performed by reorganizing the furniture.

Impact of Multi-path: To observe the multi-path effect, we evaluate in two different rooms. We observe that the error is in the same region, as shown in Fig. 6.28. We also re-organize the furniture in each room across different runs to change the static multi-path. Even if the calibration and estimation distance remains the same, the phase-based schemes perform better than the power-based schemes. Fig. 6.28a shows that when we change the static multi-path, the median temperature estimation error in PD increases up to 24° centigrade, but the error of RTSense, RTSense (Multi) and RTSense (FD) remain around 6° centigrade (C), 5° C, and 4° C, respectively. The

146

power-based temperature estimation techniques suffer as shown in Fig. 6.28a and Fig. 6.28b. In these experiments, we perform calibration at 150cm away with 0° orientation and measure at 150cm distance.

Furthermore, in the bigger room, we create dynamic multi-path by having a user move around and occasionally block the line-of-sight path. Fig. 6.26b shows that PD has around 30° C mean error while RTSENSE (FD), RTSENSE (Multi), and RTSENSE have around 4°, 5°, and 6° C mean errors, respectively.

Technique	Median Error (°C)
LR	18.34
LR with Regularization	18.38
PR with Degree 2	8.13
PR with Degree 3	**6.12**
PR with Degree 3 (3 antennas)	**3.8**
PR with Degree 3 (with 60 MHz)	**4.2**
PR with Degree 3 (multiple with 60 MHz)	**2.9**
PR with Degree 4	7.29
PR with Degree 5	8.39

Table 6.1: Error in RTSense with Other Techniques.

6.6.4 Impact of Fitting Functions

In this section, we examine a few simple alternatives in the estimation stage of RTSENSE. We conduct measurement in a conference room using the

147

heating gun setup. We measure from 200cm away. We fit the measured phase difference and temperature using polynomial regression (PR) with degree 3. Table 6.1 shows the results of other regression. In all cases, we use the data collected from the ground-truth temperature. As we can see, the 3rd-degree polynomial regression provides the best performance with a median error of 6.12° centigrade using narrow-band frequency; increasing the bandwidth to 30 channels reduces the error to 3.8° C; increasing the antennas to 3 reduces the error to 4.2° C; using both high bandwidth and 3 antennas results in the lowest error of 2.9° C. Linear regression does not work well since the data is inherently non-linear. Using a too high order polynomial increases the error due to over-fitting.

Chapter 7

Conclusion

In this dissertation, we develop novel techniques to sense a wide array of surrounding information. These include touch interaction, the environmental temperature, and motion information of moving objects.

Firstly, we develop and evaluate RIO, touch, and gesture UI primitive for smart spaces. RIO enables fine-grained touch tracking using COTS RFID reader and tags, and low-overhead training and installation. RIO is designed to be easily embedded into existing environments to turn them into smart spaces. Our evaluations demonstrate that RIO is a robust touch and gesture sensing primitive under various real-world situations. RIO also supports custom-designed RFID tags for a fully integrated UI design, and our proof-of-concept applications highlight possible interfaces that can be built with RIO. Furthermore, RIO is also the first step towards a novel battery-free interface design and presents many opportunities for future exploration into this space. Some possible extensions of our work include two-dimensional gesture tracking, multi-touch tracking, etc. and custom interfaces built using different materials.

Secondly, in RTSENSE, we develop an analytical model to understand

how impedance and phase change with the temperature. We also propose a novel approach that uses phase to sense the temperature. We implement a customized tag-pair and measure the phase difference of the received signals from two tags with different sizes to estimate the temperature change. Our evaluation shows the promise of our approach. As part of our future work, we plan to improve accuracy by exploring antenna design, custom chip design, and material selection. In this work, we start with the temperature sensing in RTSENSE using copper tag-pairs, we would like to extend to sensing other properties such as humidity and light. This solution can be achieved by selecting an appropriate material sensitive to the physical property being sensed.

Finally, in TIMU, we design a passive RFID-tag based motion-sensing system for a moving ball using a single commercial-off-the-shelf antenna. To our knowledge, it is the *first* battery-free sensing system that uses a single RFID reader antenna to sense general motion. This solution is achieved by leveraging the polarization and non-uniform antenna gains in the passive RFID system. Our system can accurately estimate the rotation and translation motion of a moving ball. As part of our future work, we are interested in developing several applications based on our sensing approach.

Bibliography

[1] Ansys hfss: 3d electromagnetic field simulator for rf and wireless design. https://www.ansys.com/products/electronics/ansys-hfss.

[2] Arduino uno r3. https://www.amazon.com/Arduino-A000066-ARDUINO-UNO-R3/dp/B008GRTSV6/.

[3] Bme280 pressure temperature sensor module. https://www.amazon.com/Diymall-Pressure-Temperature-Sensor-Arduino/dp/B0118XCKTG/.

[4] Copper foil 110 annealed. https://bit.ly/2Fnet5b.

[5] Enhancing bluetooth location services with direction finding. https://www.bluetooth.com/bluetooth-resources/enhancing-bluetooth-location-services-with-direction-finding/.

[6] Fisher scientific isotemp 637g oven. https://www.marshallscientific.com/Fisher-Scientific-Isotemp-637G-Oven-p/Fi-637G.htm.

[7] Fr4 copper-clad board. https://www.amazon.com/MG-Chemicals-Copper-Board-Single/dp/B008OAFKUS/.

[8] Gen2 uhf rfid reader with usrp and gnu radio.
https://github.com/nkargas/Gen2-UHF-RFID-Reader/.

[9] Hawk-eye ball tracking system.
https://www.hawkeyeinnovations.com/products/ball-tracking.

[10] High frequency lcr meter.
https://hiokiusa.com/product/impedance-analyzer-im3570/.

[11] Hot-spot in cricket. https://bit.ly/2nFyOw8.

[12] The indoor generation and the health risks of spending more time
inside. https://bit.ly/2XR7FUs.

[13] Nxp semiconductors sl3s1002ftb1,115. https://bit.ly/2W9Sswc.

[14] Raspberry pi 3 model b.
https://www.raspberrypi.org/products/raspberry-pi-3-model-b/.

[15] Rfm3200 wireless flexible temperature sensor.
https://axzon.com/rfm3200-wireless-flexible-temperature-sensor/.

[16] Rfmax indoor rfid antenna. https://www.atlasrfidstore.com/rfmax-
s9028pcr-s8658pcr-rhcp-indoor-rfid-antenna-fcc-etsi/.

[17] Sbx 400-4400 mhz rx/tx (40 mhz).
https://www.ettus.com/all-products/sbx/.

[18] UHF RFID Tags. https://www.atlasrfidstore.com/rfid-tags/.

[19] Usrp n210. https://www.ettus.com/all-products/un210-kit/.

[20] The effects of high and low ambient temperatures on human sleep stages. *Electroencephalography and Clinical Neurophysiology*, 51(5):494 – 501, 1981.

[21] Ieee approved draft standard for information technology–telecommunications and information exchange between systems - local and metropolitan area networks–specific requirements part 11: Wireless lan medium access control (mac) and physical layer (phy) specifications. *IEEE P802.11-REVmc/D8.0, August 2016*, pages 1–3774, Jan 2016.

[22] Alien 9613 higgs-3 loop near-field rfid tag. https://www.atlasrfidstore.com/alien-sit-rfid-white-wet-inlay-aln-9613-higgs-3/, 2017. [Online] Last Accessed : 07/12/2017.

[23] Array Solutions VNA-UHF - Two Port Vector Network Analyzer, 5 kHz to 1200 MHz. https://www.arraysolutions.com/vna-uhf, 2017. [Online] Last Accessed : 07/12/2017.

[24] Epc/rfid llrp standards. http://www.gs1.org/epcrfid/epc-rfid-llrp/1-1-0, 2017. [Online] Last Accessed : 07/12/2017.

[25] Impinj speedway uhf rfid reader.
https://www.impinj.com/products/readers/, 2017. [Online] Last
Accessed : 07/12/2017.

[26] ipod click wheel. http://bit.ly/2gfTW2z, 2017. [Online] Last Accessed
: 07/12/2017.

[27] Microsoft pixelsense - higher than 4k resolution.
https://www.microsoft.com/en-us/surface/devices/surface-
studio/innovation, 2017. [Online] Last Accessed :
07/12/2017.

[28] Monza r6 datasheet. https://support.impinj.com/hc/en-
us/articles/202765328-Monza-R6-Product-Datasheet, 2017. [Online]
Last Accessed : 07/12/2017.

[29] Mutual coupling in antenna arrays. https://nus.edu/2o5J8IN, 2017.
[Online] Last Accessed : 07/12/2017.

[30] Octane sdk for impinj.
https://support.impinj.com/hc/en-us/articles/202755268-Octane-SDK,
2017. [Online] Last Accessed : 07/12/2017.

[31] Opencv python 3.1.0.3. https://pypi.python.org/pypi/opencv-python,
2017. [Online] Last Accessed : 07/12/2017.

[32] Rfid coil antennas. http://bit.ly/2h8wLZI, 2017. [Online] Last
Accessed : 07/12/2017.

[33] Smartrac dogbone rfid paper tag (monza 4d).
https://www.atlasrfidstore.com/smartrac-dogbone-rfid-paper-tag-
monza-4d/a, 2017. [Online] Last Accessed :
07/12/2017.

[34] Specification for rfid air interface epc radio-frequency identity protocols
class-1 generation-2 uhf rfid protocol for communications at 860
mhz960 mhz. http://bit.ly/2gem5Ie, 2017. [Online] Last Accessed :
07/12/2017.

[35] Speedway revolution reader application note low level.
http://bit.ly/2geiFVA, 2017. [Online] Last Accessed : 07/12/2017.

[36] Thinkmagic rfid redaer. http://bit.ly/2tZeZ3w, 2017. [Online] Last
Accessed : 07/12/2017.

[37] 3 axis nema34 stepper motor driver.
https://www.amazon.com/dp/B07DX83J46/, 2020. [Online] Last
Accessed : 03/01/2020.

[38] Alien squiggle rfid white wet inlay (aln-9740, higgs-4).
https://www.atlasrfidstore.com/alien-squiggle-rfid-white-wet-inlay-aln-
9740-higgs-4/, 2020. [Online] Last Accessed :
03/01/2020.

[39] Arduino uno rev3. https://store.arduino.cc/usa/arduino-uno-rev3,
2020. [Online] Last Accessed : 03/01/2020.

[40] Goniometer. https://en.wikipedia.org/wiki/Goniometer, 2020.
[Online] Last Accessed : 03/01/2020.

[41] High range gyroscopes.
https://www.analog.com/en/products/sensors-mems/gyroscopes.html,
2020. [Online] Last Accessed : 03/01/2020.

[42] High speed belt driven linear actuator with stepper motor.
https://www.fuyumotion.com/high-speed-belt-driven-linear-actuator-
with-stepper-motor.html, 2020. [Online] Last Accessed :
03/01/2020.

[43] Invengo xc-af26 high gain rfid antenna.
https://www.atlasrfidstore.com/invengo-xc-af26-high-gain-rfid-
antenna/, 2020. [Online] Last Accessed :
03/01/2020.

[44] Linear motion system controller card for cnc machine.
https://www.fuyumotion.com/linear-motion-system-controller-card-for-
cnc-machine.html, 2020. [Online] Last Accessed :
03/01/2020.

[45] Nema 34 single shaft stepper motor 640 oz-in.
https://www.amazon.com/Nema-Single-Shaft-Stepper-
Motor/dp/B007QM5VEU, 2020. [Online] Last Accessed :
03/01/2020.

[46] Optasports. https://www.optasports.com/, 2020. [Online] Last Accessed : 03/01/2020.

[47] Sports analytics market worth 5.2 billion dollars by 2024. https://bit.ly/2y4eglX, 2020. [Online] Last Accessed : 03/01/2020.

[48] Sportsradar. https://sportradar.us/, 2020. [Online] Last Accessed : 03/01/2020.

[49] Statsperform. https://www.statsperform.com/, 2020. [Online] Last Accessed : 03/01/2020.

[50] Synergy sports. https://corp.synergysportstech.com/, 2020. [Online] Last Accessed : 03/01/2020.

[51] Fadel Adib, Zachary Kabelac, and Dina Katabi. Multi-person localization via RF body reflections. In *12th USENIX Symposium on Networked Systems Design and Implementation (NSDI 15)*, pages 279–292, 2015.

[52] Katsuaki Aga, Hiroo Tarao, and Shiro Urushihara. Calculation of human body resistance at power frequency using anatomic numerical human model. *Energy Procedia*, 89:401 – 407, 2016. CoE on Sustainable Energy System (Thai-Japan), Faculty of Engineering, Rajamangala University of Technology Thanyaburi (RMUTT), Thailand.

[53] S. Amendola, L. Bianchi, and G. Marrocco. Movement detection of human body segments: Passive radio-frequency identification and machine-learning technologies. *IEEE Antennas and Propagation Magazine*, 57(3):23–37, June 2015.

[54] S. Amendola, G. Bovesecchi, A. Palombi, P. Coppa, and G. Marrocco. Design, calibration and experimentation of an epidermal rfid sensor for remote temperature monitoring. *IEEE Sensors Journal*, 16(19):7250–7257, Oct 2016.

[55] Parvin Asadzadeh, Lars Kulik, and Egemen Tanin. Gesture recognition using rfid technology. *Personal Ubiquitous Comput.*, 16(3):225–234, March 2012.

[56] S. E. Asl, M. T. Ghasr, M. Zawodniok, and K. E. Robinson. Preliminary study of mutual coupling effect on a passive rfid antenna array. In *2013 IEEE International Instrumentation and Measurement Technology Conference (I2MTC)*, pages 138–141, May 2013.

[57] Daniel Avrahami and Scott E. Hudson. Forming interactivity: A tool for rapid prototyping of physical interactive products. In *Proceedings of the 4th Conference on Designing Interactive Systems: Processes, Practices, Methods, and Techniques*, 2002.

[58] A. A. Babar, S. Manzari, L. Sydanheimo, A. Z. Elsherbeni, and L. Ukkonen. Passive uhf rfid tag for heat sensing applications. *IEEE*

Transactions on Antennas and Propagation, 60(9):4056–4064, Sep. 2012.

[59] P. Bahl and V. N. Padmanabhan. Radar: an in-building rf-based user location and tracking system. In *Proceedings IEEE INFOCOM 2000. Conference on Computer Communications. Nineteenth Annual Joint Conference of the IEEE Computer and Communications Societies (Cat. No.00CH37064)*, volume 2, pages 775–784 vol.2, March 2000.

[60] Constantine A. Balanis. *Antenna Theory: Analysis and Design.* Wiley-Interscience, New York, NY, USA, 2005.

[61] L.K. Baxter. *Capacitive Sensors: Design and Applications.* IEEE Press Series on Electronics Technology. John Wiley & Sons, 1996.

[62] R. Bhattacharyya, C. Floerkemeier, and S. Sarma. Low-cost, ubiquitous rfid-tag-antenna-based sensing. *Proceedings of the IEEE*, 98(9):1593–1600, Sep. 2010.

[63] R. Bhattacharyya, C. Floerkemeier, and S. Sarma. Rfid tag antenna based sensing: Does your beverage glass need a refill? In *2010 IEEE International Conference on RFID (IEEE RFID 2010)*, pages 126–133, April 2010.

[64] Rahul Bhattacharyya, Christian Floerkemeier, and Sanjay E. Sarma. Low-cost, ubiquitous rfid-tag-antenna-based sensing. *Proceedings of the IEEE*, 98:1593–1600, 2010.

159

[65] Rahul Bhattacharyya, Christian Floerkemeier, and Sanjay E. Sarma. Rfid tag antenna based temperature sensing. *2010 IEEE International Conference on RFID (IEEE RFID 2010)*, pages 8–15, 2010.

[66] Miodrag Bolic, David Simplot-Ryl, and Ivan Stojmenovic. *RFID Systems: Research Trends and Challenges*. Wiley Publishing, 1st edition, 2010.

[67] Benjamin D Braaten, Gregory J Owen, and Robert M Nelson. Design of space-filling antennas for passive uhf rfid tags. INTECH Open Access Publisher, 2010.

[68] M. C. Caccami, S. Manzari, and G. Marrocco. Phase-oriented sensing by means of loaded uhf rfid tags. *IEEE Transactions on Antennas and Propagation*, 63(10):4512–4520, Oct 2015.

[69] M. C. Caccami and G. Marrocco. Electromagnetic modeling of self-tuning rfid sensor antennas in linear and nonlinear regimes. *IEEE Transactions on Antennas and Propagation*, 66(6):2779–2787, June 2018.

[70] S. Caizzone, E. Digiampaolo, and G. Marrocco. Investigation of suitable parameters for setup-independent rfid sensing. In *2015 International EURASIP Workshop on RFID Technology (EURFID)*, pages 98–102, Oct 2015.

[71] S. Capdevila, L. Jofre, J. Romeu, and J. C. Bolomey. Passive rfid based sensing. In *2011 IEEE International Conference on RFID-Technologies and Applications*, pages 507–512, Sep. 2011.

[72] Matthew Chalmers and Ian Maccoll. Seamful and seamless design in ubiquitous computing. Technical report, In Proceedings of Workshop At the Crossroads: The Interaction of HCI and Systems Issues in UbiComp. 2003, 2003.

[73] C. Chen, Y. Chen, Y. Han, H. Lai, and K. J. R. Liu. Achieving centimeter-accuracy indoor localization on wifi platforms: A frequency hopping approach. *IEEE Internet of Things Journal*, 4(1):111–121, Feb 2017.

[74] C. Chen, Y. Chen, Y. Han, H. Lai, F. Zhang, and K. J. R. Liu. Achieving centimeter-accuracy indoor localization on wifi platforms: A multi-antenna approach. *IEEE Internet of Things Journal*, 4(1):122–134, Feb 2017.

[75] N. Cho, J. Yoo, S. J. Song, J. Lee, S. Jeon, and H. J. Yoo. The human body characteristics as a signal transmission medium for intrabody communication. *IEEE Transactions on Microwave Theory and Techniques*, 55(5):1080–1086, May 2007.

[76] D. D. Deavours, K. Demarest, A. Syed, D. D. Deavours, K. Demarest, and A. Syed. Effects of antenna material on the performance of uhf

rfid tags. In *2007 IEEE International Conference on RFID*, pages
57–62, March 2007.

[77] M. Deng and D. Campbell-Wilson. The cloverleaf antenna: A compact
wide-bandwidth dual-polarization feed for chime. In *2014 16th
International Symposium on Antenna Technology and Applied
Electromagnetics (ANTEM)*, pages 1–2, July 2014.

[78] Han Ding, Longfei Shangguan, Zheng Yang, Jinsong Han, Zimu Zhou,
Panlong Yang, Wei Xi, and Jizhong Zhao. Femo: A platform for
free-weight exercise monitoring with rfids. In *Proceedings of the 13th
ACM Conference on Embedded Networked Sensor Systems*, SenSys '15,
pages 141–154, New York, NY, USA, 2015. ACM.

[79] Daniel M. Dobkin. *The RF in RFID, Second Edition: UHF RFID in
Practice.* Newnes, Newton, MA, USA, 2nd edition, 2012.

[80] Batdelger Doljin and Franz Konstantin Fuss. Development of a smart
cricket ball for advanced performance analysis of bowling. *Procedia
Technology*, 20:133 – 137, 2015. Proceedings of The 1st International
Design Technology Conference, DESTECH2015, Geelong.

[81] Li Du. An overview of mobile capacitive touch technologies trends.
CoRR, abs/1612.08227, 2016.

[82] Kenneth P. Fishkin, Bing Jiang, Matthai Philipose, and Sumit Roy. I
sense a disturbance in the force: Unobtrusive detection of interactions

with rfid-tagged objects. In *UbiComp 2004: Ubiquitous Computing: 6th International Conference, Nottingham, UK, September 7-10, 2004. Proceedings*, pages 268–282, 2004.

[83] Franz Konstantin Fuss, Noel Lythgo, Robert Masterton Smith, Amanda Clare Benson, and Brett Gordon. Identification of key performance parameters during off-spin bowling with a smart cricket ball. *Sports Technology*, 4(3-4):159–163, 2011.

[84] Franz Konstantin Fuss and Robert Masterton Smith. Accuracy performance parameters of seam bowling, measured with a smart cricket ball. *Procedia Engineering*, 72:435 – 440, 2014. The Engineering of Sport 10.

[85] Chuhan Gao, Yilong Li, and Xinyu Zhang. Livetag: Sensing human-object interaction through passive chipless wifi tags. In *15th USENIX Symposium on Networked Systems Design and Implementation (NSDI 18)*, pages 533–546, Renton, WA, 2018. USENIX Association.

[86] Y. Ghasempour, C. Yeh, R. Shrestha, D. Mittleman, and E. Knightly. Single shot single antenna path discovery in thz networks. In *Proc. of ACM MobiCom*, 2020.

[87] Wei Gong and Jiangchuan Liu. Sifi: Pushing the limit of time-based wifi localization using a single commodity access point. *Proc. ACM Interact. Mob. Wearable Ubiquitous Technol.*, 2(1):10:1–10:21, 2018.

163

[88] Mahanth Gowda, Ashutosh Dhekne, Sheng Shen, Romit Roy Choudhury, Lei Yang, Suresh Golwalkar, and Alexander Essanian. Bringing iot to sports analytics. In *14th USENIX Symposium on Networked Systems Design and Implementation (NSDI 17)*, pages 499–513, Boston, MA, 2017.

[89] Mahanth Gowda, Ashutosh Dhekne, Sheng Shen, Romit Roy Choudhury, Sharon Xue Yang, Lei Yang, Suresh Golwalkar, and Alexander Essanian. Iot platform for sports analytics. *GetMobile: Mobile Comp. and Comm.*, 21(4):8–14, February 2018.

[90] J. D. Griffin, G. D. Durgin, A. Haldi, and B. Kippelen. Rf tag antenna performance on various materials using radio link budgets. *IEEE Antennas and Wireless Propagation Letters*, 5(1):247–250, Dec 2006.

[91] Y. Guo, L. Yang, B. Li, T. Liu, and Y. Liu. Rollcaller: User-friendly indoor navigation system using human-item spatial relation. In *IEEE INFOCOM 2014 - IEEE Conference on Computer Communications*, pages 2840–2848, April 2014.

[92] V. Gupta, S. Mittal, S. Bhaumik, and R. Roy. Assisting humans to achieve optimal sleep by changing ambient temperature. In *2016 IEEE International Conference on Bioinformatics and Biomedicine (BIBM)*, pages 841–845, Dec 2016.

[93] C H. Loo, Khaled ElMahgoub, Fan Yang, Atef Elsherbeni, Darko Kajfez, Ahmed Kishk, Tamer Elsherbeni, Leena Ukkonen, Lauri

Sydnheimo, Markku Kivikoski, and others . Chip impedance matching for uhf rfid tag antenna design. *Progress In Electromagnetics Research*, 81:359–370, 01 2008.

[94] Unsoo Ha, Yunfei Ma, Zexuan Zhong, Tzu-Ming Hsu, and Fadel Adib. Learning food quality and safety from wireless stickers. In *Proceedings of the 17th ACM Workshop on Hot Topics in Networks*, HotNets '18, pages 106–112, New York, NY, USA, 2018. ACM.

[95] J. Han, H. Ding, C. Qian, W. Xi, Z. Wang, Z. Jiang, L. Shangguan, and J. Zhao. Cbid: A customer behavior identification system using passive tags. *IEEE/ACM Transactions on Networking*, 24(5):2885–2898, Oct 2016.

[96] Alan Hedge, Wafa Sakr, and Anshu Agarwal. Thermal effects on office productivity. *Proceedings of the Human Factors and Ergonomics Society Annual Meeting*, 49(8):823–827, 2005.

[97] C. Hekimian-Williams, B. Grant, Xiuwen Liu, Zhenghao Zhang, and P. Kumar. Accurate localization of rfid tags using phase difference. In *2010 IEEE International Conference on RFID (IEEE RFID 2010)*, pages 89–96, April 2010.

[98] Antonio Jimnez, Fernando Seco, C. Prieto, and Jaime Guevara. A comparison of pedestrian dead-reckoning algorithms using a low-cost mems imu. pages 37 – 42, 09 2009.

[99] N. Jonassen. Human body capacitance: static or dynamic concept? [esd]. In *Electrical Overstress/ Electrostatic Discharge Symposium Proceedings. 1998 (Cat. No.98TH8347)*, pages 111–117, Oct 1998.

[100] Kevin King, N. Perkins, Hugh Churchill, Ryan McGinnis, Ryan Doss, and Ron Hickland. Bowling ball dynamics revealed by miniature wireless mems inertial measurement unit. *Sports Engineering*, 13:95–104, 01 2010.

[101] Manikanta Kotaru, Kiran Joshi, Dinesh Bharadia, and Sachin Katti. Spotfi: Decimeter level localization using wifi. In *Proceedings of the 2015 ACM Conference on Special Interest Group on Data Communication*, SIGCOMM '15, pages 269–282, New York, NY, USA, 2015. ACM.

[102] Manikanta Kotaru, Kiran Joshi, Dinesh Bharadia, and Sachin Katti. Spotfi: Decimeter level localization using WiFi. In *ACM SIGCOMM Computer Communication Review*, volume 45(4), pages 269–282. ACM, 2015.

[103] Manikanta Kotaru and Sachin Katti. Position tracking for virtual reality using commodity wifi. In *Proceedings of the 10th on Wireless of the Students, by the Students, and for the Students Workshop*, S3 '18, pages 15–17, New York, NY, USA, 2018. ACM.

[104] Lito Kriara, Matthew Alsup, Giorgio Corbellini, Matthew Trotter, Joshua D. Griffin, and Stefan Mangold. Rfid shakables: Pairing

radio-frequency identification tags with the help of gesture recognition. In *Proceedings of the Ninth ACM Conference on Emerging Networking Experiments and Technologies*, CoNEXT '13, pages 327–332, New York, NY, USA, 2013. ACM.

[105] Swarun Kumar, Stephanie Gil, Dina Katabi, and Daniela Rus. Accurate indoor localization with zero start-up cost. In *Proceedings of the 20th Annual International Conference on Mobile Computing and Networking*, MobiCom '14, pages 483–494, New York, NY, USA, 2014. ACM.

[106] Swarun Kumar, Stephanie Gil, Dina Katabi, and Daniela Rus. Accurate indoor localization with zero start-up cost. In *Proceedings of the 20th Annual International Conference on Mobile Computing and Networking*, MobiCom '14, pages 483–494, New York, NY, USA, 2014. ACM.

[107] Hanchuan Li, Eric Brockmeyer, Elizabeth J. Carter, Josh Fromm, Scott E. Hudson, Shwetak N. Patel, and Alanson Sample. Paperid: A technique for drawing functional battery-free wireless interfaces on paper. In *Proceedings of the 2016 CHI Conference on Human Factors in Computing Systems*, CHI '16, pages 5885–5896, New York, NY, USA, 2016. ACM.

[108] Hanchuan Li, Can Ye, and Alanson P. Sample. Idsense: A human object interaction detection system based on passive uhf rfid. In

Proceedings of the 33rd Annual ACM Conference on Human Factors in Computing Systems, CHI '15, pages 2555–2564, New York, NY, USA, 2015. ACM.

[109] Jaime Lien, Nicholas Gillian, M. Emre Karagozler, Patrick Amihood, Carsten Schwesig, Erik Olson, Hakim Raja, and Ivan Poupyrev. Soli: Ubiquitous gesture sensing with millimeter wave radar. In *Proc. of ACM SIGGRAPH*, 2016.

[110] Q. Lin, L. Yang, Y. Sun, T. Liu, X. Y. Li, and Y. Liu. Beyond one-dollar mouse: A battery-free device for 3d human-computer interaction via rfid tags. In *2015 IEEE Conference on Computer Communications (INFOCOM)*, pages 1661–1669, April 2015.

[111] T. Liu, L. Yang, Q. Lin, Y. Guo, and Y. Liu. Anchor-free backscatter positioning for rfid tags with high accuracy. In *IEEE INFOCOM 2014 - IEEE Conference on Computer Communications*, pages 379–387, April 2014.

[112] Y. Liu, Y. Zhao, L. Chen, J. Pei, and J. Han. Mining frequent trajectory patterns for activity monitoring using radio frequency tag arrays. *IEEE Transactions on Parallel and Distributed Systems*, 23(11):2138–2149, Nov 2012.

[113] Zhihong Luo, Qiping Zhang, Yunfei Ma, Manish Singh, and Fadel Adib. 3d backscatter localization for fine-grained robotics. In

Proceedings of the 16th USENIX Conference on Networked Systems Design and Implementation, NSDI'19, pages 765–781, Berkeley, CA, USA, 2019. USENIX Association.

[114] N. Ma and L. Chen. The design of folded dipole antenna. In *2008 4th International Conference on Wireless Communications, Networking and Mobile Computing*, pages 1–3, Oct 2008.

[115] Yunfei Ma, Nicholas Selby, and Fadel Adib. Minding the billions: Ultra-wideband localization for deployed rfid tags. In *Proceedings of the 23rd Annual International Conference on Mobile Computing and Networking*, MobiCom '17, pages 248–260. ACM, 2017.

[116] Yunfei Ma, Nicholas Selby, and Fadel Adib. Minding the billions: Ultra-wideband localization for deployed rfids. In *Proc. of ACM MobiCom*, 2017.

[117] S. Manzari, A. Catini, G. Pomarico, C. Di Natale, and G. Marrocco. Development of an uhf rfid chemical sensor array for battery-less ambient sensing. *IEEE Sensors Journal*, 14(10):3616–3623, Oct 2014.

[118] S. Manzari, C. Occhiuzzi, S. Nawale, A. Catini, C. Di Natale, and G. Marrocco. Humidity sensing by polymer-loaded uhf rfid antennas. *IEEE Sensors Journal*, 12(9):2851–2858, Sep. 2012.

[119] S. Manzari, C. Occhiuzzi, S. Nawale, A. Catini, C. Di Natale, and G. Marrocco. Humidity sensing by polymer-loaded uhf rfid antennas.

IEEE Sensors Journal, 12(9):2851–2858, Sept 2012.

[120] Wenguang Mao, Jian He, and Lili Qiu. CAT: high-precision acoustic motion tracking. In *Proc. of ACM MobiCom*, 2016.

[121] Nicolai Marquardt, Alex S. Taylor, Nicolas Villar, and Saul Greenberg. Rethinking rfid: Awareness and control for interaction with rfid systems. In *Proceedings of the SIGCHI Conference on Human Factors in Computing Systems*, CHI '10, pages 2307–2316, New York, NY, USA, 2010. ACM.

[122] G. Marrocco. The art of uhf rfid antenna design: impedance-matching and size-reduction techniques. *IEEE Antennas and Propagation Magazine*, 50(1):66–79, Feb 2008.

[123] G. Marrocco. Pervasive electromagnetics: sensing paradigms by passive rfid technology. *IEEE Wireless Communications*, 17(6):10–17, December 2010.

[124] G. Marrocco. Rfid grids: Part ielectromagnetic theory. *IEEE Transactions on Antennas and Propagation*, 59(3):1019–1026, March 2011.

[125] G. Marrocco and F. Amato. Self-sensing passive rfid: From theory to tag design and experimentation. In *2009 European Microwave Conference (EuMC)*, pages 001–004, Sept 2009.

[126] Ryan S. McGinnis and Noel C. Perkins. A highly miniaturized, wireless inertial measurement unit for characterizing the dynamics of pitched baseballs and softballs. *Sensors*, 12(9):11933–11945, 2012.

[127] R. Miesen, F. Kirsch, and M. Vossiek. Holographic localization of passive uhf rfid transponders. In *2011 IEEE International Conference on RFID*, pages 32–37, April 2011.

[128] S. Milici, S. Amendola, A. Bianco, and G. Marrocco. Epidermal rfid passive sensor for body temperature measurements. In *2014 IEEE RFID Technology and Applications Conference (RFID-TA)*, pages 140–144, Sept 2014.

[129] Rajalakshmi Nandakumar, Vikram Iyer, Desney Tan, and Shyamnath Gollakota. FingerIO: Using active sonar for fine-grained finger tracking. In *Proc. of ACM CHI*, pages 1515–1525, 2016.

[130] Lionel M. Ni, Yunhao Liu, Yiu Cho Lau, and Abhishek P. Patil. Landmarc: Indoor location sensing using active rfid. *Wirel. Netw.*, 10(6):701–710, November 2004.

[131] J. Fergus Nicol and Michael A. Humphreys. Adaptive thermal comfort and sustainable thermal standards for buildings. 2001.

[132] P. V. Nikitin, R. Martinez, S. Ramamurthy, H. Leland, G. Spiess, and K. V. S. Rao. Phase based spatial identification of uhf rfid tags. In

2010 IEEE International Conference on RFID (IEEE RFID 2010), pages 102–109, April 2010.

[133] P. V. Nikitin and K. V. S. Rao. Theory and measurement of backscattering from rfid tags. *IEEE Antennas and Propagation Magazine*, 48(6):212–218, Dec 2006.

[134] Pavel V. Nikitin, K. V. S. Rao, Senior Member, and Steve Lazar. An overview of near field uhf rfid, 2007.

[135] C. Occhiuzzi and G. Marrocco. Constrained-design of passive uhf rfid sensor antennas. *IEEE Transactions on Antennas and Propagation*, 61(6):2972–2980, June 2013.

[136] C. Occhiuzzi and G. Marrocco. Constrained-design of passive uhf rfid sensor antennas. *IEEE Transactions on Antennas and Propagation*, 61(6):2972–2980, June 2013.

[137] C. Occhiuzzi, A. Rida, G. Marrocco, and M. Tentzeris. Rfid passive gas sensor integrating carbon nanotubes. *IEEE Transactions on Microwave Theory and Techniques*, 59(10):2674–2684, Oct 2011.

[138] Cecilia Occhiuzzi and Gaetano Marrocco. Precision and accuracy in uhf-rfid power measurements for passive sensing. *IEEE Sensors Journal*, 16:3091–3098, 2016.

[139] A. Park and J. R. Glass. Towards unsupervised pattern discovery in speech. In *IEEE Workshop on Automatic Speech Recognition and Understanding*, pages 53–58, Nov 2005.

[140] A. S. Park and J. R. Glass. Unsupervised pattern discovery in speech. *IEEE Transactions on Audio, Speech, and Language Processing*, 16(1):186–197, Jan 2008.

[141] Neal Patwari and Sneha K. Kasera. Robust location distinction using temporal link signatures. In *Proceedings of the 13th Annual ACM International Conference on Mobile Computing and Networking*, MobiCom '07, pages 111–122, New York, NY, USA, 2007. ACM.

[142] Chunyi Peng, Guobin Shen, Yongguang Zhang, Yanlin Li, and Kun Tan. BeepBeep: a high accuracy acoustic ranging system using COTS mobile devices. In *Proc. of ACM SenSys*, 2007.

[143] M. Philipose, J. R. Smith, B. Jiang, A. Mamishev, Sumit Roy, and K. Sundara-Rajan. Battery-free wireless identification and sensing. *IEEE Pervasive Computing*, 4(1):37–45, Jan 2005.

[144] G. E. Ponchak, J. L. Jordan, and M. C. Scardelletti. Temperature dependence of thin film spiral inductors on alumina over a temperature range of 25 to 475 c. In *2010 Proceedings 60th Electronic Components and Technology Conference (ECTC)*, pages 713–719, June 2010.

[145] Swadhin Pradhan, Eugene Chai, Karthikeyan Sundaresan, Lili Qiu, Mohammad A. Khojastepour, and Sampath Rangarajan. Rio: A pervasive rfid-based touch gesture interface. In *Proceedings of the 23rd Annual International Conference on Mobile Computing and Networking*, MobiCom '17, pages 261–274, 2017.

[146] Kun Qian, Chenshu Wu, Yi Zhang, Guidong Zhang, Zheng Yang, and Yunhao Liu. Widar2.0: Passive human tracking with a single wi-fi link. In *Proceedings of the 16th Annual International Conference on Mobile Systems, Applications, and Services*, MobiSys '18, pages 350–361, New York, NY, USA, 2018. ACM.

[147] Lanxin Qiu, Zhangqin Huang, Shaohua Zhang, Cheng Jing, Hao Li, and Shuyao Li. Multifrequency phase difference of arrival range measurement: Principle, implementation, and evaluation. *International Journal of Distributed Sensor Networks*, 2015.

[148] H. Rahul, F. Edalat, D. Katabi, and C. Sodini. Frequency-aware rate adaptation and mac protocols. In *Proc. of MobiCom*, 2009.

[149] Anshul Rai, Krishna Kant Chintalapudi, Venkata N. Padmanabhan, and Rijurekha Sen. Zee: Zero-effort crowdsourcing for indoor localization. In *Proceedings of the 18th Annual International Conference on Mobile Computing and Networking*, Mobicom '12, pages 293–304, New York, NY, USA, 2012. ACM.

[150] K. V. S. Rao, P. V. Nikitin, and S. F. Lam. Antenna design for uhf rfid tags: a review and a practical application. *IEEE Transactions on Antennas and Propagation*, 53(12):3870–3876, Dec 2005.

[151] K. V. S. Rao, P. V. Nikitin, and S. F. Lam. Antenna design for uhf rfid tags: a review and a practical application. *IEEE Transactions on Antennas and Propagation*, 53(12):3870–3876, Dec 2005.

[152] K. V. S. Rao, Pavel V. Nikitin, and Sander F. Lam. Impedance matching concepts in rfid transponder design. In *Proceedings of the Fourth IEEE Workshop on Automatic Identification Advanced Technologies*, AUTOID '05, pages 39–42, Washington, DC, USA, 2005. IEEE Computer Society.

[153] K. V. Seshagiri Rao, Senior Member, Pavel V. Nikitin, and Er F. Lam. Antenna design for uhf rfid tags: A review and a practical application. *IEEE Trans. Antennas Propag*, pages 3870–3876, 2005.

[154] K. V. Seshagiri Rao, Pavel V. Nikitin, and Sander F. Lam. Antenna design for uhf rfid tags: A review and a practical application. *IEEE TRANSACTIONS ON ANTENNAS AND PROPAGATION*, 2005.

[155] R. A. A. Rodrigues, E. C. Gurjo, and F. M. de Assis. Radar cross-section and electric field analysis of backscattering elements of chipless rfid tag. In *2014 IEEE RFID Technology and Applications Conference (RFID-TA)*, pages 103–108, Sept 2014.

[156] Wenjie Ruan, Lina Yao, Quan Z. Sheng, Nickolas J. G. Falkner, and Xue Li. Tagtrack: Device-free localization and tracking using passive rfid tags. In *Proceedings of the 11th International Conference on Mobile and Ubiquitous Systems: Computing, Networking and Services*, MOBIQUITOUS '14, pages 80–89, ICST, Brussels, Belgium, Belgium, 2014. ICST (Institute for Computer Sciences, Social-Informatics and Telecommunications Engineering).

[157] A. P. Sample, D. J. Yeager, P. S. Powledge, and J. R. Smith. Design of a passively-powered, programmable sensing platform for uhf rfid systems. In *2007 IEEE International Conference on RFID*, pages 149–156, March 2007.

[158] A. P. Sample, D. J. Yeager, P. S. Powledge, and J. R. Smith. Design of a passively-powered, programmable sensing platform for uhf rfid systems. In *2007 IEEE International Conference on RFID*, pages 149–156, March 2007.

[159] A. P. Sample, D. J. Yeager, and J. R. Smith. A capacitive touch interface for passive rfid tags. In *2009 IEEE International Conference on RFID*, pages 103–109, April 2009.

[160] S. Sarkka, V. V. Viikari, M. Huusko, and K. Jaakkola. Phase-based uhf rfid tracking with nonlinear kalman filtering and smoothing. *IEEE Sensors Journal*, 12(5):904–910, May 2012.

[161] Souvik Sen, Jeongkeun Lee, Kyu-Han Kim, and Paul Congdon. Avoiding multipath to revive inbuilding wifi localization. In *Proceeding of the 11th Annual International Conference on Mobile Systems, Applications, and Services*, MobiSys '13, pages 249–262, New York, NY, USA, 2013. ACM.

[162] Souvik Sen, Jeongkeun Lee, Kyu-Han Kim, and Paul Congdon. Avoiding multipath to revive inbuilding WiFi localization. In *Proceeding of the 11th annual international conference on Mobile systems, applications, and services*, pages 249–262. ACM, 2013.

[163] Souvik Sen, Božidar Radunovic, Romit Roy Choudhury, and Tom Minka. You are facing the mona lisa: Spot localization using phy layer information. In *Proceedings of the 10th International Conference on Mobile Systems, Applications, and Services*, MobiSys '12, pages 183–196, New York, NY, USA, 2012. ACM.

[164] Longfei Shangguan and Kyle Jamieson. The design and implementation of a mobile rfid tag sorting robot. In *Proceedings of the 14th Annual International Conference on Mobile Systems, Applications, and Services*, MobiSys '16, pages 31–42, New York, NY, USA, 2016. ACM.

[165] Longfei Shangguan and Kyle Jamieson. Leveraging electromagnetic polarization in a two-antenna motion tracking system. *ACM CoNext*, 2016.

[166] Longfei Shangguan, Zhenjiang Li, Zheng Yang, Mo Li, and Yunhao Liu. Otrack: Order tracking for luggage in mobile rfid systems. In *INFOCOM*, pages 3066–3074. IEEE, 2013.

[167] Longfei Shangguan, Zheng Yang, Alex X. Liu, Zimu Zhou, and Yunhao Liu. Relative localization of rfid tags using spatial-temporal phase profiling. In *12th USENIX Symposium on Networked Systems Design and Implementation (NSDI 15)*, pages 251–263, Oakland, CA, May 2015. USENIX Association.

[168] Longfei Shangguan, Zimu Zhou, Xiaolong Zheng, Lei Yang, Yunhao Liu, and Jinsong Han. Shopminer: Mining customer shopping behavior in physical clothing stores with cots rfid devices. In *Proceedings of the 13th ACM Conference on Embedded Networked Sensor Systems*, SenSys '15, pages 113–125, New York, NY, USA, 2015. ACM.

[169] Sheng Shen, Mahanth Gowda, and Romit Roy Choudhury. Closing the gaps in inertial motion tracking. In *Proceedings of the 24th Annual International Conference on Mobile Computing and Networking*, MobiCom '18, pages 429–444, 2018.

[170] Xianwei Shi, Fan Yang, Shenheng Xu, and Maokun Li. A passive temperature-sensing antenna based on a bimetal strip coil. *Sensors*, 17(4):665, 2017.

[171] Katrin Steinberg, Marc Scheffler, and Martin Dressel. Microwave inductance of thin metal strips, 2010.

[172] W.L. Stutzman and G.A. Thiele. *Antenna Theory and Design.*
Antenna Theory and Design. Wiley, 2012.

[173] Li Sun, Souvik Sen, Dimitrios Koutsonikolas, and Kyu-Han Kim.
Widraw: Enabling hands-free drawing in the air on commodity wifi
devices. In *Proceedings of the 21st Annual International Conference on
Mobile Computing and Networking*, MobiCom '15, pages 77–89, New
York, NY, USA, 2015. ACM.

[174] Y. Tanaka, Y. Umeda, O. Takyu, M. Nakayama, and K. Kodama.
Change of read range for uhf passive rfid tags in close proximity. In
2009 IEEE International Conference on RFID, pages 338–345, April
2009.

[175] Deepak Vasisht, Swarun Kumar, and Dina Katabi. Decimeter-level
localization with a single wifi access point. In *13th USENIX
Symposium on Networked Systems Design and Implementation (NSDI
16)*, pages 165–178, Santa Clara, CA, 2016.

[176] He Wang, Souvik Sen, Ahmed Elgohary, Moustafa Farid, Moustafa
Youssef, and Romit Roy Choudhury. No need to war-drive:
Unsupervised indoor localization. In *Proceedings of the 10th
International Conference on Mobile Systems, Applications, and
Services*, MobiSys '12, pages 197–210, New York, NY, USA, 2012.
ACM.

[177] Jingxian Wang, Junbo Zhang, Rajarshi Saha, Haojian Jin, and Swarun Kumar. Pushing the range limits of commercial passive rfids. In *16th USENIX Symposium on Networked Systems Design and Implementation (NSDI 19)*, pages 301–316, Boston, MA, February 2019. USENIX Association.

[178] Ju Wang, Omid Abari, and Srinivasan Keshav. Challenge: Rfid hacking for fun and profit. In *Proceedings of the 24th Annual International Conference on Mobile Computing and Networking*, MobiCom '18, pages 461–470, New York, NY, USA, 2018. ACM.

[179] Ju Wang, Jie Xiong, Xiaojiang Chen, Hongbo Jiang, Rajesh Krishna Balan, and Dingyi Fang. Tagscan: Simultaneous target imaging and material identification with commodity rfid devices. In *Proc. of ACM MobiCom*, pages 288–300. ACM, 2017.

[180] Jue Wang, Fadel Adib, Ross Knepper, Dina Katabi, and Daniela Rus. Rf-compass: Robot object manipulation using rfids. In *Proceedings of the 19th Annual International Conference on Mobile Computing & Networking*, MobiCom '13, pages 3–14, New York, NY, USA, 2013. ACM.

[181] Jue Wang, Fadel Adib, Ross Knepper, Dina Katabi, and Daniela Rus. RF-compass: robot object manipulation using RFIDs. In *Proc. of the 19th annual international conference on Mobile computing and networking*, pages 3–14, 2013.

[182] Jue Wang and Dina Katabi. Dude, where's my card?: Rfid positioning that works with multipath and non-line of sight. In *Proceedings of the ACM SIGCOMM 2013 Conference on SIGCOMM*, SIGCOMM '13, pages 51–62, New York, NY, USA, 2013. ACM.

[183] Jue Wang and Dina Katabi. Dude, where's my card? RFID positioning that works with multipath and non-line of sight. In *Proc. of the ACM SIGCOMM*, pages 51–62, 2013.

[184] Jue Wang, Deepak Vasisht, and Dina Katabi. Rf-idraw: Virtual touch screen in the air using rf signals. In *Proceedings of the 2014 ACM Conference on SIGCOMM*, SIGCOMM '14, pages 235–246, New York, NY, USA, 2014. ACM.

[185] Jue Wang, Deepak Vasisht, and Dina Katabi. RF-IDraw: virtual touch screen in the air using RF signals. In *Proc. of ACM SIGCOMM*, 2014.

[186] Wei Wang, Alex X Liu, and Ke Sun. Device-free gesture tracking using acoustic signals. In *Proceedings of the 22nd Annual International Conference on Mobile Computing and Networking*, pages 82–94. ACM, 2016.

[187] Teng Wei and Xinyu Zhang. mTrack: high precision passive tracking using millimeter wave radios. In *Proc. of ACM MobiCom*, 2015.

[188] Teng Wei and Xinyu Zhang. Gyro in the air: Tracking 3d orientation of batteryless internet-of-things. In *Proceedings of the 22Nd Annual*

International Conference on Mobile Computing and Networking, MobiCom '16, pages 55–68, New York, NY, USA, 2016. ACM.

[189] E. Weisstein. Chinese remainder theorem. https://bit.ly/2xlV42S.

[190] Z. Wu, Y. Han, Y. Chen, and K. J. R. Liu. A time-reversal paradigm for indoor positioning system. *IEEE Transactions on Vehicular Technology*, 64(4):1331–1339, April 2015.

[191] Yaxiong Xie, Zhenjiang Li, and Mo Li. Precise power delay profiling with commodity wifi. In *Proceedings of the 21st Annual International Conference on Mobile Computing and Networking*, MobiCom '15, pages 53–64, New York, NY, USA, 2015. ACM.

[192] Yaxiong Xie, Jie Xiong, Mo Li, and Kyle Jamieson. md-track: Leveraging multi-dimensionality for passive indoor wi-fi tracking. In *The 25th Annual International Conference on Mobile Computing and Networking*, MobiCom '19, pages 8:1–8:16, New York, NY, USA, 2019. ACM.

[193] Yaxiong Xie, Yanbo Zhang, Jansen Christian Liando, and Mo Li. Swan: Stitched wi-fi antennas. In *Proceedings of the 24th Annual International Conference on Mobile Computing and Networking*, MobiCom '18, pages 51–66, New York, NY, USA, 2018. ACM.

[194] Jie Xiong and Kyle Jamieson. Arraytrack: A fine-grained indoor location system. In *Proceedings of the 10th USENIX Conference on*

Networked Systems Design and Implementation, nsdi'13, pages 71–84, Berkeley, CA, USA, 2013. USENIX Association.

[195] Jie Xiong and Kyle Jamieson. Arraytrack: A fine-grained indoor location system. In *Proc. of NSDI*, pages 71–84, 2013.

[196] F. Yang, Q. Qiao, J. Virtanen, A. Z. Elsherbeni, L. Ukkonen, and L. Sydanheimo. Reconfigurable sensing antenna: A slotted patch design with temperature sensation. *IEEE Antennas and Wireless Propagation Letters*, 11:632–635, 2012.

[197] L. Yang, Y. Qi, J. Fang, X. Ding, T. Liu, and M. Li. Frogeye: Perception of the slightest tag motion. In *IEEE INFOCOM 2014 - IEEE Conference on Computer Communications*, pages 2670–2678, April 2014.

[198] Lei Yang, Yekui Chen, Xiang-Yang Li, Chaowei Xiao, Mo Li, and Yunhao Liu. Tagoram: Real-time tracking of mobile rfid tags to high precision using cots devices. In *Proceedings of the 20th Annual International Conference on Mobile Computing and Networking*, MobiCom '14, pages 237–248, New York, NY, USA, 2014. ACM.

[199] Lei Yang, Yekui Chen, Xiang-Yang Li, Chaowei Xiao, Mo Li, and Yunhao Liu. Tagoram: Real-time tracking of mobile RFID tags to high precision using cots devices. In *Proc. of ACM MobiCom*, 2014.

183

[200] Zheng Yang, Chenshu Wu, Zimu Zhou, Xinglin Zhang, Xu Wang, and Yunhao Liu. Mobility increases localizability: A survey on wireless indoor localization using inertial sensors. *ACM Comput. Surv.*, 47(3):54:1–54:34, 2015.

[201] Lina Yao, Wenjie Ruan, Quan Z. Sheng, Xue Li, and Nicholas J.G. Falkner. Exploring tag-free rfid-based passive localization and tracking via learning-based probabilistic approaches. In *Proceedings of the 23rd ACM International Conference on Conference on Information and Knowledge Management*, CIKM '14, pages 1799–1802, New York, NY, USA, 2014. ACM.

[202] Daniel Yeager, Alanson Sample, and Joshua Smith. *Wisp: A passively powered uhf rfid tag with sensing and computation.* 01 2008.

[203] Sangki Yun, Yi-Chao Chen, and Lili Qiu. Turning a mobile device into a mouse in the air. In *Proceedings of the 13th Annual International Conference on Mobile Systems, Applications, and Services*, MobiSys '15, pages 15–29, New York, NY, USA, 2015. ACM.

[204] Sangki Yun, Yi-Chao Chen, Huihuang Zheng, Lili Qiu, and Wenguang Mao. Strata: Fine-grained acoustic-based device-free tracking. In *Proceedings of the 15th Annual International Conference on Mobile Systems, Applications, and Services*, pages 15–28. ACM, 2017.

[205] Pengyu Zhang, Pan Hu, Vijay Pasikanti, and Deepak Ganesan. Ekhonet: High speed ultra low-power backscatter for next generation

sensors. In *Proceedings of the 20th Annual International Conference on Mobile Computing and Networking*, MobiCom '14, pages 557–568, New York, NY, USA, 2014. ACM.

[206] Yaodong Zhang and James R. Glass. Unsupervised spoken keyword spotting via segmental dtw on gaussian posteriorgrams. In *ASRU*, pages 398–403. IEEE, 2009.

[207] Zengbin Zhang, David Chu, Xiaomeng Chen, and Thomas Moscibroda. Swordfight: Enabling a new class of phone-to-phone action games on commodity phones. In *Proc. of ACM MobiSys*, 2012.

[208] Pengfei Zhou, Mo Li, and Guobin Shen. Use it free: Instantly knowing your phone attitude. In *Proceedings of the 20th Annual International Conference on Mobile Computing and Networking*, MobiCom '14, pages 605–616, 2014.

[209] Y. Zou, J. Xiao, J. Han, K. Wu, Y. Li, and L. M. Ni. Grfid: A device-free gesture recognition system using cots rfid device. *IEEE Transactions on Mobile Computing*, PP(99):1–1, 2016.